DISSERTATION

QUANTUM MAGNETISM IN THE RARE-EARTH PYROSILICATES

Submitted by

Gavin L. Hester

Department of Physics

In partial fulfillment of the requirements

For the Degree of Doctor of Philosophy

Colorado State University

Fort Collins, Colorado

Spring 2021

Doctoral Committee:

Advisor: Kate Ross

Hua Chen
Martin Gelfand
Matthew Shores

ABSTRACT

QUANTUM MAGNETISM IN THE RARE-EARTH PYROSILICATES

In recent years, both physicists and non-physicists have shown immense interest in the burgeoning field of quantum computing and the possible applications a quantum computer could be used for [1]. However, current quantum computers suffer from issues of decoherence: where the quantum state used for computation is broken by external noise. A new possible avenue for quantum computation would be to use systems that are intrinsically protected from some level of noise, such as topologically protected states. Topological states are inherently protected from small perturbations due to their topological nature. However, to exploit this feature of topologically protected systems more experimental realizations are needed to better understand the underlying mechanisms. This has motivated a surge in interest of condensed matter systems with topologically protected states, such as the quantum spin liquid or fractional quantum Hall systems. A current focus in the subfield of quantum magnetism has focused on using the anisotropic exchange properties of the rare-earth (La - Lu) ions to find quantum spin liquid states, such as the Kitaev spin liquid that is predicted for systems exhibiting a honeycomb lattice. The Kitaev model is an exactly solvable model with a quantum spin liquid ground state, allowing for precise comparison between experiment and theory. Currently, no system has been rigorously proven to be a Kitaev spin liquid but developing our understanding of the underlying physical mechanisms in these systems may allow for the "engineering" of systems that are likely to be Kitaev spin liquids.

The desire to understand the underlying mechanisms for quantum spin liquids and other quantum ground states led to the study of the three-honeycomb rare-earth pyrosilicate compounds discussed in this dissertation. The first compound, $Yb_2Si_2O_7$, is a quantum dimer magnet system with the first evidence for a rare-earth based triplon Bose-Einstein condensate. Inelastic neutron scattering, specific heat, and ultrasound velocity measurements showed a characteristic (for triplon

Bose-Einstein condensates) dome in the field-temperature phase diagram and provided evidence for predominantly isotropic exchange, something that is not typically expected for rare-earth systems. Following this work on $Yb_2Si_2O_7$, our focused turned to two of the Er^{3+} rare-earth pyrosilicates. The first of these Er^{3+}-based pyrosilicates measured was D-$Er_2Si_2O_7$. Previous work on D-$Er_2Si_2O_7$ discovered a highly anisotropic g-tensor, an antiferromagnetic ground state, and modeled a selection of the magnetic field induced transitions via Monte-Carlo simulations [2]. Our work followed up on this with AC susceptibility, powder inelastic neutron scattering, and powder neutron diffraction measurements to further investigate the ground state of this quantum magnet. Through this we discovered that the system enters an antiferromagnetic state with the spins almost aligned along the previously determined local Ising-axis [2]. The inelastic neutron scattering spectrum show a gapped excitation at zero field - consistent with Ising-like exchange. Transverse field AC susceptibility shows a change in the susceptibility at 2.65 T. These signatures indicate that D-$Er_2Si_2O_7$ exhibits predominantly Ising-like exchange and that a transition can be induced by a field applied transverse to the Ising axis. This allows for the possibility of D-$Er_2Si_2O_7$ bein g a new experimental realization of the Transverse Field Ising Model (TFIM). The TFIM is a simple, anisotropic exchange, theoretically tractable model exhibiting quantum criticality with few experimental examples, making new experimental examples of this model highly desired. These intriguing results on D-$Er_2Si_2O_7$ and $Yb_2Si_2O_7$ led to an interest in the polymorph formed at lower synthesis temperatures, C-$Er_2Si_2O_7$, which happens to be isostructural to $Yb_2Si_2O_7$. Measurements of the neutron diffraction, specific heat, and magnetization/susceptibility in this system allowed for us to determine that C-$Er_2Si_2O_7$ magnetically orders at 2.3 K into an antiferromagnetic Néel state. While this is the expected ground state for an isotropically exchange coupled honeycomb system, C-$Er_2Si_2O_7$ does not form a "perfect" honeycomb lattice and it is interesting that C-$Er_2Si_2O_7$ magnetically orders while $Yb_2Si_2O_7$ does not. Understanding the ground state for C-$Er_2Si_2O_7$ will allow for bettering our understanding of $Yb_2Si_2O_7$ and rare-earth quantum magnet ground states by comparing the properties of the two systems. Overall, the work on these three compounds required numerous experimental techniques, models, and theoretical understanding.

It is my hope that the preliminary understanding for these three pyrosilicates will motivate future work within the rare-earth pyrosilicate family and provide a family of rare-earth quantum magnets that can be studied to improve our understanding of novel quantum states.

ACKNOWLEDGEMENTS

First and foremost, I would like to thank my wife Nycole for her support throughout my graduate school career. From reading parts of this dissertation to listening to my practice talks, your support has pushed me through the hardest times of the past five years. I would also like to thank my sister Caylin, my brother-in-law Bryant, my nephew Lyle, my niece Elayna, my father Gary, my mother Ellen, and my grandmother Mary. Caylin and Bryant, it is difficult to put into words how much appreciation I have for everything you all have done for me. Without your support I never would have had the opportunity to perform extracurricular research during my undergraduate years, enabling my entrance to graduate school. Your selflessness in allowing me to live with you throughout my undergraduate years - paying a dismally small amount of rent - is greatly appreciated. To my father Gary, you have always been one of my strongest supporters, you are always the first to give a "I'm proud of you, son." when it is needed, something that has helped me surpass many of the hurdles of graduate school. To my mother Ellen, you were the person who helped nurture my young mind, pushed me academically, and set the foundation for me to pursue my dreams. To my grandmother Mary, your support over the years has been incredible and I appreciate all the skills and traits you have instilled in me. I would also like to thank other influential members of my extended family who helped nurture my scientific and mechanical skills throughout the years: my aunt and uncle John and Nancy Erkenbrack, my aunt and uncle Ann and Rich Gebhard, and my cousins Dan and Tracy Gebhard.

I would like to thank all the people who supported me throughout my undergraduate and graduate school years. In my undergraduate years, I was lucky enough to work with four fantastic mentors: Ikenna Nlebedim, Saibal Mitra, David Cornelison, and Tom Heitmann. All these mentors have made me the scientists I am today. I would like to particularly single out Tom Heitmann. Tom, you introduced me to one of my true loves, neutron scattering, and you have served as a valuable mentor throughout graduate school - thank you. In my research, I have had the opportunity to work with some wonderful people, including, but not limited to: Tim DeLazzer, Danielle

Yahne, Colin Sarkis, John Ringler, Andrew Treglia, Steffen Säubert, Siau Sing Lim, Hari Nair, Jamie Neilson, Daniel Shaw, Theo Wecker, Tim Reeder, and Antony Sikorski. I would also like to thank all the support staff both at Colorado State University and at the neutron sources utilized. All of you have enabled the scientific work included in this document and I cherish my time working with you all. I would also like to thank some of the closest friends I have made in graduate school. I would like to specifically acknowledge Danielle Yahne. Danielle, you are one my best friends and my closest scientific colleagues. Your friendship has helped me become a better person and your insight and advice has made me a better scientist. I look forward to our years to come of scientific collaboration and friendship. I would also like to single out Colin Sarkis, I appreciate every debate we have had over the years, particularly those about science and video games. You have been a valuable scientific partner on numerous works included here and I hope we are able to continue to work together in the future. I would also like to acknowledge Aidan Winblad and Alec Iverson. Our gaming nights have provided innumerable laughs over the years and our frank discussions about mental health have encouraged me to address my mental health and push for normalization of discussing mental health problems in science. I would also like to thank a longtime friend from high school, Zach "Halfy" Henley. Zach, our friendship over the years has provided me so much happiness and so many laughs. I appreciate you being there as a friend over the years, keeping me grounded, and always being happy to decompress with video games together.

I would also like to thank many of the people that helped guide this work, including my committee members: Matt Shores, Marty Gelfand, and Hua Chen. You all have been incredibly supportive, providing valuable insights and asking questions that have given me a new perspective upon this research. I would also like to specifically thank my advisor, Kate Ross. Kate, it is difficult to adequately capture the profound impact you have had upon my career as a scientist and me as a person. As a research advisor, you have been incredibly supportive of everything I wanted to do in graduate school, from traveling to numerous conferences to trying new experimental techniques, and I consider it a privilege to have worked with such a brilliant scientist. As a mentor,

your honesty, humility, and compassion have provided me a template for the advisor I hope to one day be and I look forward to your mentorship for the years to come. Thank you.

Finally, I would also like to acknowledge those people and entities who assisted with the research and the writing of the papers shown in Chapter 3-5, that may not have already been mentioned. All of this research was supported by the National Science Foundation Agreement No. DMR-1611217 and DMR-2005143. I would also like to acknowledge the Central Instrument Facility at Colorado State University for instrument access and training. For the work on $Yb_2Si_2O_7$, my coauthor Jeff Quilliam acknowledges technical support from M. Castonguay and S. Fortier, informative conversations with G. Quirion, C. Bourbonnais and I. Garate and funding from NSERC. I would also like to acknowledge the assistance of Aaron Glock and Antony Sikorski in the sample synthesis, as well as Craig Brown for his assistance with the BT1 neutron powder diffraction experiment on $Yb_2Si_2O_7$. For the inelastic scattering measurements on D-$Er_2Si_2O_7$, access to MACS was provided by the Center for High Resolution Neutron Scattering, a partnership between the National Institute of Standards and Technology and the National Science Foundation under Agreement No. DMR-1508249. Many of the measurements included here used resources at the High Flux Isotope Reactor and the Spallation Neutron Source, a DOE Office of Science User Facility operated by Oak Ridge National Laboratory. I would also like to thank Gang Cao for enabling our use of millikelvin range AC susceptometry on D-$Er_2Si_2O_7$. I would also like to thank John McArthur for performing the DC magnetometry measurements presented on D-$Er_2Si_2O_7$.

DEDICATION

For my wife and family. Your unwavering love and support has encouraged me to pursue my dreams.

I have no special talent. I am only passionately curious.

$\sim$ *Albert Einstein*

TABLE OF CONTENTS

Chapter 1

Introduction

The twentieth century brought us the revolutionary understanding of quantum mechanics and relativity, and it seems that the twenty-first century will be defined by our ability to harness these basic physical mechanisms for the betterment of humanity. One of the most promising developments in this direction is the search for new methods for quantum computation. Quantum computing is particularly powerful due to the property of superposition. In a classical computer, data is stored in binary ones and zeroes, called "bits", but in a quantum computer the bit can be in both the one and the zero state at the same time. When a collection of these qubits (quantum bits) is entangled, they can be utilized for factoring large numbers [3], modeling quantum systems [4], and numerous other powerful applications. Current quantum computation generally utilizes ultracold gasses or entanglement of superconducting loops, however decoherence [1] is common in these systems, thus making practical use more difficult [5, 6]. A possible platform for future developments of quantum computing is performing computations using topologically protected states such as topological insulators or quantum spin liquids. The topological nature of these systems provides robustness against decoherence, as topological systems are not affected by local perturbations. These platforms share the commonality that they are based on condensed matter systems. Therefore, to properly harness these platforms, we must understand the underlying mechanisms controlling the quantum states. Particularly in the realm of quantum spin liquids, this understanding is in the process of being developed, but the prospect of "engineering" a quantum spin liquid is on the horizon. To move towards this reality of "engineering" quantum spin liquids - and quantum states in general - new systems must be synthesized, characterized, and understood. In this dissertation I have focused on elucidating the quantum ground states of three members of the rare-earth pyrosilicate family of compounds: $Yb_2Si_2O_7$, D-$Er_2Si_2O_7$, and C-$Er_2Si_2O_7$. While none of these

[1] Decoherence is the loss of information from a system to its environment. Particularly for quantum computers decoherence is an issue as the carefully prepared quantum state for a computation could be destroyed by interacting with the environment.

systems exhibit a quantum spin liquid ground state, they serve as a stepping stone towards understanding the ground states of quantum magnets which in the future may be leveraged to engineer quantum states.

This dissertation consists of five chapters in addition to this introductory chapter. Chapter 2 focuses on explaining the necessary background knowledge needed to understand the results presented in Chapter 3-5. I begin Chapter 2 by outlining the basics of magnetic solids and the process of superexchange. I then specifically focus on the Hamiltonians relevant to this work: the quantum dimer magnet and the transverse field Ising model Hamiltonian. All the work performed for this dissertation included rare-earth ions in oxygen crystal fields, so a brief discussion of the underlying physics for crystal electric fields is also given in Chapter 2. Chapter 2 also contains an overview of the experimental techniques used, including neutron scattering, heat capacity, and magnetometry. I thoroughly discuss neutron scattering theory and experiment, as this technique provided the base for the three sets of results presented and I am truly passionate about neutron scattering.

Following the background of Chapter 2, Chapters 3-5 consists of academic papers written for research journals. Each chapter focuses on a different rare-earth pyrosilicate compound, with Chapter 3 consisting of my paper on $Yb_2Si_2O_7$, published under reference [7]. This paper outlines our discovery of a quantum dimer magnet ground state with evidence for a field-induced Bose-Einstein condensate (BEC); the first of its kind based on a pseudo spin-$\frac{1}{2}$ ion. This paper also furthers an emerging narrative that - contrary to conventional wisdom - rare-earth based ions often exhibit isotropic - or nearly isotropic - exchange interactions [8, 9]. This work also motivated the study of the two compounds in Chapter 4 and Chapter 5. Chapter 4 consists of my in-progress paper on D-$Er_2Si_2O_7$. This preliminary paper outlines our experimental work on the Ising-like compound D-$Er_2Si_2O_7$ where a transition can be induced via a transverse applied magnetic field, indicating that D-$Er_2Si_2O_7$ exhibit properties of the transverse field Ising model (TFIM), a model that currently only has a few experimental realizations. Chapter 5 includes my paper on C-$Er_2Si_2O_7$, published under reference [10]. The compound, C-$Er_2Si_2O_7$, is isostruc-

tural to the quantum dimer magnet compound $Yb_2Si_2O_7$, but C-$Er_2Si_2O_7$ magnetically orders at 2.3 K while $Yb_2Si_2O_7$ does not magnetically order. This difference between these isostructural compounds provides the opportunity to study how the ground states of quantum magnets change when the rare-earth ion is substituted. Finally, in Chapter 6 I will summarize the major results and motivate future work for these three rare-earth pyrosilicate systems.

Chapter 2

Background

2.1 Magnetism

From early human discovering strange rocks that attract other rocks - called lodestones - to children baffled by the repulsion of two rare-earth magnets, humans have always been entranced by the mysterious forces of magnetism. In this work we will be focusing on magnetic materials, which come in a few different varieties; the ferromagnet, the antiferromagnet, the paramagnet, and the diamagnet. Ferromagnetic systems are the canonical magnets most people are familiar with, they have a spontaneous magnetization in zero magnetic field, and have all their magnetic spins aligned along the same direction. Antiferromagnets are magnets with no spontaneous magnetization due to their neighboring spins ordering in opposite directions, thus cancelling each other out. In analogy to the "traditional" states of matter (e.g. liquids, gasses, solids) the antiferromagnet and ferromagnet states can be thought of as magnetic solids. The paramagnet can then be thought of as a magnetic gas, where all the spins point randomly in space, yielding no net magnetic moment and no correlation between spins [2]. The paramagnet state generally exists for all magnetic materials at high enough temperatures. Finally, there is the diamagnet, which exhibits a spontaneous magnetization antiparallel to an applied field causing them to repel magnetic fields. All materials have some level of diamagnetism present, but it is generally significantly weaker than the other forms of magnetism.

One thing that is left out of this description is the underlying mechanisms describing how this magnetism operates at a fundamental level. If we consider a ferromagnetic or antiferromagnetic system at very high temperatures, the system likely acts paramagnetic with no preferred spin direction. As the system is cooled down from high temperatures, the system searches for the state that

[2]The liquid in this analogy would be the quantum spin liquid state. This is a state where the spins are correlated and dynamic, however, there is no magnetic ordering.

will most minimize its free energy. This could be with the spins parallel to one another, antiparallel, some combination of parallel or antiparallel, or in the case of strong magnetic frustration, no magnetic ordering may happen. The main governing mechanisms for the magnetic ordering are the exchange interaction and the dipole interaction. A magnetic system will (generally) magnetically order when the thermal energy (k_BT) becomes equal in magnitude to the interaction energy (J) between the magnetic atoms. In the case of the dipole interaction, one can think of this interaction energy as being the "classical" magnetic coupling between two magnetic dipoles, which can result in the dipoles align antiferromagnetically or ferromagnetically, depending upon their relative location (see Fig. 2.1). Importantly, the dipole interaction is proportional to the size of the magnetic moment, so when considering systems with small magnetic moments, where the dipolar interaction potential is much smaller then the other types of exchange in the system, one can often ignore the dipole interaction. Another common magnetic interaction in the systems studied for this work is that of exchange interactions, which are purely quantum mechanical in nature. The exchange interaction arises due to the electrostatic Coulomb interactions between the electrons and the Pauli exclusion principle. Physically, the exchange interaction represents the energy cost for an electron to switch locations with its neighbor. There is a finite energy cost to this process due to the electrons repelling one another electrostatically (Coulomb interaction) and due to the electrons inability to occupy the same state (Pauli exclusion principle).

There are many flavors of exchange interactions that share this underlying mechanism, with a few being: direct exchange, Dzyaloshinskii–Moriya interaction, and superexchange. The predominant exchange interaction type for materials studied in this work is superexchange. This is - in part - due to the highly localized nature of the unpaired electrons in the systems studied and their insulating nature. The process of superexchange starts by two magnetic atoms sharing a non-magnetic neighbor (e.g. O^{2-}) between them. This non-magnetic neighbor's orbitals overlap with the orbitals of both magnetic atoms, creating a mainfold of electronic states where the sign of the exchange is determined by the lowest energy electronic state. Depending on the nature of the lowest energy electronic state (which is influenced by the bond angles, bond symmetry, and the magnetic species,

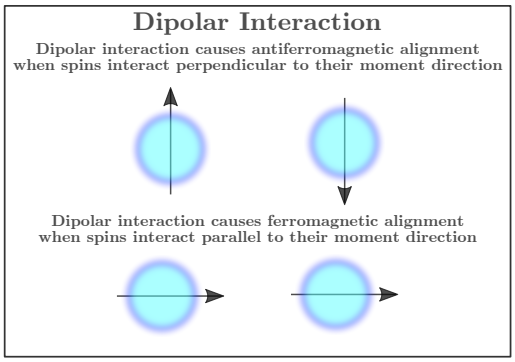
Dipolar Interaction
Dipolar interaction causes antiferromagnetic alignment when spins interact perpendicular to their moment direction
Dipolar interaction causes ferromagnetic alignment when spins interact parallel to their moment direction

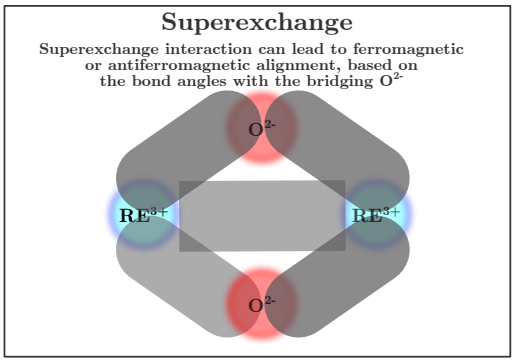
Superexchange
Superexchange interaction can lead to ferromagnetic or antiferromagnetic alignment, based on the bond angles with the bridging O^{2-}
O^{2-}
RE^{3+}
RE^{3+}
O^{2-}

phases due to the large total angular momentum, as (generally) the higher the number of accessible states, the more classical a system is. This can be understood by thinking about the classical limit of any system. In quantum mechanics, the states exist at discrete energy levels. As the limit to classical physics is taken, the discrete energy levels turn into a continuum, which is essentially a system with an infinite number of accessible states. If we now consider placing a Yb^{3+} ion in an ionic solid, the Yb^{3+} ion can be in a cage of highly electronegative atoms, such as O^{2-}. This cage of O^{2-} ions influence the energy landscape of the total angular momentum states through the Stark effect, breaking the degeneracy of the eight J_z angular momentum eigenstates. This alludes to a benefit of the rare-earth ions; the incredibly high spin-orbit coupling and the highly localized nature of the $4f$ electrons allow for the crystal electric field (CEF) to be treated as a perturbation, due to the spin-orbit coupling in these systems being much stronger then the CEF. The pertubative nature of the CEF allows for all of Hund's rules to apply, simplifying analysis of the ground state magnetism of the rare-earth ion. In the case of Yb^{3+}, there are an odd number of electrons in the outer shell meaning that the system is subject to Kramer's degeneracy theorem. Kramer's degeneracy theorem states that any time-reversal symmetric system made of an odd number of fermionic particles must have at least doubly degenerate energy eigenstates. This means that in the case of a magnetic ion, like Yb^{3+}, at low temperatures (compared to the CEF gap) the system can be treated as an effective spin-$\frac{1}{2}$ system. This general process of angular momentum degeneracy breaking, and Kramer's theorem is demonstrated in Fig. 2.2.

An important property of the rare-earth series of elements is their similar chemical properties. All the elements from Lanthanum to Lutetium often form trivalent compounds. This similarity is due to the highly localized nature of the $4f$ orbitals. When one of the lanthanides form an ionic compound, they generally donate the two electrons in the $6s$ shell and one electron from the $4f$ shell. Only one $4f$ electron is generally donated due to the remaining $4f$ electrons seeing an effectively larger charge from the nucleus and thus the electrons generally residing even closer to the nucleus, increasing the speed the electrons have to orbit to relativistic speeds, making their participation in bonding energetically unlikely. The similarity in bonding is one of the features

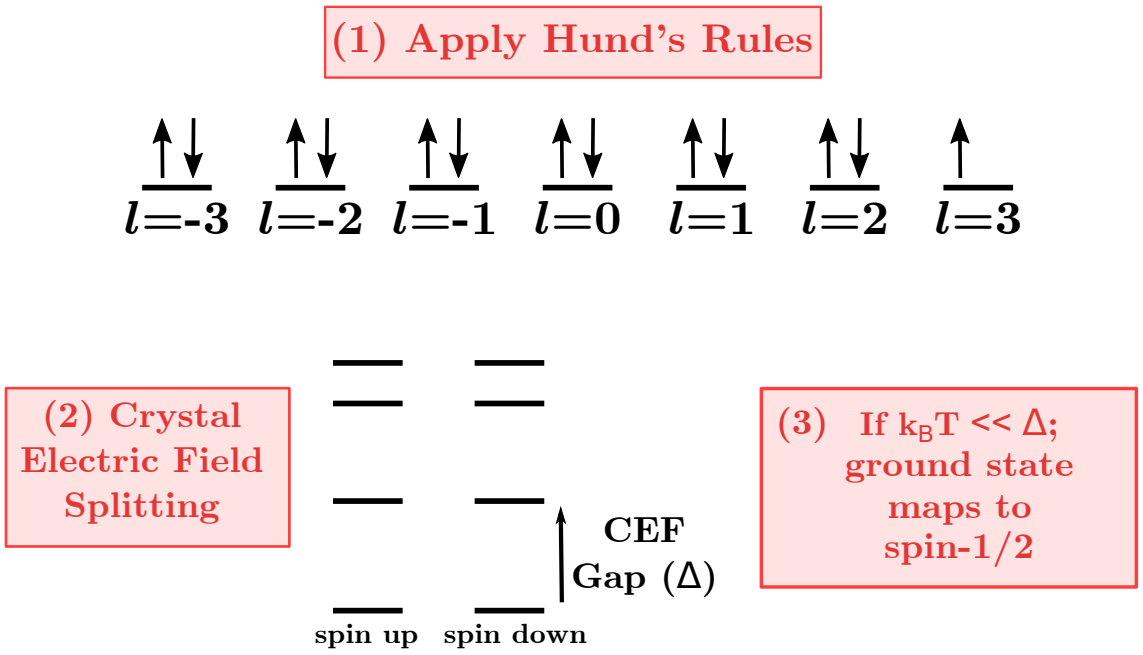

Figure 2.2: Schematic showing the process of determining the ground state properties for the Yb^{3+} rare-earth ion. First, Hund's rules are applied to put the $13f$ electrons into angular momentum states. Crystal electric field splitting is then introduced to break the degeneracy of the 8 total angular momentum states, leading to multiple sets of doublets. If the temperature of the system is much smaller than the gap to the first excited state, then the ground state can be mapped to a spin-$\frac{1}{2}$.

that makes the rare-earth series of atoms ideal for studying in quantum magnets, as one magnetic atom in the series can often easily be exchanged for a different atom (magnetic or non-magnetic) from the series. The main limitation upon this substitution is the contraction of the ionic radius from La (2.5 Å) to Lu (2.27 Å), but this also results in different structures forming for different rare-earth ions and allows for the possibility of polymorphic phase diagrams, like in the rare-earth pyrosilicates [17, 18].

2.1.2 Quantum Dimer Magnets and Bose-Einstein Condensation

Perhaps one of the simplest quantum magnet states is that of the quantum dimer magnet and could be considered the textbook example of quantum magnetism. In describing the quantum dimer magnet, let us consider a magnetic system made up of atoms with a spin of $\frac{1}{2}$ (this could be a "bare" spin-$\frac{1}{2}$ or an effective spin-$\frac{1}{2}$) and where each magnetic atom has only one nearest-neighbor

magnetic atom. If we assume that these nearest-neighbor magnetic atoms have antiferromagnetic Heisenberg exchange and only interact with their nearest-neighbor, it is possible that the spin's wavefunctions become entangled,

$$\Psi(\mathbf{r}_1, \mathbf{r}_2) = \psi_1(\mathbf{r}_1) \otimes \psi_2(\mathbf{r}_2) \tag{2.1}$$

If we focus purely on the spin component of the wavefunction, we obtain an antisymmetric wavefunction for the combined spins - a dimer - of the form,

$$\Psi_{S_z=0}(\mathbf{r}_1, \mathbf{r}_2) = \frac{1}{\sqrt{2}}(|\uparrow\downarrow\rangle - |\downarrow\uparrow\rangle) \tag{2.2}$$

This wavefunction has no total spin (S_{tot} = 0) and therefore no z-component to the spin (S_z = 0), which importantly means that the state has no net magnetization. If we then examine the triplet of (S_{tot} = 1) excited states from this singlet ground state, we obtain,

$$\Psi_{S_z=0}(\mathbf{r}_1, \mathbf{r}_2) = \frac{1}{\sqrt{2}}(|\uparrow\downarrow\rangle + |\downarrow\uparrow\rangle) \tag{2.3}$$

$$\Psi_{S_z=1}(\mathbf{r}_1, \mathbf{r}_2) = |\uparrow\uparrow\rangle \tag{2.4}$$

$$\Psi_{S_z=-1}(\mathbf{r}_1, \mathbf{r}_2) = |\downarrow\downarrow\rangle \tag{2.5}$$

This triplet state consists of a non-magnetic state (Eq. 2.3), a state that would align parallel to an applied field (Eq. 2.4), and a state that would align antiparallel to an applied field (Eq. 2.5). Practically, it is difficult to directly prove the entanglement of dimers in solid state systems, and therefore the wavefunction shown above, so generally the system is compared to the quantum dimer magnet Hamiltonian,

$$\mathcal{H} = \sum_{<i,j>} \boldsymbol{S_i} \overline{J}_{\text{intra}} \boldsymbol{S_j} + \sum_{<<i,j>>} \boldsymbol{S_i} \overline{J}_{\text{inter}} \boldsymbol{S_j} + \sum_i \boldsymbol{B} \overline{g} \boldsymbol{S_i} \tag{2.6}$$

where the first term represents the exchange interaction within the dimers (i.e. between nearest neighbor spins), the second term represents the exchange interaction between the dimers (e.g. between next-nearest neighbor spins), and the final term is the Zeeman interaction with the magnetic field. It is not a requirement that the system have a finite $\overline{J}_{\text{inter}}$ exchange, but in condensed matter systems it is highly unlikely that only the nearest neighbor exchange has a finite strength. However, it is a requirement that the intradimer ($\overline{J}_{\text{intra}}$) exchange tensor be antiferromagnetic. Systems matching these properties of the quantum dimer magnet system are numerous and can often be identified by measurement of the specific heat at low temperatures [19]. Upon cooling from high temperature, a quantum dimer magnet system should exhibit a Schottky anomaly in the specific heat at a temperature related to the strength of the exchange within the dimers. This Schottky anomaly arises from the thermal depopulation of the S_{tot} = 1 states. The quantum dimer magnet system (with $S = \frac{1}{2}$) should release $k_B \ln 4$ per dimer (where k_B is the ideal gas constant) of entropy upon passing through this Schottky anomaly. The value of this entropy arises from the number of accessible microstates to the system, which in the case of the above wavefunctions, is four. No transitions related to the magnetism would be expected to occur below this temperature, indicating that the quantum dimer magnet state is the true ground state of the system.

An important special case of the Hamiltonian in Eq. 2.6 is the one in which the exchange tensors, J_{intra} and J_{inter}, are U(1) symmetric (i.e. circularly symmetric). This could be Heisenberg exchange - where the diagonals of the exchange tensor are equal and no-off diagonal elements exist - or XXZ type exchange - where two of the diagonals are equal and no off-diagonal elements exist. If the system exhibits this type of exchange, the Hamiltonian can be usefully mapped - via the Matsubara-Matsuda transformation [20] - to one of hard-core bosons where the bosons can undergo BEC. This mapping allows for spin variables of the system to be written in terms of the variables, such as boson number, that are used in describing more traditional BEC systems in ultracold gasses. This allows for the incredible breadth of theory work performed on ultracold gas BEC systems to be leveraged on quantum dimer magnet BEC systems. A few of these mappings are: (i) The component of the spin along the applied field direction (z) maps to the boson population of the

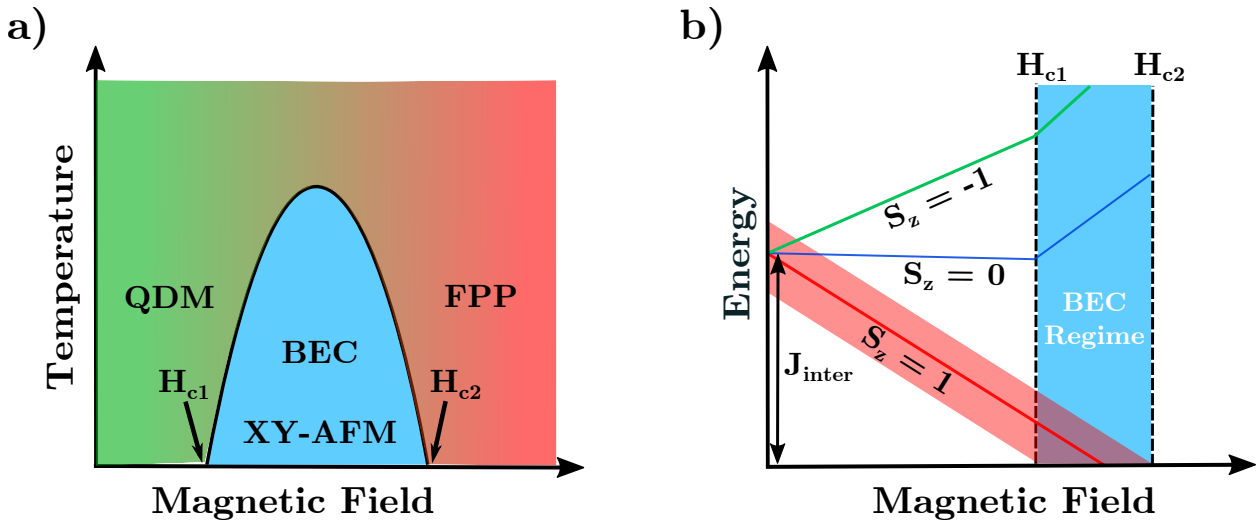

Figure 2.3: a) Example phase diagram for a weakly-coupled quantum dimer magnet system with a field-induced BEC. In the low field region, the system acts as a quantum dimer magnet (QDM). As the field passes H_{c1} the system exhibits a dome of XY antiferromagnetism, where the state can be mapped to a BEC. At fields greater than H_{c2} the system is in a field polarized paramagnet (FPP) state. b) Schematic showing the Zeeman splitting of the triplet states. The gap at zero field is determined by the magnitude of the exchange interaction, J_{inter}. The bandwidth is shown for the S_z = 1 state, as the bottom of the band reaching zero energy determines H_{c1} and the top of the band reaching zero energy determines H_{c2}. The first critical field, H_{c1} correspond to the S_z = 1 state becoming degenerate with the nonmagnetic, S_{tot} = 0, thus making the ground state doubly degenerate and therefore making it mappable to an effective spin-$\frac{1}{2}$ The second critical field, H_{c2} corresponds to the S_z = 1 state becoming the only accessible ground state in the system.

condensate. (ii) The magnetic field strength maps to the chemical potential of the BEC. (iii) An XY-like ordered state [4] maps to the BEC state. The aforementioned U(1) symmetry is required for mapping to BEC, as BEC spontaneously break U(1) symmetry. In the case of ultracold gasses, this results in the system choosing a single phase of the wavefunction, even though the physical properties of the system are not related to the phase chosen. As a result of the system spontaneously breaking the continuous U(1) symmetry, a Goldstone mode arises in the system. Goldstone modes are massless excitations that correspond to a long-wavelength fluctuation of the order parameter. In the case of quantum magnets, the choosing of a single phase corresponds to the spins ordering in one direction in the plane perpendicular to the magnetic field and the Goldstone mode corresponds to a global rotation of the spins around the magnetic field direction within the XY-ordered state.

[4] The XY state is a planar magnetic state, where the spins order in the plane perpendicular to the magnetic field and preserve their U(1) symmetry.

As the excitation is massless, it presents as a linearly dispersive excitation originating at zero momentum and energy. For the Hamiltonian shown, this BEC manifests as a dome in the magnetic field vs. temperature phase diagram, as shown in Fig. 2.3a. At low magnetic fields, the system is in the quantum dimer magnet state, so no magnetic ordering is observed, but coherent excitations to the triplet states (called triplons) can be measured via inelastic neutron scattering. As the strength of the magnetic field increases, the triplet of excited states Zeeman split in energy, with the S_z = 1 state being driven down towards zero energy, shown in Fig. 2.3b. In the presence of a finite J_{inter} exchange the triplet of states are not at discrete energies, but instead have a dispersion (bandwidth) with the width of J_{inter}. It is this bandwidth that determines the critical fields (H_{c1} and H_{c2}) where the system undergoes a quantum phase transition into and out of an XY ordered state, respectively. When the bottom of the S_z = 1 band reaches zero energy the ground state of the system is now a degenerate state with the S_{tot} = 0, S_z = 0 and S_{tot} = 1, S_z = 1 states. This degenerate ground state allows for the Hamiltonian in Eq. 2.6 to be rewritten in terms of an effective spin-$\frac{1}{2}$system, with the S_{tot} = 0, S_z = 0 corresponding to "spin" down and the S_{tot} = 1, S_z = 1 corresponding to "spin" up. In bosonic language these states correspond to the absence of a boson (spin down) on a dimer or the presence of a boson (spin up) on a dimer. As the magnetic field (chemical potential) is increased bosons begin to populate the dimers until at H_{c2} all dimers are in the spin up state and the system is then a field-polarized paramagnet. The usefulness of this bosonic description for a quantum magnet may not be apparent at first, but due to the mapping to language used for traditional BEC's a large amount of theoretical work can be leveraged towards understanding these systems. The quantum magnet BEC acts as a playground for understanding BEC physics that cannot be easily replicated in ultracold gasses, such as easily modifying the chemical potential. Additionally, due to the underlying symmetries of the lattice (amongst others) the description of quantum magnets as BEC's is only approximate since the U(1) symmetry is always broken at some temperature scale. This allows for the bounds of the theory of BEC to be probed and can give rise to novel physics, such as the Bose glass state [21] or boson crystallization [22], amongst others.

Overall, BEC in quantum magnets provides a useful theoretical jumping off point for discovering and understanding new phases of quantum matter, like the elusive quantum spin liquid state.

2.1.3 Transverse Field Ising Model

Perhaps one of the most ubiquitous models combining statistical mechanics and magnetism is that of the Ising model. The Ising model consists of spins arranged on a lattice with the spins coupled via an Ising exchange, therefore they can only align parallel or antiparallel (i.e. along a preferred quantization axis, generally referred to as the Ising or easy axis). The physics of this model vary depending upon the dimensionality, for example the one-dimensional Ising model does not magnetically order at any temperature whereas the two-dimensional Ising model does magnetically order [23]. This model is theoretically tractable, making it an excellent system for comparison to experimental systems. If an external magnetic field perpendicular to the Ising direction is introduced to the simple Ising model, the model can remain theoretically tractable, but can only be exactly solved in one dimension and ultimately gives rise to a quantum phase transition. In the case of a spin-$\frac{1}{2}$ Ising chain, the Transverse Field Ising Model (TFIM) Hamiltonian has the form,

$$\mathcal{H} = -\sum_{<i,j>} J\sigma_i^z\sigma_j^z - h\sum_i \sigma_i^x \tag{2.7}$$

where J is the exchange between nearest neighbor spins, $\sigma_{i,j}$ is the Pauli spin matrix for the spin at site i or j, and h is the magnetic field. This model gives rise to a quantum phase transition due to the Pauli spin matrices, σ^z and σ^x, not commuting with one another. Thus, whereas the classical Ising model phase transition is driven by entropy, the *quantum* phase transition in the TFIM is driven by the uncertainty principle. The magnetic field vs. temperature phase diagram for the one-dimensional ferromagnetic TFIM (shown in Fig. 2.4) has a low field regime where the first term of the Hamiltonian dominates and the system exhibits a ferromagnetic state (when J is positive) with the spins parallel to the z direction. At zero temperature and as the magnetic field strength is increased, the two terms of the Hamiltonian become comparable in magnitude and there will be a quantum phase transition when their energies are equal. Past this quantum phase transition,

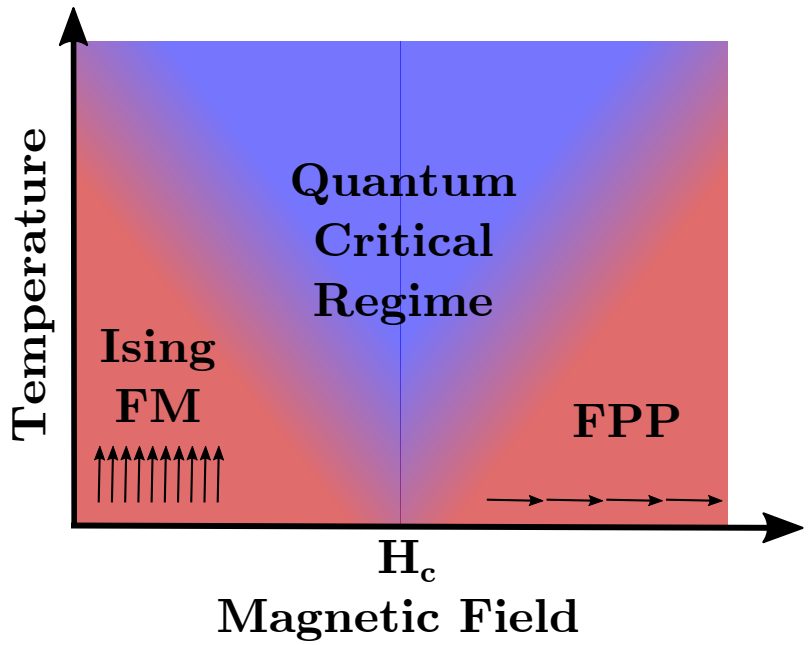

Figure 2.4: Phase diagram for the ferromagnetic one-dimensional TFIM. At low fields the system is in a ferromagnetic state with the spins aligned along the Ising direction. At T = 0 and a critical field (H_c) the system undergoes a quantum phase transition to a field polarized paramagnet (FPP) state. At finite temperatures, this quantum phase transition manifests as a quantum critical regime with the edges of the regime dictated by the critical exponents of the TFIM.

the second term in the Hamiltonian is dominant and therefore the spins are polarized along the magnetic field direction, x. While this Hamiltonian is relatively simple, very few experimental examples exist to date. This lack of experimental examples may seem surprising at first due to the relative simplicity of the model, but in the known experimental examples there are complicating processes that allow the system to deviate from strict TFIM behavior. One such case is in the quasi-one dimensional TFIM compound $CoNb_2O_6$, where interchain couplings allow for three-dimensional long-range order that can mask the effects of the one-dimensional TFIM quantum critical point [24]. In light of the theoretical tractability of this model, new systems exhibiting these properties are highly desired and motivate our study of D-$Er_2Si_2O_7$ in Chapter 4.

2.2 Experimental Techniques

2.2.1 Neutron Scattering

In 1932, James Chadwick published a short letter in *Nature* describing experiments on the recoil of different atoms from beryllium radiation [25]. Based on arguments of conservation of momentum and energy, Chadwick was able to deduce that this radiation could only come from a charge 0, mass 1 particle; in direct contradiction to separate findings by Bothe and Becker [26] and the Joliot-Curie's [27] who believed the beryllium radiation consisted of gamma rays. This particle Chadwick discovered was the neutron. The discovery of the neutron directly led to the discovery of artificial radioactivity and later the development of the first nuclear bomb. A less well-known product of Chadwick's discovery is the development of neutron scattering. Neutron scattering is a wide encompassing term, which generally describes experiments where low energy (meV-keV) neutrons are directed at a sample - which they interact with - and then the neutrons resulting energy and momentum are analyzed. The development of neutron scattering was started at Oak Ridge National Laboratory (at the time Clinton Laboratories) where Ernest Wollan and Lyle Borst performed the first measurements on a powder sample of calcite using a modified X-ray diffractometer [28]. This experiment quickly led to the first neutron Laue photographs, evidence of antiferromagnetism, and numerous other developments. As Ernest Wollan quickly learned, neutrons are the ideal probe for condensed matter systems due to their wavelength and energy relation serendipitously matching the spacings of atomic lattices and the energy scale of condensed matter excitations (e.g. phonons). This wavelength and energy can also be tuned to allow for application to systems of different sizes, such as biological systems or large polymer chains. In addition to the beneficial wavelength and energy relation of neutrons, the neutron's absence of a net charge allows them to probe the bulk of a sample and their spin (a result of their up-down-down quark structure) allows them to probe magnetic properties of materials. In the 74 years since Wollan's experiments, neutron scattering has advanced significantly in terms of theoretical understanding, instrumentation, and data analysis.

Before discussing neutron scattering theory, it is worthwhile to mention how neutrons are generated. Two types of sources are currently in use: spallation sources and nuclear reactor sources. Nuclear reactor sources generate neutrons by the fissioning of uranium and provide a steady source of neutrons. The neutrons released by the uranium are generally at very high energies (MeV) and energies of meV are needed for neutron scattering, so the neutrons need to pass through a moderator (sometimes multiple moderators) before reaching a sample. The moderator is typically water or heavy water [5] which slows the neutrons down via inelastic collisions. The neutrons leave the moderator at the same temperature as the moderator, where the effective temperature of the neutrons is described by a Boltzmann distribution. This moderation of neutrons reduces their energies - and therefore wavelengths - to those that are applicable to measuring materials. The neutrons are generally classified into three different effective temperature ranges; cold, thermal, and hot. Cold neutrons have an energy of 0.1 - 10 meV, thermal neutrons have an energy of 5 - 100 meV, and hot neutrons have energy of 100 - 500 meV. Many instruments are specialized for one of these temperature ranges to maximize flux of a specific energy. Contrary to nuclear reactor sources, spallation sources (generally) emit pulsed beams of neutrons. The neutrons in spallation sources are created by colliding relativistic protons with a target [6]. The neutrons exiting the target must be moderated via similar methods as the reactor source due to their high energies. A pulsed spallation source - like those used for this work - leads to a lower time averaged flux of neutrons, but also makes analyzing the time-of-flight of the neutrons much simpler. Spallation sources also have the societal benefit of limiting nuclear proliferation as they do not require uranium to generate neutrons. Overall, spallation and nuclear reactor sources have their own benefits and downfalls, but both are vital tools in the neutron scatterer's toolbox.

[5]Heavy water is water where the natural abundance hydrogen with no neutrons in the nucleus is replaced with deuterium atoms with one neutron in the nucleus.

[6]In the case of the venerable Spallation Neutron Source at Oak Ridge National Laboratory, the target is liquid mercury

Neutron Scattering Theory

As seen in the previous section, neutron scattering has proven to be a reliable tool for investigating condensed matter systems. This is primarily due to the non-relativistic energies used and the weak or short-range interactions the neutron experiences when scattering off a condensed matter system. These properties of the scattering allow for the use of Fermi's Golden Rule, the Born approximation, and ignoring relativistic properties [7]. Numerous textbooks have been written on neutron scattering theory and experiment. My description of neutron scattering theory is guided by two books, *Neutron Scattering from Magnetic Materials* edited by Tapan Chatterji [29] and *Introduction to the Theory of Thermal Neutron Scattering* by G. L. Squires [30]. The theoretical treatment I will show in this section is primarily based off the latter. I will not attempt to repeat all the derivations performed by G. L. Squires, but I will quote results and explain why those results make sense and what approximations are needed to reach them.

The first step to understanding neutron scattering theory is to consider how neutrons are measured, as that is what the theory will be compared to. The neutrons impinging upon the sample have a probability of interacting with the sample that can be expressed as a cross section, σ. To detect neutrons, we can imagine placing a detector somewhere around the sample that the neutrons will be scattering off. However, we will only be measuring a portion of this cross section, $d\sigma$, as the detector is of finite size so it takes up a solid angle, $d\Omega$, of the sphere that the neutrons could be scattered into. We can additionally design the experiment to have the detector select for a single energy of neutrons, dE'. Our detector will then measure the number of neutrons per unit time, Φ, in that solid angle $d\Omega$ with energy dE'. This value the detector measures is called the double differential cross section,

$$\frac{d^2\sigma}{d\Omega dE'} \tag{2.8}$$

[7] In most cases of neutron scattering Fermi's Golden Rule and the Born approximation are equivalent due to only s-wave scattering being considered. Only s-wave scattering is allowed because the object being scattered off of (electrons or a nucleus) are significantly smaller than the wavelength of the neutrons and therefore the scattering must be spherically symmetric. A common place where this does not apply is in neutron reflectometry, as reflectometry utilizes refraction instead of diffraction.

this double differential cross section is fundamental to the neutron scattering theory and virtually every theoretical result can be traced back to this. The double differential cross section tells us what our detector is measuring, but to garner useful information we must know what this is equivalent to. More precisely, we must have some prediction for how the physics of our scattering system will scatter neutrons into this detector. To understand this, we can think about the cross section as a sum of all the processes in which the total scattering system (the neutron plus the sample) where the system changes from wavelength λ to λ' and consequently momentum **k** to **k'** [8]. We can write this cross section (called just the differential cross section) as,

$$\frac{d\sigma}{d\Omega} = \frac{1}{\Phi}\frac{1}{d\Omega}\sum_{\mathbf{k}' \text{ in } d\Omega} W_{\mathbf{k},\lambda\to\mathbf{k}'\lambda'} \tag{2.9}$$

where Φ is the flux of incident neutrons and $W_{\mathbf{k},\lambda\to\mathbf{k}'\lambda'}$ is a generic term for the number of transitions per second from the state **k**, λ to the state **k'**, λ'. This is where Fermi's Golden Rule becomes applicable. As a reminder, Fermi's Golden Rule describes the probability of a transition per second from one energy eigenstate to a group of energy eigenstates, as a result of a weak pertubation. Due to nuclear forces being very strong forces; one may think that Fermi's Golden Rule does not apply. However, due to the nuclear potential being incredibly short range *and* only *s*-wave scattering being possible, Fermi's Golden Rule is still valid for neutron scattering. Applying Fermi's Golden Rule to Eq. 2.9 yields,

$$\sum_{\mathbf{k}' \text{ in } d\Omega} W_{\mathbf{k},\lambda\to\mathbf{k}'\lambda'} = \frac{2\pi}{\hbar}\rho_{\mathbf{k}'} |\, \langle \mathbf{k}'\lambda'|V|\mathbf{k}\lambda\rangle \,|^2 \tag{2.10}$$

upon substitution of this in Eq. 2.9, application of box normalisation, and enforcement of conservation of energy we can arrive at the master equation in neutron scattering,

$$\left(\frac{d^2\sigma}{d\Omega dE'}\right)_{\lambda\to\lambda'} = \frac{k'}{k}\left(\frac{m}{2\pi\hbar}\right)^2 |\, \langle \mathbf{k}'\lambda'|V|\mathbf{k}\lambda\rangle \,|^2 \delta(E_\lambda - E_{\lambda'} + E - E') \tag{2.11}$$

[8] We will consider the process of scattering from E to E' shortly

the primary assumption made to reach this master equation is simply that Fermi's Golden Rule applies, i.e. no assumptions otherwise have been made about the potential, V. We can then limit ourselves to a short-range potential, such as,

$$V(\mathbf{r}) = \frac{2\pi\hbar^2}{m}\, b\, \delta(\mathbf{r}) \tag{2.12}$$

where *b* is the scattering length, which describes the nature of the scattering. This potential is known as the Fermi pseudopotential and has proven to be a good potential for describing nuclear scattering. If *b* is positive the potential is considered repulsive and if *b* is negative the potential is considered attractive, although this is not indicative of the attractive/repulsive nature of the *actual* potential of the system. If we consider how this potential would look for a system of identical nuclei, we obtain a potential of the form,

$$V_j(\mathbf{Q}) = \frac{2\pi\hbar^2}{m} b_j \tag{2.13}$$

by plugging this potential into Eq. 2.11, converting the delta function to an integral, summing over λ', and averaging over λ we arrive at the basic expression for the differential cross section for neutron scattering off a system of identical nuclei,

$$\left(\frac{d^2\sigma}{d\Omega dE'}\right)_{\lambda\to\lambda'} = \frac{k'}{k}\frac{1}{2\pi\hbar}\sum_{jj'} b_j b_{j'} \int_{-\infty}^{\infty} \langle \exp\{-i\mathbf{Q}\cdot\mathbf{R}_j(0)\}\exp\{-i\mathbf{Q}\cdot\mathbf{R}_j(t)\}\rangle \times \exp(-i\omega t)\, dt \tag{2.14}$$

where b_j is the scattering length of the jth atom, **Q** is the scattering vector (i.e. **k** - **k**', shown in Fig. 2.5), and $\mathbf{R}_j$(t) is the position vector of the jth nucleus. If we then consider the scattering as being from an ensemble of nuclei where the scattering length varies - due to isotope and/or nuclear spin - and there is no correlation between scattering lengths we can rewrite the $b_j b_{j'}$ term as an average over all the scattering lengths: $\overline{b_j b_{j'}}$. For values in the sum where $j \neq j'$ this average is equal to $(\overline{b})^2$ and for values where $j = j'$ this average is equal to $\overline{b^2}$. This allows the differential

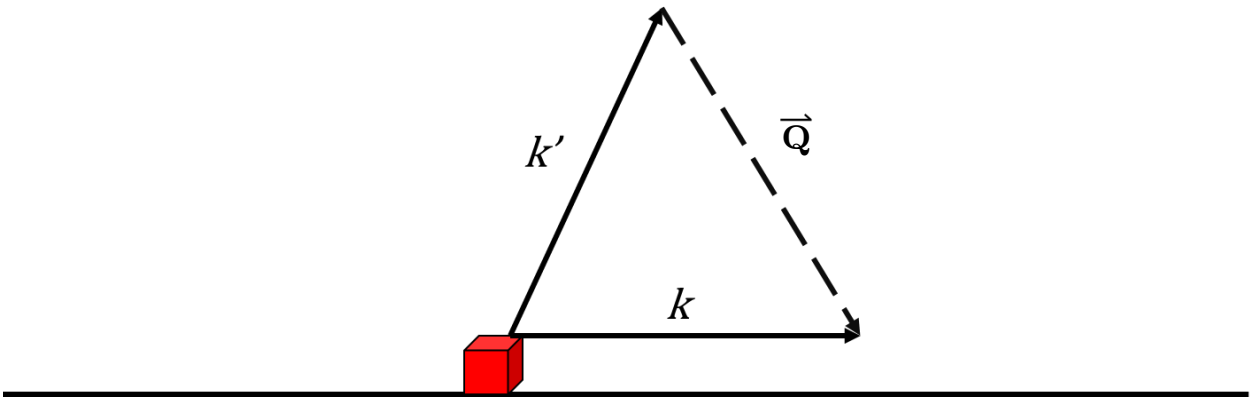

Figure 2.5: Diagram showing how the scattering vector **Q** relates to the neutron's incoming (*k*) and outgoing (*k'*) momentum. The red cube indicates the sample position.

cross section to be split into two different terms, one where the sum is over j and j' and one where the sum is just over j. The former depends on the correlation between the position of the same nucleus at different times and the correlation between the positions of different nuclei at different times, generally referred to as the coherent cross section due to this term being responsible for interference effects. The latter depends *only* on the correlation between the same nucleus at different times, generally referred to as the incoherent cross section. Some examples of coherent scattering processes are magnons, phonons, and diffraction. Some examples of incoherent scattering processes are atomic diffusion or crystal field excitations, essentially any single particle process.

With a basic understanding of neutrons scattering off nuclei, we now concern ourselves with how the neutron interacts with unpaired electrons in a system, i.e. magnetic neutron scattering. In comparison to nuclear neutron scattering, magnetic neutron scattering is interesting as the interaction potential is known to be,

$$\mathbf{V}(\mathbf{r}) = -\gamma\mu_N 2\mu_B \boldsymbol{\sigma} \cdot \left[\nabla \times \left(\frac{\mathbf{s} \times \hat{\mathbf{R}}}{R^2}\right) + \frac{1}{\hbar}\frac{\mathbf{p} \times \hat{\mathbf{R}}}{R^2}\right] \tag{2.15}$$

where γ is the neutron gyromagnetic ratio, μ_N is the nuclear magneton, μ_B is the Bohr magneton, $\boldsymbol{\sigma}$ is the Paul spin operator, $\mathbf{s}$ is the spin angular momentum operator of the electron, $\mathbf{R}$ is the distance from the electron to the neutron, and $\mathbf{p}$ is the momentum of the electron. The first term in this equation is due to the spin of the electron - i.e. the magnetic field of the electron at the

position of the neutron - and the second term is due to the orbital motion of the electron. In order to calculate the double differential cross section (Eq. 2.11) for magnetic scattering, this potential must be used to evaluate the matrix elements of $\langle \mathbf{k}'\lambda'|V|\mathbf{k}\lambda\rangle$. The evaluation of these elements consists of utilizing box normalization again, assuming the neutron is a plane wave, and Fourier transforming to reciprocal space. In the case of my work, we have only utilized unpolarized neutron scattering so I will be quoting the differential cross section with the sum over the final polarization (σ') and wavelength (λ') and the average over the intial polarization (σ) and wavelength (λ) states already performed, similar to what was needed to get to Eq. 2.11. Thus, the double differential cross section for magnetic neutron scattering is,

$$\frac{d^2\sigma}{d\Omega dE'} = r_0^2 \frac{k'}{k} |\frac{g}{2} F(Q)|^2 \sum_{\alpha\beta} (\delta_{\alpha\beta} - \hat{Q}_\alpha \hat{Q}_\beta) \times \frac{1}{2\pi\hbar} \int dt\, e^{i\omega t} \frac{1}{N} \sum_{\mathbf{RR'}} \langle S^\alpha_{\mathbf{R}}(t) S^\beta_{\mathbf{R'}}(0)\rangle\, e^{-i\mathbf{Q}\cdot(\mathbf{R}-\mathbf{R'})} \tag{2.16}$$

where α and β refers to the Cartesian coordinates *x, y, z*, g is the g-factor for the spin being measured, r_0 is the classical radius of the electron, $F(Q)$ is the magnetic form factor for the magnetic species being probed, $\hat{Q}_{\alpha,\beta}$ is the x, y, z components of **Q**, and $\langle S^\alpha_{\mathbf{R}}(t) S^\beta_{\mathbf{R'}}(0)\rangle$is the spin-spin correlation function, which will be elaborated on shortly. There are two important notes regarding this equation: 1) The term within the integral and the sum corresponds to the Fourier transform of the spin-spin correlation function. 2) The scattering is directionally dependent, as the neutron only probes the components of the magnetization perpendicular to the momentum transfer (**Q**). These properties allow for the determination of complex magnetic structures in single crystal materials (along with "normal" magnetic structures).

This naturally leads to the discussion of correlation functions. The power of correlation functions in neutron scattering come from the difficulty in precisely knowing the interaction potential. If we return to Eq. 2.14, but focus purely on the coherent part we can introduce the intermediate scattering function,

$$I(\mathbf{Q},t) = \frac{1}{N}\sum_{jj'}\langle \exp\{-i\mathbf{Q}\cdot\mathbf{R}_{j'}(0)\}\exp\{i\mathbf{Q}\cdot\mathbf{R}_{j}(t)\}\rangle \tag{2.17}$$

where N is the number of nuclei in the scattering systems. From this definition we can then introduce the time-dependent pair correlation function,

$$G(\mathbf{r},t) = \frac{1}{(2\pi)^3}\int I(\mathbf{Q},t)\exp(-i\mathbf{Q}\cdot\mathbf{r})d\mathbf{Q} \tag{2.18}$$

While this equation may seem ambiguous, it is quite powerful. A pair correlation function describes how two nuclei are correlated in space and time. This is something that is conceptually tractable and in many cases, this can be calculated to compare with experiment. In addition, we can introduce the scattering function, often known as the dynamic structure factor,

$$S(\mathbf{Q},\omega) = \frac{1}{2\pi\hbar}\int I(\mathbf{Q},t)\exp(-i\omega t)dt \tag{2.19}$$

which is simply the Fourier transform of $G(\mathbf{r}, t)$ in space and time. The variables of $S(\mathbf{Q}, \omega)$ relate to what is measured in actual neutron scattering experiments much better, as neutron scatterers generally work in momentum space and energy (or frequency ω) space, rather than position and time. In the case that one cannot derive an exact expression for these functions, the analytic properties of these functions need to be known. There are numerous analytic properties that I will not discuss, but perhaps the most important one for a neutron scatterer to know is,

$$S(\mathbf{Q},\omega) = \exp(\hbar\omega\beta)S(-\mathbf{Q},-\omega) \tag{2.20}$$

where β is the thermodynamic $\beta = \frac{1}{k_B T}$. This is called the principle of detailed balance and relates the signal from the positive energy transfer (where the neutron gives energy to the scattering system) to the negative energy transfer (where the neutron takes energy from the scattering system). In practice this allows for the determination of the temperature of the system (or possibly subsystem) to compare with measurements by a thermocouple placed near the sample. This also puts a constraint on analytic expressions for the correlation function. Correlation functions are incredibly

useful for modeling magnetic structures, spin waves, and understanding novel magnetic states - such as the elusive quantum spin liquid - due to the neutron directly probing the magnetization density of the system.

In summary, neutron scattering theory is incredibly deep set of calculations, of which I have only given the major points. The major points to remember from this are: (i) Most of neutron scattering lies within the Born approximation/Fermi's Golden rule. This makes the theory of neutron scattering approachable to the average physicist. (ii) Scattering processes can be separated into two different kinds: coherent and incoherent. These two different processes have different cross sections and therefore can allow for analyzing the properties of a specific element in a system (such as hydrogen which has a large incoherent cross section). It is also important to keep these cross sections in mind when planning an experiment, as some isotopes have large incoherent cross sections that will mask the coherent signals one may be looking for. (iii) It is difficult to know the precise potential and/or Hamiltonian of the scattering system, so the concept of correlation functions is quite powerful, as it is often easier to understand how particles are correlated instead of knowing every eigenstate and the probability of transition between them.

Neutron Scattering Experiment

Now that we have developed a basic understanding of the theory behind neutron scattering, we concern ourselves with experimental aspects of neutron scattering. In neutron scattering, data can generally be thought of as four-dimensional; where one dimension is energy transfer and the other three are the components of the scattering vector, $\mathbf{Q}$. Note, the basis for $\mathbf{Q}$ is (generally) related to the reciprocal axes of the crystal system and therefore need not be an orthogonal basis [9]. One of the simplest, and still useful, neutron experiments one could perform is one in which a monochromatic neutron beam is scattered from a powder sample and the neutron's final energy is not analyzed. This limits the dimensions of the dataset to just the magnitude of the scattering vector ($|\mathbf{Q}|$). Though this is an energy-integrated measurement (e.g. the final neutron energy is not

[9] This is the case for all the systems I have presented in this work.

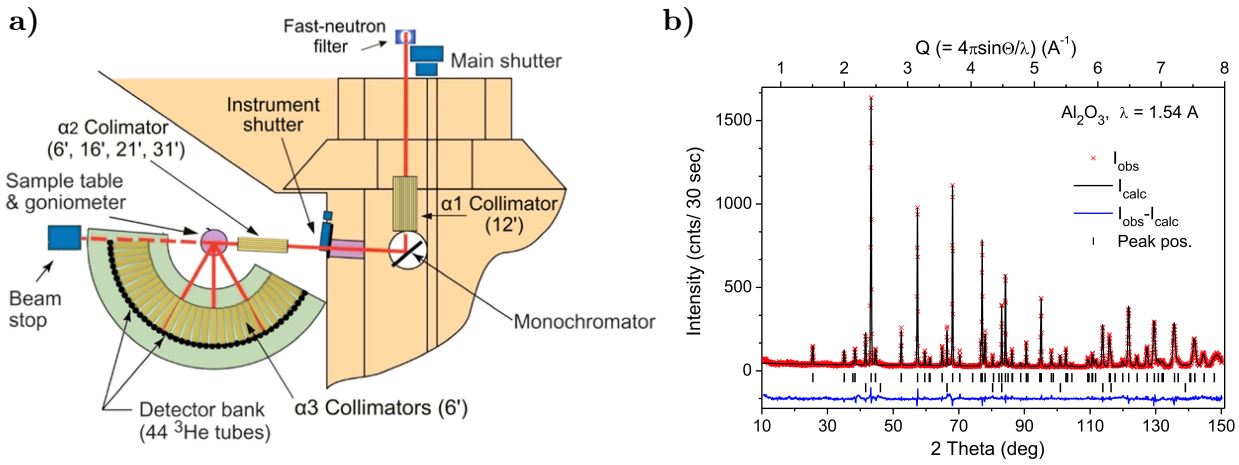

Figure 2.6: a) Diagram of the HB-2A powder diffractometer at Oak Ridge National Laboratory. b) Powder diffraction pattern for Al_2O_3 measured on HB-2A. Both panels were obtained from reference [31].

selected for) the measurements are generally thought of as elastic, as elastic scattering is generally orders of magnitude more intense than the inelastic scattering. This is exactly the method used in powder diffractometers for solving the simple magnetic structures and nuclear structures of powdered materials.

A diagram for a typical powder diffractometer (HB-2A at Oak Ridge National Laboratory) is shown in Fig. 2.6a. Following the beam from the reactor, the beam first encounters a fast-neutron filter. In this instrument the fast-neutron filter is made of a liquid nitrogen cooled sapphire filter. This filter works by having a very low scattering cross section for thermal neutrons (< 0.1 eV) and a very high cross section for neutrons of higher energies. This allows for the thermal neutrons to go through the sapphire filter with a small chance of interacting, whereas, high energy neutrons will likely interact with the sapphire filter and be scattered randomly out of the beam. The neutron beam then encounters a collimator (labeled $\alpha 1$) whose purpose is to limit the divergence of the beam. Limiting the beam divergence is important as this directly translates to the resolution in momentum ($|\mathbf{Q}|$) space. These collimators are generally Söller collimators which consist of parallel blades often made of Cd or Gd painted mylar with a carefully measured separation between the blades that determines the angular divergence the exiting neutron beam can have [10]. The neutron beam

[10]Cd or Gd are used because they are incredibly strong neutron absorbers.

then encounters a monochromator crystal, often made of single crystals of silicon, germanium, or pyrolytic graphite. These crystals are cut very precisely along a particular lattice direction and placed in the neutron beam. Since the crystal has been carefully aligned, only one crystallographic reflection will redirect the neutrons to the sample, so only one wavelength is reflected towards the sample as described by Bragg's law. In the case of HB-2A, the beam goes through another collimator to further improve resolution before impinging upon the sample. Most neutrons will not interact with the sample, but those that do can be scattered off the crystallographic and/or magnetic planes and into one of the detectors of the instrument. A bank of detectors made of ^{3}He gas-filled tubes is used for fast data acquisition and the whole set of detectors is moved through the necessary angular range. An experiment on this instrument gives a data set like the one shown in Fig. 2.6b. The pattern shown is for Al_2O_3 and shows very sharp peaks corresponding to the Bragg reflections of the system. This pattern can then be used to solve the structure of the system via Rietveld refinement. If the system is magnetic, two patterns must be taken to accurately solve the magnetic structure, one above the ordering temperature and one below the ordering temperature. This will allow for the isolation of the magnetic scattering and then a Rietveld refinement of the symmetry allowed magnetic structures can be performed. In the case that one needs to measure the diffraction off a single crystal, the same instrument could be used when combined with a rotating sample stage. This allows for the rotation of the sample to find different Bragg peaks within the angular range of the instrument. In practice, powder diffractometers are not generally used for this as the bank of detectors is no longer as useful. For this reason, a triple axis spectrometer or a special made diffractometer are used for measurements of elastic scattering from single crystals.

Adding the dimension of energy to our desired experimental variables adds significant complexity to neutron scattering measurements. If we do not select for energy, then we only must concern ourselves with putting detectors where neutrons are scattered to. In the case that we want to know the energy that the neutrons transmitted/received from our scattering system we must determine a way to select for a single energy of the neutron before detecting it. There are generally two ways to select for final energy: the analyzer crystal method and time-of-flight method. The

analyzer crystal method is essentially the same as how the monochromator works for selecting the incident energy, however, the analyzer crystal can easily be adjusted to different angles to allow for different energy transfers. These types of analyzers are generally used on triple-axis spectrometers. The other method for selecting final energy is via the time-of-flight method. In the time-of-flight method a set of choppers (rotating, neutron absorbing discs with a slot cut into them) are put in the path of the beam. These choppers are then rotated at a frequency that only neutrons of a single energy can make it through all the slits and make it to the sample. This essentially does the same thing as the monochromator crystal but can also be used to pulsate the beam for a steady-state reactor source, allowing reactor sources to leverage the benefits of time of flight neutron techniques that spallation sources often utilize. In order to get the final energy, a low efficiency monitor is put in the path of the beam to monitor measure "t0" (the time at which we start our theoretical stop watch) and then we simply time stamp events when the detector detects a neutron. If pulses do not overlap - known as frame overlap - we then know how long it took the neutrons to make it from the monitor to the detector. As we know the neutron's energy from the monitor to our sample, we know how long they take to reach the sample. This allows us to deduce the time it takes for the neutron to travel from our sample to the detector and since we know the distance from the sample to the detector, we can get the neutron's speed. This speed is related to the energy of the neutron and thus we can know the energy of the neutron after it interacted with our sample.

A diagram of the Cold Neutron Chopper Spectrometer (CNCS) is shown in Fig. 2.7a and I will go through the purpose of all the parts shown, as it is useful to understand the instrumentation when analyzing the data. Starting from the bottom left of Fig. 2.7a, the neutron encounters a curved neutron guide on its way to the sample. This curved neutron guide is used to reduce the amount of high-energy and thermal neutrons that make it to the sample (this instrument utilizes cold neutrons). This guide is coated in a neutron "supermirror" material which keeps the neutrons traveling towards the sample. The first chopper that the neutron encounters in this guide is the Fermi chopper. The Fermi chopper consists of many curved blades and spins with its angular momentum perpendicular to the beam. The purpose of this chopper is to shape the neutron beam

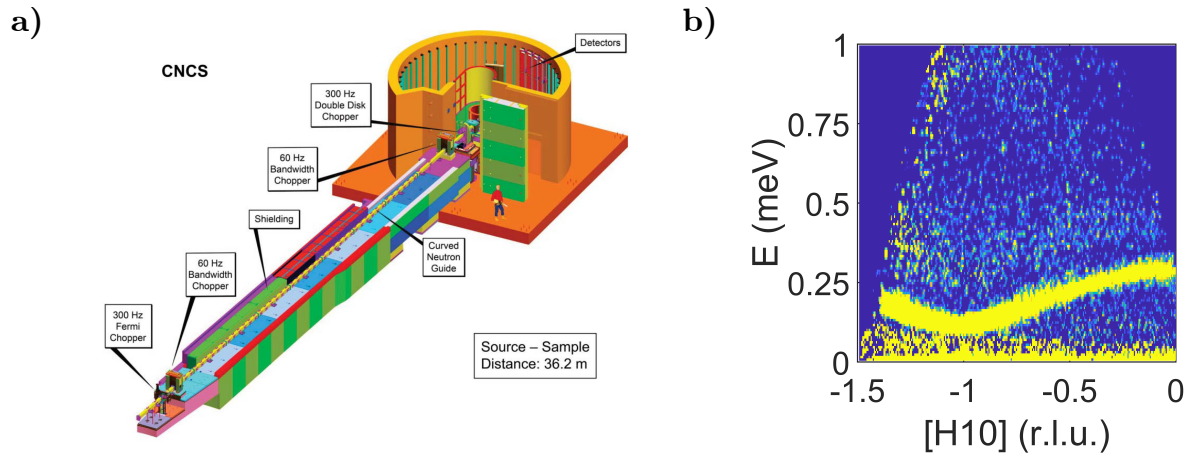

Figure 2.7: a) Diagram of the Cold Neutron Chopper Spectrometer at Oak Ridge National Laboratory (Figure from reference [32]). b) A typical inelastic neutron scattering spectra measured on CNCS. The color corresponds to the number of neutrons counted with blue being no neutrons and yellow being a lot of neutrons. The x-axis is in reciprocal lattice units corresponding to the system measured, $Yb_2Si_2O_7$ this can be thought of as momentum transfer along a certain lattice direction. The y-axis corresponds to the energy the neutron lost to the scattering system. Data reproduced from [7].

pulse, essentially shortening the pulse from the spallation source, as the length of the initial pulse is generally too long for most of the desired applications. The neutron then encounters two 60 Hz bandwidth choppers. These choppers are responsible for preventing the aforementioned frame overlap. The neutron then encounters a double-disk chopper which determines the average neutron energy and resolution bandwidth by the relative phase between the openings in the chopper and the size of the openings, respectively. The neutron then encounters the sample and, in the case that it interacts with the sample it is (possibly) scattered off towards the semi-circular array of detectors. The detectors are tubes of ^{3}He with position discrimination, which allows for an approximate +/- 16° out of plane coverage and a coverage of -50° to 135° in the scattering plane. This instrument generates a massive amount of data ($\sim$terabytes) through the course of an experiment that later must be analyzed. When the four-dimensional data set is reduced and formatted it is generally displayed in slices (2D) and cuts (1D), an example of the former is shown in Fig. 2.7b. This data shows a triplon excitation from the quantum dimer magnet system, $Yb_2Si_2O_7$. A similar signal would be expected for a magnon from a simple antiferromagnetic system. Numerous spectra similar to this will be shown later in this work, so it is useful to provide some tips for looking at the

data: (i) The plain blue sections of data around the edges can be ignored, as that is simply where no detectors exist to measure neutrons. (ii) The yellow (high intensity) signature at 0 meV is the elastic scattering. It is very high intensity due to the much higher cross section for elastic scattering compared to inelastic scattering. The elastic scattering measured on a spectrometer like this can be important, but for plots like this can be ignored. (iii) The important features are generally the bright excitations at finite energy (although the excitations can reach zero energy depending upon the nature of the excitation), how the dispersion changes with momentum transfer, and how these excitations evolve with temperature, field, etc. Overall, neutron scattering has proven to be integral to this work - showing up in the three papers presented in Chapters 3-5 - and will continue to be useful for tackling the most cutting-edge problems in condensed matter physics.

2.2.2 Heat Capacity

Measurements of a sample's heat capacity is a one of the best methods for analyzing the phase transitions predicted by Landau's theory of phase transitions, likely due to the relative simplicity of heat capacity and its measurement. Landau's theory of phase transitions is powerful for analyzing phase transitions as it starts with two simple conditions: (1) The free energy is an analytic function of an order parameter, ν. An order parameter is zero in the disordered state and one in the ordered state, in a ferromagnetic system this would be the magnetization. (2) The free energy obeys the symmetry of the Hamiltonian. From these assumptions, one can expand the free energy through a Taylor expansion in terms of the order parameter. The order parameter is a measure of the order of the system, so it is zero in the disordered phase and non-zero in the ordered phase. In the case of magnetism, this could be the total magnetization of a ferromagnetic system as the system is cooled, as the magnetization is zero in the paramagnet phase and non-zero in the ordered state. While this analysis may sound simple, it is incredibly powerful in analyzing first- and second-order phase transitions, particularly through the concept of universality. Universality is the phenomena of - seemingly disparate - systems obeying the same critical scaling laws in the vicinity of a phase transition. This phenomenon arises due to the properties of a system in the vicinity of a phase

transition only relying upon a few physical observables, such as the symmetry and dimensionality of the system. This concept of universality is prevalent throughout this work, as this concept of universality is vital to the BEC physics discussed both in Chapter 2.1.2 and Chapter 3.

Mathematically, heat capacity (at constant pressure) is defined by,

$$C_P = \left(\frac{dQ}{dT}\right)_P = -T\left(\frac{\partial^2 F}{\partial T^2}\right)_P \tag{2.21}$$

where dQ is an infinitesimal heat change, dT is an infinitesimal temperature change, F is the Helmholtz free energy of the system, and C_p is the constant pressure heat capacity. To measure this heat capacity, a sample is loaded onto a sensitive calorimeter that is weakly thermally coupled to a thermal bath. A heat pulse of a defined power - *generally* small enough to remain in the quasi-adiabatic regime - is then applied to the sample and the sample's temperature is measured as a function of time, as shown in Fig. 2.8a. The heat pulse is a step function, where a constant power is supplied to the heater until the sample reaches the desired temperature rise (often 2% of the sample's starting temperature) and the heater is then turned off, allowing the sample to return to thermal equilibrium with the bath. In the case of the Quantum Design Heat Capacity option used in this work [33], this temperature curve can then be fit by solving the differential equation [11],

$$C_{\text{total}}\frac{dT}{dt} = -K_w(T - T_b) + P(t) \tag{2.22}$$

where C_{total} is the heat capacity of the sample platform and the sample, K_w is the thermal conductance of the wires connecting the platform to the thermal bath, T_b is the temperature of the thermal bath, $P(t)$ is the power supplied by the heater to the sample. The heat capacity of the sample can then be extracted by subtracting a background measurement (also known as an addenda measurement) of the platform and thermal grease used to hold the sample. The heat pulses are generally performed at numerous starting temperatures in order to measure the heat capacity as a function of temperature, as shown in Fig. 2.8b. It is possible for the fit to deviate significantly from the

[11] In the case that a sample's thermal coupling to the stage is weak, a different expression using two time constants can be used.

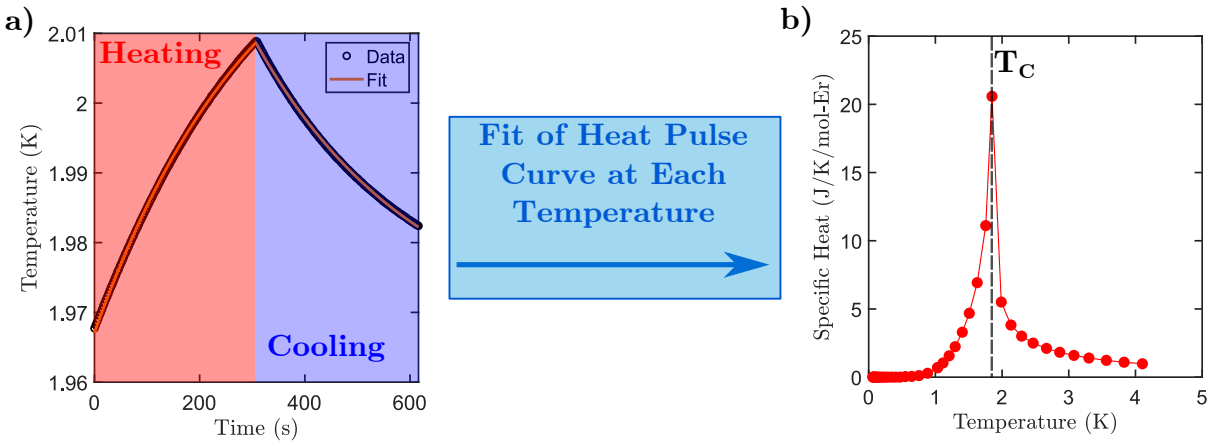

Figure 2.8: a) Characteristic heating and cooling curve for a measurement of the specific heat. The data measured after the heating is fit to extract the specific heat. b) Specific heat data showing a lambda-like peak at 1.9 K due to a magnetic ordering transition in the compound measured, D-$Er_2Si_2O_7$. Data reproduced from [34].

data, typically due to inadequate thermal conductivity between the sample platform and the sample. This is something that (generally) only happens at the lowest temperatures (> 100 mK) and will be addressed more in regards to specific heat data presented in Chapter 3. As can be seen from Fig. 2.8, the critical temperature for the magnetic ordering of the system can be measured. Additionally, if enough points are garnered in the vicinity of the critical temperature, the system can be fit to a critical exponent of the form $|T - T_c|^{\beta}$. The critical exponent, β, can then be compared to other systems or theoretical predictions to better understand the nature of the phase transition. This process is relatively straightforward and accessible, demonstrating the incredible power of heat capacity measurements.

In this work, only systems utilizing rare-earth ions were studied. Due to the highly localized nature of the $4f$ electrons, the exchange interactions are relatively small, often leading to transitions at very low temperatures (< 1.8 K) that traditional evaporative He cooling cannot access. To reach these ultracold temperatures, dilution cooling is utilized as it can reach temperatures down to roughly 0.07 K. Dilution cooling primarily works on the concept of the enthalpy of mixing. When a mixture of ^{3}He and ^{4}He is cooled to temperatures below approximately 0.9 K, phase separation occurs between a pure ^{3}He phase and a phase with 6.6% ^{3}He and 93.4% ^{4}He. The former is referred to as the concentrated phase and the latter is referred to as the dilute phase. In order to

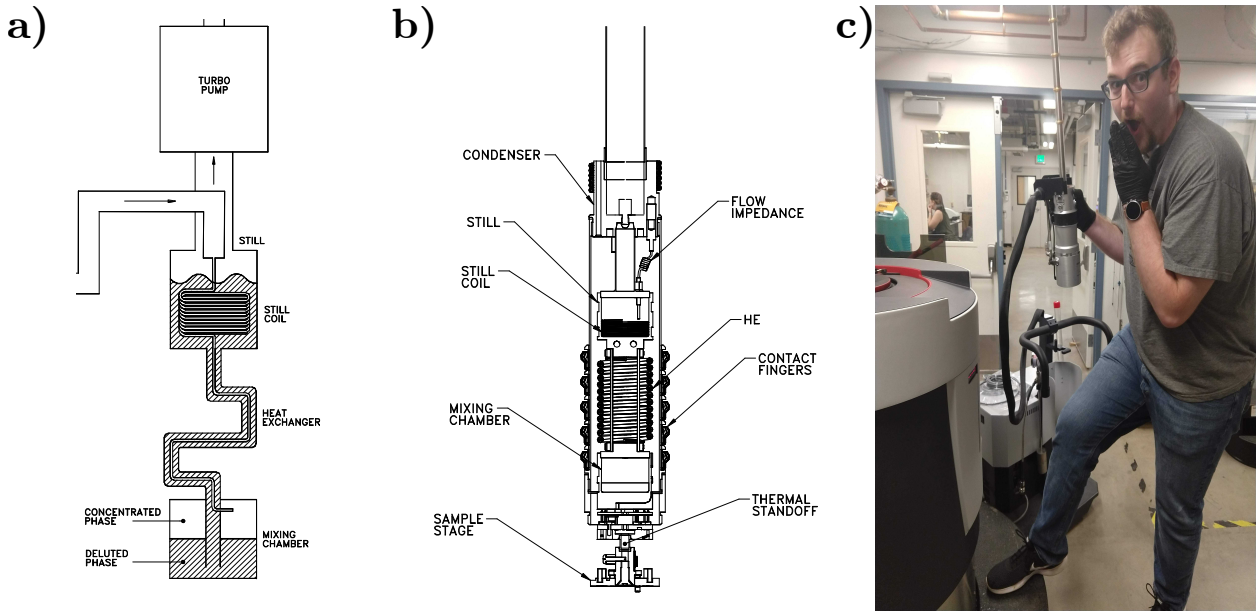

Figure 2.9: a) Diagramattic view of the Quantum Design PPMS Dilution Refrigerator insert showing the turbo pump, the still, the heat exchanger, and the mixing chamber. Diagram from [35]. b) Actual layout of the end of the dilution refrigerator, where the mixing and cooling takes place. The sample would be mounted at the stage at the bottom and cooled by the connection to the mixing chamber. Image from [35]. c) Scandalous photo of Gavin loading the dilution refrigerator probe at Colorado State University.

cool, ^{3}He needs to be removed from the dilute phase so the endothermic process of ^{3}He crossing from the concentrated phase to the dilute phase can occur. This is generally done by connecting a pumping tube from a still to the bottom of the mixing chamber (where the denser dilute phase resides). Osmotic pressure drives the ^{3}He atoms up the pumping tube into the still, which is kept at low pressure by use of a turbo pump and at a temperature of 0.7 K by a heater. This low pressure and temperature causes the ^{3}He to evaporate in the still, removing it from the dilute phase. The ^{3}He is then recondensed and put back into the concentrated phase of the mixing chamber, thus completing the cooling cycle. This method, as implemented by the Quantum Design PPMS Dilution Refrigerator insert is shown in Fig. 2.9.

2.2.3 Magnetometry

Magnetometry is an essential tool in the condensed matter physicist's toolbox. Magnetometry is used to measure the magnetic moment of a sample, generally measuring the moment with respect to a varied parameter, like temperature or magnetic field. In this work, a magnetometer with

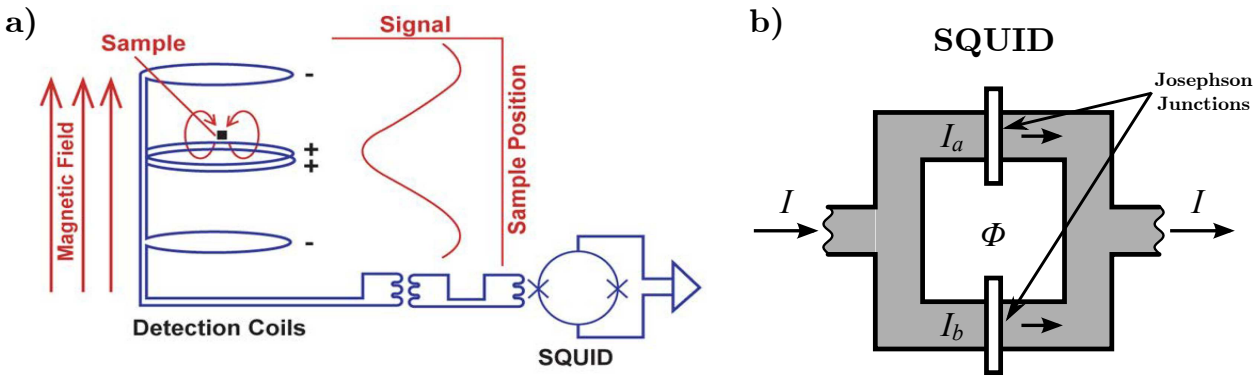

Figure 2.10: a) A diagram of basic parts of a SQUID magnetometer. Figure is from reference [36]. b) Diagram of a SQUID, showing the two Josephson junctions in parallel in a superconducting loop. Image credit: Miraceti - Own work, CC BY-SA 3.0, https://commons.wikimedia.org/w/index.php?curid=13302041

a Superconducting Quantum Interference Device (SQUID) was used. A SQUID magnetometer works by moving a sample through a set of detection coils that are inductively coupled to two Josephson junctions in parallel with one another [12]. When the sample is moved through the coil, a change in magnetic flux occurs in the coil and generates a current via Lenz's law. This current is then inductively transferred to the one of the Josephson junctions. This causes a change in flux in the Josephson junction and the Josephson junction then generates a current to maintain integer flux throughout the loop. The change in flux is incredibly sensitive to the magnetic field, allowing for measurement of magnetic moments on the order of 10^{-7} emu. A diagram of a SQUID magnetometer and the SQUID itself is shown in Fig. 2.10.

In this work, primarily direct current (DC) magnetometry measurements were utilized. Two different types of measurements were performed using DC magnetometry: magnetization and susceptibility measurements. The magnetization measurements measure the moment of the sample at various magnetic field strengths. This measurement allows for the identification of field-induced phase transitions and the saturated moment of the sample at high field. As primarily rare-earth systems were measured in this work, high field data must be considered carefully due to the possibility

[12] A Josephson junction is a device made up of two or more superconductors with a weak link between them, the link is typically made of an insulator or non-superconducting metal. These superconducting loops must have integer values of flux enclosed by the loop and therefore will create a current to increase/decrease the flux to maintain an integer value.

of populating higher crystal field levels at high magnetic field strengths. Susceptibility measurements are like magnetization measurements, but instead of varying magnetic field, the temperature is varied. Susceptibility data is analyzed as the ratio of the magnetization to the magnetic field strength, as it is a measure of how the material will become magnetized in an applied magnetic field. Susceptibility measurements are generally only performed at very low field strengths due to susceptibility only being defined in the limit of zero magnetic field, mathematically represented as,

$$\chi = \left.\frac{\partial M}{\partial H}\right|_{H=0} \tag{2.23}$$

where χ is the susceptibility, M is the magnetization of the sample, and H is the magnetic field. Susceptibility measurements are generally used to search for and characterize magnetic phase transitions. While specific heat measurements could determine the critical temperature of these phase transitions, specific heat measurements are not ideal for determining if a transition is magnetic and specific heat cannot determine if the transition is antiferromagnetic, ferromagnetic, etc. Additionally, information such as the magnetic moment per site or the strength of the magnetic interactions via Curie-Weiss fits can be extracted. This makes susceptibility and magnetization measurements excellent compliments to specific heat measurements and enable quick characterization of new magnetic materials. The susceptibility, magnetization, and specific heat measurements are vital for the neutron scattering experiments performed, as these measurements are often used to determine the experimental parameters and justification for a neutron scattering experiment.

Chapter 3

A Novel Strongly Spin-Orbit Coupled Quantum Dimer Magnet: $Yb_2Si_2O_7$

3.1 Context

This chapter consists of the paper *A Novel Strongly Spin-Orbit Coupled Quantum Dimer Magnet: $Yb_2Si_2O_7$* which was published in Physical Review Letters in 2019* [7]. The supplemental information for the paper and an unpublished erratum are shown in Appendix A and Appendix A.11, respectively. Additional data that has not appeared in press is shown in Section A.12. This work utilized elastic and inelastic neutron scattering, heat capacity, magnetometry, and ultrasound velocity measurements to determine that $Yb_2Si_2O_7$ has a quantum dimer magnet ground state with field-induced features reminiscent of those observed in traditional $3d$ transition metal BEC systems. In the erratum, I outline an issue our research group recently discovered that affects the heat capacity data presented in the paper. This erratum does not affect the fundamental conclusions of the paper and will be published when new data is available. Overall, the possible field induced BEC state in $Yb_2Si_2O_7$ opens many avenues for studying the effects of inherent anisotropy on well understood bosonic theories and serves as a centerpiece of this dissertation.

3.1.1 Contributions

H. S. Nair, T. Reeder, G. Sala, and K. A. Ross performed the inelastic neutron scattering measurements. G. Hester and K. A. Ross performed the subsequent analysis of the inelastic neutron scattering. G. Hester, D. R. Yahne, A. A. Aczel, and K. A. Ross performed and analyzed the elastic neutron scattering measurements. J. A. Quilliam, D. Ziat, L. Berges performed the ultrasound velocity and zero-field heat capacity measurements. Heat capacity measurements in a magnetic

field were primarily performed by G. Hester with assistance from D. R. Yahne, H. S. Nair, and K. A. Ross. The synthesis of $Yb_2Si_2O_7$ was primarily performed by H. S. Nair, T. Reeder, G. Hester, T. N. DeLazzer, J. R. Neilson, and K. A. Ross. The first draft of the paper was written by G. Hester and detailed editing was performed by G. Hester, J. A. Quilliam, and K. A. Ross.

3.2 Research Article

3.2.1 Overview

The quantum dimer magnet (QDM) is the canonical example of quantum magnetism. The QDM state consists of entangled nearest-neighbor spin dimers and often exhibits a field-induced triplon Bose-Einstein condensate (BEC) phase. We report on a new QDM in the strongly spin-orbit coupled, distorted honeycomb-lattice material $Yb_2Si_2O_7$. Our single crystal neutron scattering, specific heat, and ultrasound velocity measurements reveal a gapped singlet ground state at zero field with sharp, dispersive excitations. We find a field-induced magnetically ordered phase reminiscent of a BEC phase, with exceptionally low critical fields of $H_{c1} \sim 0.4$ T and $H_{c2} \sim 1.4$ T. Using inelastic neutron scattering in an applied magnetic field we observe a Goldstone mode (gapless to within δE = 0.037 meV) that persists throughout the entire field-induced magnetically ordered phase, suggestive of the spontaneous breaking of U(1) symmetry expected for a triplon BEC. However, in contrast to other well-known cases of this phase, the high-field ($\mu_0 H \geq 1.2$T) part of the phase diagram in $Yb_2Si_2O_7$ is interrupted by an unusual regime signaled by a change in the field dependence of the ultrasound velocity and magnetization, as well as the disappearance of a sharp anomaly in the specific heat. These measurements raise the question of how anisotropy in strongly spin-orbit coupled materials modifies the field induced phases of QDMs.

3.2.2 Introduction

Quantum dimer magnets (QDMs) represent the simplest cases of quantum magnetism, where entanglement is a required ingredient for even a qualitative understanding of the phase. In a QDM, entangled pairs of spins form $S_{tot} = 0$ dimers and result in a non-magnetic ground state. The

excited states of these entangled spins can be treated as bosons, called triplons, which can undergo Bose-Einstein condensation (BEC) as their density is tuned by an applied magnetic field. This BEC state is a magnetic field-induced long range ordered phase, which occupies a symmetric "dome" in the field vs. temperature phase diagram with two temperature-dependent critical fields, $H_{c1}(T)$ and $H_{c2}(T)$. The vast majority of the previously studied QDMs are based on 3d transition metal ions with "bare" (spin-only) $S = 1/2$ or $S = 1$ angular momentum, resulting in simple Heisenberg or XXZ spin interaction Hamiltonians, and high critical fields set by the relatively high energy scale of exchange interactions [19, 37, 38, 39, 40, 41].

Lanthanide-based magnetic materials with spin-orbit coupled pseudo-spin 1/2 (S_{eff} = 1/2) angular momenta can also exhibit quantum phases, and these are often directly analogous to their traditional $3d$ transition metal ion counterparts. However, entirely new phases are possible due to the anisotropic exchange in these materials [15, 16, 42, 43, 44, 45]. In the lanthanide series, Yb^{3+} has been of particular interest as it can generically host interactions leading to quantum fluctuations irrespective of the Crystal Electric Field (CEF) ground state doublet composition [8]. Indeed, various quantum phases have been discovered in Yb-based systems [9, 46, 47, 48, 49, 50]. Recently, a random valence bond state in $YbMgGaO_4$ was proposed [51]. However, a notable absence in the growing lineup of Yb quantum materials is a material exhibiting a QDM with a field induced BEC state. The opportunity to study such a material could lead to the observation of new phases describable by theories of interacting bosons, as well as new types of quantum phase transitions.

As a previously studied example, the metallic material $YbAl_3C_3$ was shown to host Yb dimerization and triplet excitations [52, 53]. However, an unusual field-induced ordered state was observed whose onset temperature far exceeds the spin gap energy [54], suggesting that it is not directly related to the singlet-triplet excitation (unlike a field-induced BEC phase). Additionally, $YbAl_3C_3$ shows field-induced *disordered* regimes that have yet to be fully understood, particularly in the context of the additional Kondo and RKKY interactions involving the conduction electrons in this material [55, 56, 57]. This material demonstrates that quantum dimerization is possible in lanthanide-based magnetic materials but does not always lead to a field-induced BEC phase.

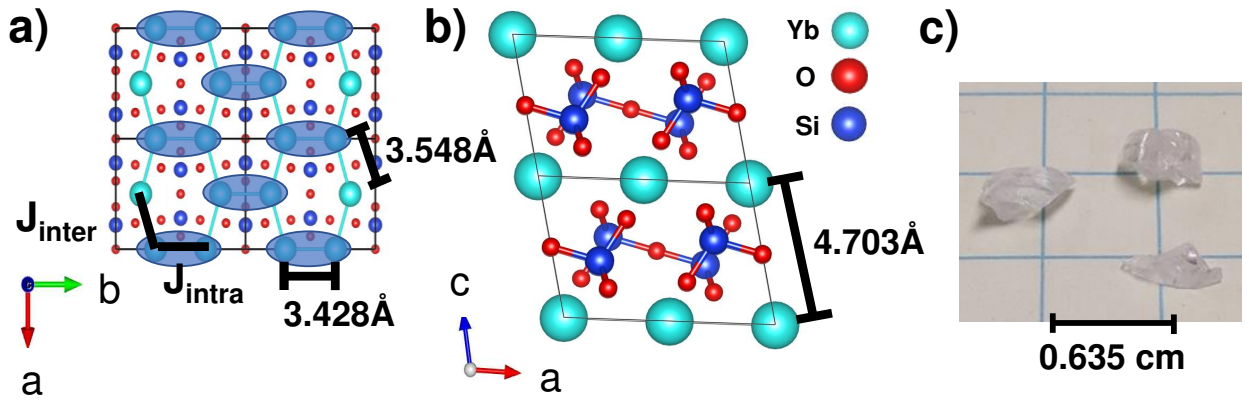

Figure 3.1: a) Crystal structure of $Yb_2Si_2O_7$ viewed along the c-axis, where Yb atoms are light green and form a distorted honeycomb lattice, Si atoms are blue, and O atoms are red [58]. Intradimer and interdimer bond lengths are shown (3% anisotropy), and J_{intra} and J_{inter} exchange tensors are labeled. The blue ovals indicate the probable location of the dimers. b) Crystal structure viewed along the b-axis, showing the separation of the layers of Yb honeycombs. c) Characteristic crystals obtained from breaking the crystal boule. The crystals are clear and colorless.

Naively, one might not expect a highly spin-orbit coupled material to exhibit BEC, which requires the exchange Hamiltonian to be at least U(1) symmetric (i.e., XXZ type interactions). Although recent work has demonstrated that for ideal, edge-sharing octahedral environments, Heisenberg exchange is indeed expected to dominate in Yb materials [8], such high exchange symmetry is not *a priori* expected for non-ideal local environments. However, a recent example of high exchange symmetry for Yb^{3+} in a non-ideal crystal field environment has been discovered in the Tomonaga-Luttinger liquid $YbAlO_3$ [9], suggesting that it may be more common than expected. Yet even with dominant Heisenberg interactions, smaller anisotropic terms should still be relevant which, in the case of a QDM, would be expected to modify the field-induced phases. Furthermore, Yb-based QDMs should provide a convenient testing ground for field-induced BEC physics due to reduced exchange energy compared to materials based on $3d$ transition metals. This leads to lower critical fields, which can be accessed by continuous field magnets, thus enabling experimental techniques such as inelastic neutron scattering (INS) to be brought to bear on the full phase diagram. This is the case for $Yb_2Si_2O_7$, as we show here.

3.2.3 Experimental Methods

$Yb_2Si_2O_7$ (monoclinic space group $C2/m$, room temperature lattice parameters of a = 6.7714(9) Å, b = 8.8394(2) Å, c =4.6896(5) Å, β = 101.984(9)° [59]) was previously studied in the context of polymorphism in the $RE_2Si_2O_7$ (rare earth pyrosilicate) series [17, 18], but its magnetic properties have not been reported. $Yb_2Si_2O_7$ has only one reported polymorph, known as the C-type pyrosilicate (Fig. 3.1). The single crystal samples of $Yb_2Si_2O_7$ used in this study were grown via the optical floating zone method [34, 59]. Our growths have resulted in clear, colorless multi-crystal boules which are then broken into smaller single crystal pieces as shown in Fig. 3.1c.

Magnetization was measured using a MPMS XL Quantum Design SQUID magnetometer at T = 1.8 K along the a^*, b, and c directions. Field and temperature-dependent specific heat was measured down to 50 mK using the quasi-adiabatic heat pulse method in a Quantum Design Dynacool PPMS with a dilution refrigerator insert at Colorado State University, as well as a home-built dilution refrigerator at Université de Sherbrooke. $Lu_2Si_2O_7$ was also measured as a non-magnetic analog. Ultrasound velocity experiments were performed down to 50 mK using a pulsed, time-of-flight interferometer. 30 MHz transducers were glued to parallel surfaces to propagate longitudinally polarized sound waves along the c^*-axis. The absolute velocity of the quasi-longitudinal mode studied here was approximately 3000 m/s and relative changes in velocity ($\Delta v/v$) were measured with high precision using a phase-lock loop. Powder neutron diffraction data was collected on BT1 at the NIST Center for Neutron Research with incident wavelength $\lambda = 2.0787$ Å and 60 arcminute collimation. Synchrotron x-ray diffraction (SXRD) data were recorded at $T = 295$ K at beamline 11 BM (λ = 0.41418 Å) at the Advanced Photon Source, Argonne National Laboratory. Time-of-flight INS experiments were performed at the Cold Neutron Chopper Spectrometer (CNCS) at the Spallation Neutron Source, Oak Ridge National Laboratory (ORNL). These INS data were collected using E_i = 1.55 meV neutrons in the "high flux" chopper setting mode, producing an energy resolution of δE = 0.037 meV at the elastic line [32], and were analyzed using the DAVE software package [60]. A neutron diffraction measurement using $E_i = 14.7$ meV neutrons

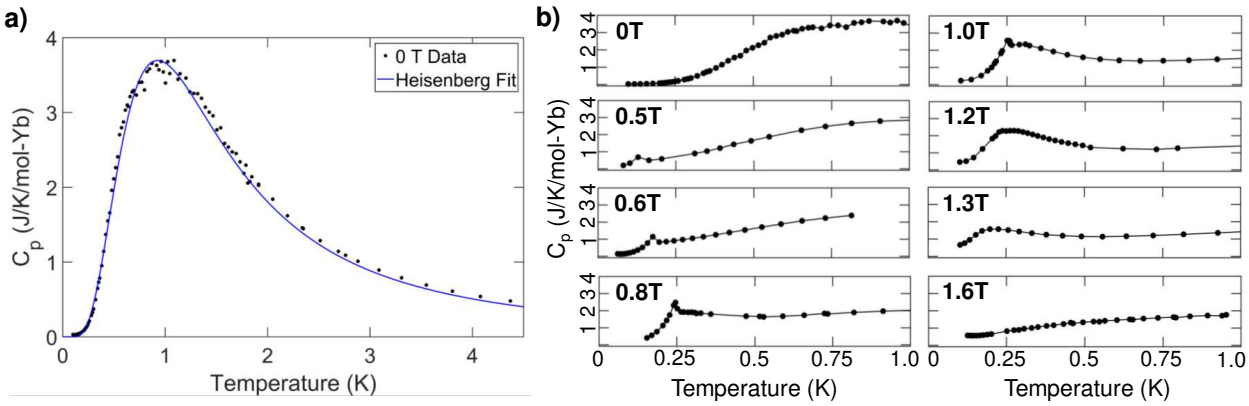

Figure 3.2: a) Zero-field specific heat and fit to a dispersive 4-level Schottky anomaly, using Heisenberg exchange for inter- and intra-dimer interactions (J_{intra} = 0.236(4) meV, J_{inter} = 0.06(2) meV). b) Specific heat of $Yb_2Si_2O_7$ at increasing fields with $H||c$. A sharp anomaly is visible at 0.5 T ($>H_{c1}$), which corresponds to a field-induced magnetically ordered state. The transition temperature maps out a dome as a function of field, but the sharp anomaly is replaced by a broad anomaly above $\sim$ 1.2 T (H_m), which moves to lower temperatures with increasing field. Above H_{c2}(1.4 T), the broad anomaly shifts to higher temperatures with increasing field, consistent with field polarized paramagnetism.

was performed using the Fixed-Incident Energy Triple-Axis Spectrometer (FIE-TAX) on the HB-1A beamline at the High Flux Isotope Reactor at Oak Ridge National Laboratory, using collimator settings of 40' - 40' - 40' - 80'.

Rietveld analysis of the SXRD data [59] confirms the previously reported crystal structure. Analysis of the zero field, high-temperature, magnetic specific heat of $Yb_2Si_2O_7$ confirms that a low energy S_{eff}=1/2 picture applies at temperatures well below $\sim$ 100 K [59]. The saturation magnetization at $T = 1.8$ K along three crystal directions gives the approximate g-values of $g_{a*} = 3.2$, $g_b = 2.0$, and $g_c = 4.8$.

3.2.4 Results

The zero-field specific heat shown in Fig. 3.2a displays a broad feature peaked at $\sim$ 1 K, which can be fit to a dispersive four level Schottky anomaly form, consistent with an interacting spin dimer ground state. We used an approximation of an interacting triplon model to fit the zero-field specific heat [59], enforcing Heisenberg interactions. The fit yielded the parameters J_{intra} = 0.236(4) meV and J_{inter} = 0.06(2) meV. These parameters are similar to those extracted from fit-

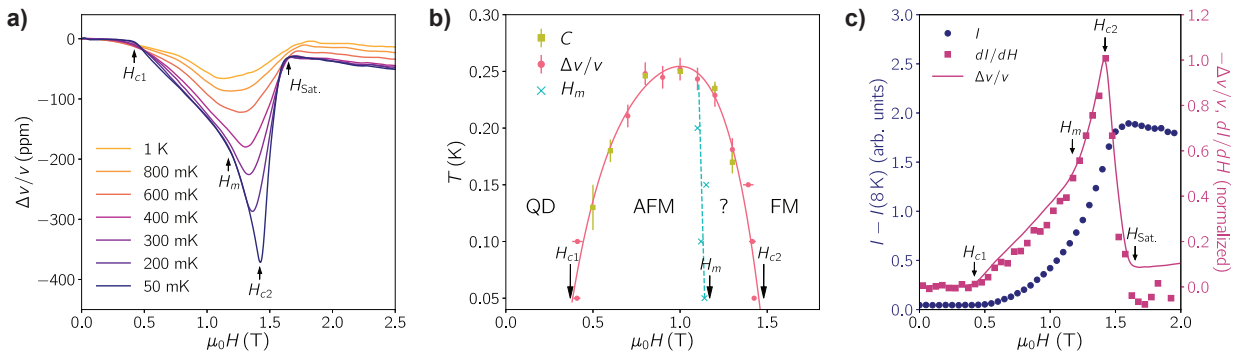

Figure 3.3: a) Ultrasound velocity with longitudinally polarized sound waves along the c^*-axis. b) H vs. T phase diagram for $Yb_2Si_2O_7$ with the points on the phase boundary determined by ultrasound velocity (pink circles and blue crosses) and specific heat (yellow squares). The field was applied along the c-axis (specific heat) and c^*-axis (ultrasound). c) Evolution of the (2,0,0) magnetic Bragg peak intensity (blue) versus field, $I(H)$, which is proportional to the square of the net magnetization. Additionally the derivative of the (2,0,0) magnetic Bragg peak intensity (square symbols) and the inverse of the ultrasound velocity data (solid line) are overlaid, showing agreement between these two measurements.

ting the field polarized spin wave spectrum; J_{intra} = 0.217(3) meV and J_{inter} = 0.089(1) meV [59]. The adequacy of Heisenberg interactions for reproducing both the zero field C_p and field-polarized INS data measurements suggests that $Yb_2Si_2O_7$ is another case in which Yb^{3+} interactions are unexpectedly predominantly isotropic. The entropy change through this low temperature Schottky anomaly (0.05 to 2 K), reaches the expected Rln2 per Yb [59], indicating that $Yb_2Si_2O_7$ does not undergo a magnetic ordering transition at lower temperatures, and thus remains quantum disordered down to $T = 0$ K. This is further confirmed by the lack of magnetic Bragg peaks at 50 mK, as determined by both single crystal (Fig. 3.3c) and powder neutron diffraction measurements [59].

The field-dependence ($H||c$) of the specific heat is shown in Fig. 3.2b. At $H = 0.5$ T, a sharp anomaly appears at $T = 0.13$ K, which we have confirmed by neutron scattering to coincide with a transition to long range magnetic order via the appearance of magnetic Bragg peaks. With increasing field, the transition temperature maps out a "dome" in the H vs. T phase diagram as expected for a BEC phase. As the field is increased further (0.8T), a broad feature emerges, which eventually becomes the dominant feature above $H_m = 1.2$ T. The maximum of this broad feature then continues to trace out the high field region of the dome, with the temperature of the maximum

decreasing with increasing field. At 1.6 T, the maximum of the broad feature is again increasing in temperature with increasing field as expected for a field-polarized paramagnetic regime.

Isothermal field scans of variations in sound velocity are shown in Fig. 3.3a for various temperatures. At the lowest temperatures ($T = 50$ mK) the sound velocity is largely field independent until $H_{c1} \simeq 0.4$ T, where $\Delta v/v$ begins decreasing with field. At $H_{c2} \simeq 1.4$ T, $\Delta v(H)$ reaches a minimum, before returning sharply to roughly the zero-field value in the field polarized limit. In addition to the two expected critical fields, H_{c1} and H_{c2}, the sound velocity also exhibits a significant change in slope at roughly $H_m = 1.2$ T, suggesting the presence of an additional phase, as indicated in Fig. 3.3b. Aside from the sharp change of slope at H_m, our sound velocity measurements resemble those performed on another quantum dimer magnet, $Sr_3Cr_2O_8$ [61]. In contrast, sound velocity measurements on $NiCl_2$-4SC$(NH_2)_2$ [62] show sharper dips at both H_{c1} and H_{c2}, which are attributed to coupling between the ultrasound velocity and antiferromagnetic fluctuations.

As the temperature is raised, the overall variations in sound velocity become much smaller in magnitude and the sharp features are smoothed out, hence we use temperature scans of sound velocity (see Supplemental Information [59]), which show small but fairly sharp anomalies, to establish the phase boundaries of the antiferromagnetic dome at higher temperatures. These boundaries are entirely consistent with the specific heat measurements.

The dome of field-induced order mapped out by the specific heat and ultrasound velocity data (Fig. 3.3b) is similar to the BEC phase of traditional QDMs, but there is an important difference: the dome in $Yb_2Si_2O_7$ is highly asymmetric, with an unusual regime in the high field part of the phase ($H > H_m$). Asymmetry of the dome can sometimes be attributed to quantum fluctuations in the proximity of H_{c1} which is expected when H_{c1}/(H_{c2}-H_{c1}) is small. However, in $Yb_2Si_2O_7$ this number is 0.4, which is twice as large as the well-known case of dome asymmetry in DTN [63]. Further, this effect does not explain the high field phase above H_m. This unusual regime may be due to non-U(1) symmetric terms in the S_{eff}=1/2 low energy effective Hamiltonian for $Yb_2Si_2O_7$. However, the strength of any anisotropic exchange is limited by our observation of a Goldstone-like mode (gapless to within $\delta E = 0.037$ meV) via INS, discussed below.

Fig. 3.3c shows the field dependence of neutron diffraction (measured on FIE-TAX) at the (2,0,0) zone center. This reflection is only sensitive to the square of the net magnetization (m_z^2) that arises due to canting towards the field direction rather than any AFM components of the magnetic structure. The onset of magnetic order and growth of the net magnetization is confirmed above H_{c1} through the observation of increasing magnetic Bragg peak intensity. The intensity of the (2,0,0) peak shows an approximately quadratic increase, with a sudden change in the second derivative occurring at approximately H_m. Additionally, Fig. 3.3c shows a comparison of the first derivative of the (2,0,0) Bragg peak intensity at 50 mK and the negative of the relative ultrasound velocity at 100 mK, which are consistent (though this level of agreement is somewhat unexpected following a standard theoretical treatment, see [59]).

INS data provides evidence of the spontaneous breaking of an approximately continuous symmetry for fields between H_{c1} and H_{c2}. Fig. 3.4 shows the INS spectra of $Yb_2Si_2O_7$ at $T = 50$ mK for representative applied fields along the c-axis. In a QDM with Heisenberg exchange, the three excited dimer states are triply degenerate (forming a triplet with $S_{tot} = 1$, and $S_z = -1, 0,$ and 1), and are then Zeeman split by the applied magnetic field. With finite interdimer exchange the resulting triplons are mobile, and the excited states become dispersive. For $Yb_2Si_2O_7$ below H_{c1} a resolution-limited single excited dispersive branch (bandwidth of 0.167(1) meV, and a gap of 0.1162(4) meV) is visible. The apparent secondary branch observed around $(\overline{0.1}, \overline{1}, 0)$ and ($\bar{1}$,$\bar{1}$,0) is due to a minority crystal grain. The energy of the observed excitation does not change for $H < H_{c1}$ as shown in the supplemental information [59], signifying that the angular momentum projection along the magnetic field is zero (i.e., S_{tot} = 1, S_z = 0, which we call $\psi_{1,0}$). The absence of apparent $S_{tot} = 1$, $S_z \pm 1$ modes (hereafter labeled as $\psi_{1,\pm1}$) at most field strengths below H_{c1} indicates that the neutron scattering transition matrix elements from the ground state to $\psi_{1,\pm1}$ are small compared to that for $\psi_{1,0}$. However, $\psi_{1,\pm1}$ are discernible with very weak intensity at fields near H_{c1} indicating the transition matrix elements are non-zero [59]. Above H_{c1}, a new low energy excitation appears, which is gapless at the magnetic zone centers to within the energy resolution of the instrument ($\delta E = 0.037$ meV). This Goldstone mode implies spontaneous breaking of an ap-

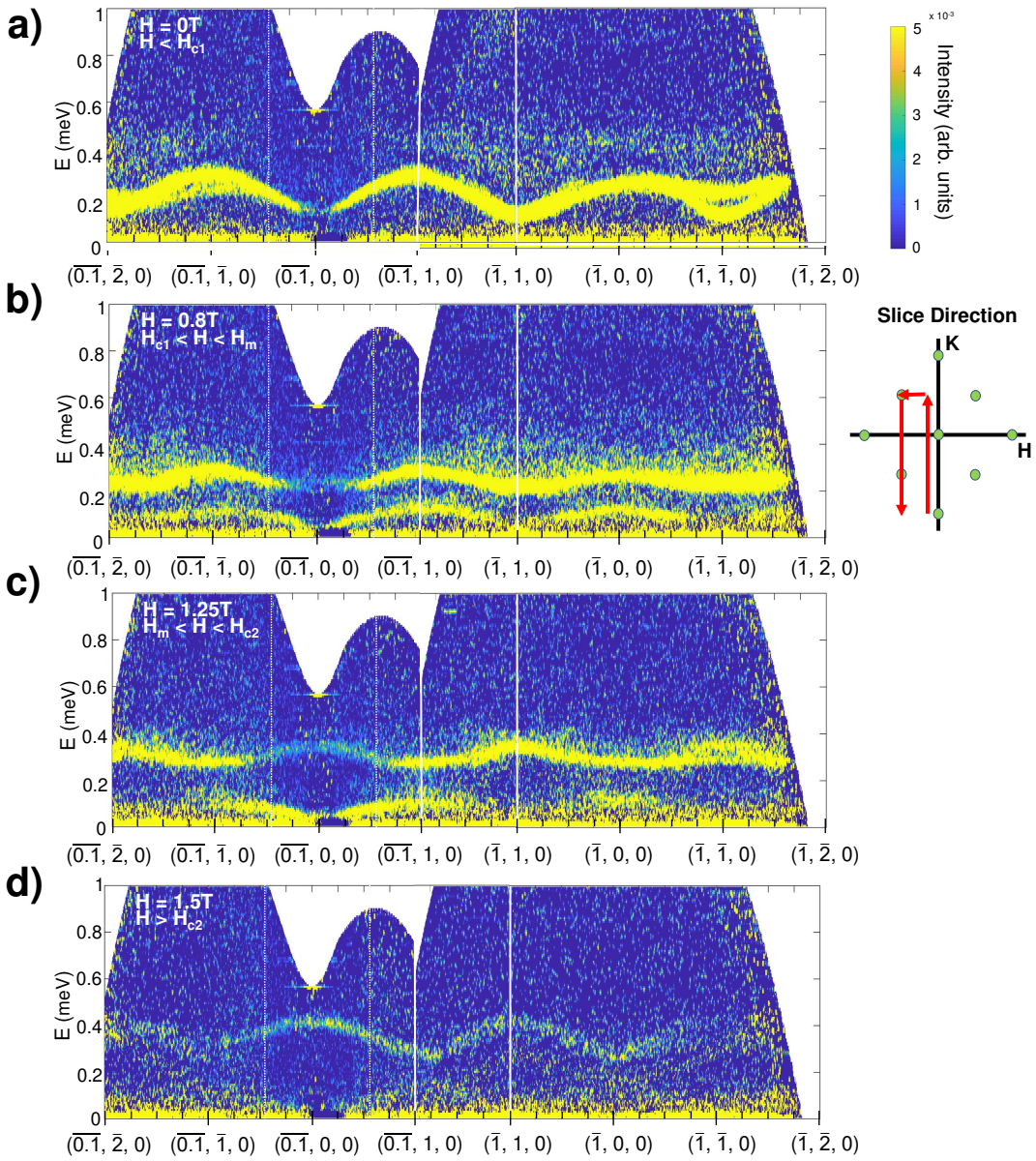

Figure 3.4: INS data at $T = 50$ mK for four representative field strengths ($H||c$). The path shown includes the reciprocal lattice directions [-0.1K0], [H10], and [-1K0] as shown schematically to the right of the figure. All slices shown are integrated $\pm$ 0.1 r.l.u. in the perpendicular direction. At zero field (panel a), two bands are visible near (-1,1,0) and (-0.1, -1, 0) due to a misaligned grain in the sample [59]. These are actually due to the same excitation which is identified as the $\psi_{1,0}$ state. Between H_{c1} and H_{c2} (panels b and c), a Goldstone mode appears which is gapless at zone centers to within the energy resolution of the instrument, δE = 0.037 meV. Above H_{c2} (panel d) the intensity of the excitation drops dramatically due to the system entering a field-polarized paramagnet state.

proximate U(1) symmetry in the plane perpendicular to the applied magnetic field (the a^*-b plane), suggestive of the BEC transition observed in traditional QDMs [19, 64]. Additionally we note

that the energy resolution is $\sim$16% of our estimated J_{intra}, thus this measurement of the Goldstone mode actually allows for a potentially sizable anisotropic exchange contribution. Furthermore, the presence of a distinguishable region of the field-induced phase (between H_m and H_{c2}) is not expected for simple Heisenberg or XXZ exchange. We find that in this field region the Goldstone mode persists, despite the lack of evidence for spontaneous symmetry breaking in $C_p(T)$ (i.e. a sharp anomaly is absent). However, the broad $C_p(T)$ feature does move to lower temperature as the field is further increased in this field region, tracing out the high-field side of the dome phase boundary. Above H_{c2} all the excitations become fully gapped and the broad feature in C_p moves to higher temperature with increasing field, consistent with a field-polarized paramagnet. In the field polarized regime, the inelastic intensity is greatly reduced due to the development of strong magnetic Bragg peaks at the elastic line, as expected based on the sum rule for magnetic neutron scattering.

3.2.5 Discussion

Recently, rare-earth materials have been identified as potential hosts of Kitaev exchange in honeycomb materials [65]. In light of this, it is important to note that $Yb_2Si_2O_7$ is structurally similar to the famous Kitaev material Na_2IrO_3 [66], as they share the same space group and Wyckoff position of the magnetic species. Therefore, Kitaev exchange is allowed by symmetry in $Yb_2Si_2O_7$. If Kitaev exchange were dominant in $Yb_2Si_2O_7$ it could lead to a quantum spin liquid ground state [15]. Interestingly, the presence of a Goldstone mode does *not* rule out such anisotropic Kitaev exchange due to the "hidden" SU(2) symmetries found within the extended Kitaev-Heisenberg model [67, 68]. However, our fits to field polarized INS data are well-approximated by Heisenberg interactions, so Kitaev interactions are unlikely to be dominant in this material.

In summary, the strongly spin-orbit coupled material $Yb_2Si_2O_7$ realizes a QDM ground state with magnetic field-induced order reminiscent of a BEC phase. However, this ordered phase exhibits unusual characteristics at the high field part of the dome, including an abrupt change in the field dependence of the magnetization and sound velocity, and the loss of a sharp anomaly in the

specific heat. The presence of a Goldstone mode throughout the full field-induced ordered state suggests dominant Heisenberg or XXZ exchange interactions, and the former is confirmed by fits to field polarized INS data and the zero-field specific heat. However, the observation of the unusual regime between H_m and H_{c2} may imply that additional anisotropic interactions are necessary to fully describe the field induced phases of this novel quantum magnet. $Yb_2Si_2O_7$ provides the first example of a Yb^{3+}-based QDM with a possible field-induced BEC phase, adding this canonical example of quantum magnetism to the roster of quantum phases exhibited by materials based on this versatile ion.

Chapter 4

Magnetic properties of the Ising-like rare-earth pyrosilicate: D-$Er_2Si_2O_7$

4.1 Context

This chapter consists of my unpublished work, which is being prepared as a manuscript with the working title *Magnetic properties of the Ising-like rare-earth pyrosilicate: D-$Er_2Si_2O_7$*, where we studied magnetic ground state and field-induced properties of D-$Er_2Si_2O_7$. A preprint version of the paper is available on arXiv under reference [69].

This paper originally appeared on arXiv under the title *Evidence for a field-induced quantum phase transition in Ising-like D-$Er_2Si_2O_7$*, however, it was later realized that the crystal used for some of the AC susceptibility data included was not aligned as intended which invalidated our initial comparision to the TFIM. This discrepancy is mentioned in the main text and outlined further in the supplemental information (Appendix B). In this work, we utilized powder inelastic neutron scattering, powder neutron diffraction, single crystal AC susceptibility, and heat capacity measurements to study the Ising-like nature of D-$Er_2Si_2O_7$. While this is currently a work in progress, our work shows that D-$Er_2Si_2O_7$ exhibits a gapped zero-field spectra - consistent with predominantly Ising-like exchange - and our transverse field AC susceptibility measurements hint at the possibility of D-$Er_2Si_2O_7$ being a new candidate for the TFIM.

4.1.1 Contributions

C. L. Sarkis, D. R. Yahne, J. A. R. Rivera, and K. A. Ross performed the powder inelastic neutron scattering and the data was primarily analyzed by G. Hester, T. N. DeLazzer, and K. A. Ross. G. Hester, S. Calder, and K. A. Ross performed the neutron diffraction measurements and the neutron diffraction data was primarily analyzed by G. Hester with the assistance of D. R. Yahne and K. A. Ross. G. Hester, H. D. Zhao, T. N. DeLazzer, and K. A. Ross performed the

AC susceptibility measurements and they were primarily analyzed by G. Hester and K. A. Ross. Heat capacity measurements were performed by G. Hester with the assistance of D. R. Yahne, T. N. DeLazzer, and K. A. Ross. The first draft of the paper was written by G. Hester and detailed editing was performed by G. Hester and K. A. Ross.

4.2 Research Article

4.2.1 Overview

Ising-like spin-1/2 magnetic materials are of interest for their ready connection to theory, particularly in the context of quantum critical behavior. In this work we report detailed studies of the magnetic properties of a member of the rare-earth pyrosilicate family, D-$Er_2Si_2O_7$, which is known to display a highly anisotropic Ising-like g-tensor and effective spin 1/2 magnetic moments. We used powder neutron diffraction, powder inelastic neutron spectroscopy (INS), and single crystal AC susceptibility to characterize its magnetic properties. Neutron diffraction enabled us to determine the magnetic structure below the known transition temperature ($T_N = 1.9$ K) in zero field, confirming that magnetic state is a four-sublattice antiferromagnetic structure with two non-collinear Ising axes, as was previously hypothesized. Our powder INS data revealed a gapped excitation at zero field, consistent with anisotropic (possibly Ising) exchange. An applied field of 1 T produces a mode softening, which is consistent with a field-induced 2nd order phase transition. To assess the relevance of D-$Er_2Si_2O_7$ to the transverse field Ising model, we performed AC susceptibility measurements on a single crystal with the magnetic field oriented in the direction transverse to the Ising axes. This revealed a transition at 2.65 T at 0.1 K, a field significantly higher than the mode-softening field observed by powder INS, showing that the field-induced phase transitions are highly field-direction dependent as expected. These measurements suggest that D-$Er_2Si_2O_7$ may be a candidate for further exploration related to the transverse field Ising model.l.

4.2.2 Introduction

The identification of Ising-like magnetic materials has been historically important for verifying the many intriguing features of the classical Ising model [70, 71]. In the context of quantum magnetism, examples of Ising materials which can be tuned to a quantum phase transition (QPT) via a transverse magnetic field are in even higher demand. The Transverse Field Ising Model (TFIM) is one of the most tractable models with a QPT, and thus has been studied extensively theoretically, including in the burgeoning field of non-equilibrium quantum dynamics [72]. However, despite the seemingly straightforward ingredients, there are only a few currently known magnetic materials which approximate the TFIM; $CoNb_2O_6$ (quasi-1D) [24], (Ba/Sr)$Co_2V_2O_8$ (quasi-1D) [73, 74], and $LiHoF_4$ (dipolar coupled 3D) [75, 76]. With each of these materials, many detailed comparisons to theoretical expectations have been pursued, and even their non-equilibrium behavior are now being explored [77]. Yet, each material has its own deviations from the ideal models, and the identification of additional TFIM materials, particularly those representing the higher dimensional 2D or 3D (non-dipolar) models, which cannot be solved exactly, are of great interest. The first step in finding new TFIM materials is to find materials with predominantly Ising-like exchange. This type of anisotropic exchange is expected to be more prevalent in $4f$ rare-earth based magnetic systems, as the high spin-orbit coupling provides inherent anisotropy to the system.

Indeed, rare-earth based materials have become the subject of increased study in the realm of quantum magnetism in general. Due to the chemical similarity of the rare earths, the same structure can often be stabilized with a variety of rare-earth ions. However, the magnetic interactions and anisotropies can be dramatically different between each instance; such is the case for the rare-earth pyrochlores [78, 79] and the rare-earth delafossites [80, 81, 82, 83]. In this work we have investigated a member of the rare-earth pyrosilicate ($RE_2Si_2O_7$) family of compounds which have become the subject of renewed interested due to the discovery of a dimer magnet with evidence for a field-induced Bose-Einstein condensate in $Yb_2Si_2O_7$ [7, 84]. The present work focusses on the magnetic properties of one polymorph of $Er_2Si_2O_7$. It is worth noting that all of the lanthanide series can be synthesized in this stoichiometry (albeit with many possible structures) making this

series an interesting playground for understanding the interplay of magnetic species and crystal structure on the ground state of quantum magnets.

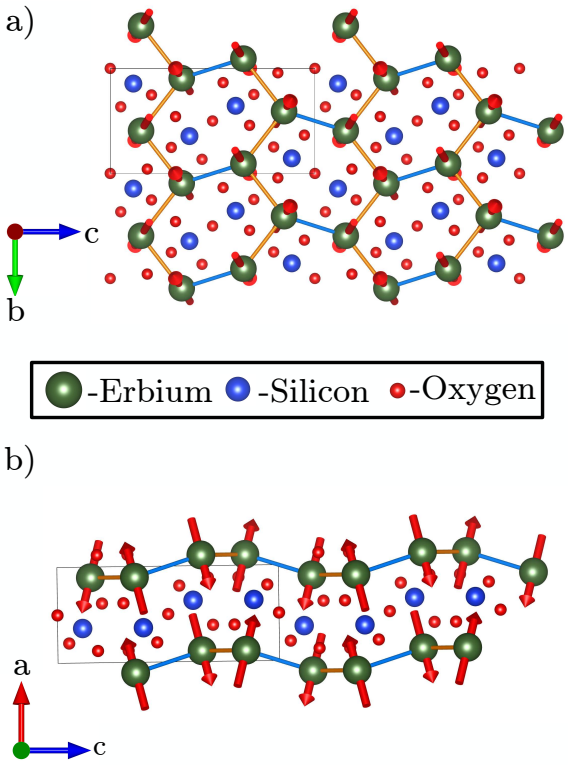

Figure 4.1: a) The crystal and magnetic structure (obtained from the refinement in Fig. 4.3a) of D-$Er_2Si_2O_7$ viewed along the a-axis. Bonds in orange dictate the equivalent "intrachain" interactions that form chains and bonds in blue dictate the interchain interactions that form a tessellated, distorted honeycomb lattice. Here Er atoms are green, Si are blue, and O are red. b) View of the crystal and magnetic structure along the b-axis showing the layered nature of the magnetic ions. All panels of this figure were created using the Vesta software [58].

The pyrosilicate compound $Er_2Si_2O_7$ can crystallize in three different structures based on the synthesis temperature: the low-temperature phase P1 (Type B), the intermediate-temperature phase C2/m (Type C) and the high-temperature phase $P2_1/a$ (Type D) [17, 18]. The focus of this work is the high temperature phase (shown in Fig. 4.1), hereby referred to as D-$Er_2Si_2O_7$. Since Er^{3+} is a Kramer's ion the ground state of the CEF is protected by time-reversal symmetry and thus must be at least doubly degenerate. In the 1970's the structure of the rare-earth pyrosilicates was determined due to interest in the magnetic, electrical, and optical properties of rare-earth materials.

In particular, the rare-earth pyrosilicates were of interest due to the 180° Si-O-Si bond in the $[Si_2O_7]^{6-}$ groups [17, 18]. After some time the magnetic properties of D-$Er_2Si_2O_7$ were explored via Zeeman spectroscopy and magnetometry [2, 85]. The Zeeman spectroscopy measurements revealed crystal field levels at 27 cm^{-1} (39 K) and 52 cm^{-1} (74 K), the former of which we have confirmed via specific heat in Appendix B.1. Further, Leask *et al.* determined an Ising-like g-tensor anisotropy, with $g_x = 2.6$, $g_y = 3.4$, and $g_z = 13.4$ [2]. The crystal symmetry results in two orientations of these local axes, with the x axis shared by both. The z axis was found to be 28° (clockwise) from the a axis and ± 15° from the a-b plane, while x is in the a-b plane (see Fig. 4.2c). However, there is a discrepancy in the g-tensor values identified by Leask, *et al.* [2] and those identified earlier by Maqsood [85]. This discrepancy could be due to Maqsood using Curie-Weiss fits to determine the values of the g-tensor. Curie-Weiss fits can prove unreliable for rare-earth ions due to crystal field effects; typically, they are performed at high temperatures to ensure the system is no longer strongly correlated, but for rare-earth ions this causes thermal population of higher crystal field levels and means the fit is not truly indicative of the low temperature angular momentum degrees of freedom. Previous temperature-dependent susceptibility measurements on single crystals of D-$Er_2Si_2O_7$ were performed along the c axis, a axis, and the m axis, where m refers to a vector in the a-b plane that lies 28° (clockwise) from the a axis, which we will refer to as the "average Ising direction" (the projection of Leask's z axis onto the a-b plane). The susceptibility along all three directions showed a sharp downturn indicative of antiferromagnetic ordering at 1.9 K, with the maximum susceptibility observed for measurements along m. This magnetic ordering temperature was corroborated by our group using zero-field specific heat measurements [34]. Magnetization versus magnetic field measurements along a and m showed evidence of a spin-flip transition at $\frac{1}{3}$ the saturation magnetization. This occurs at $\sim$ 0.5 T for the a axis and slightly lower for the m axis. The observation of a spin-flip transition is consistent with the Ising-like moment found from the g-tensor. After these seminal studies of D-$Er_2Si_2O_7$, no magnetic measurements were performed until the present study.

4.2.3 Experimental Methods

Details of the D-$Er_2Si_2O_7$ sample synthesis have been outlined elsewhere [34], but broadly the synthesis was performed by mixing stoichiometric amounts of Er_2O_3 and SiO_2, pressing the powder into dense rods, and heating the rods between 1400°C and 1500°C four times with intermediate re-grinding. Two types of samples were used in the present study. For susceptibility measurements, a small single crystal of pure D-$Er_2Si_2O_7$ - grown via the optical floating zone technique - was used. The second sample was a powder, which was used for neutron scattering and heat capacity. Rietveld refinement of room-temperature powder x-ray diffraction data indicated that Er_2SiO_5, a common (and stubborn) impurity in the synthesis of D-$Er_2Si_2O_7$, made up approximately 9% of the sample. The powder x-ray diffraction data for D-$Er_2Si_2O_7$ yielded the lattice parameters: a = 4.68878(8) Å, b = 5.56029(7) Å, c = 10.79659(10) Å, α = 90°, β = 90°, γ = 96.043(1)°. These parameters are consistent with previously published values [18]. Heat capacity measurements were performed using a Quantum Design PPMS with the heat capacity option on a sintered powder sample of D-$Er_2Si_2O_7$. AC susceptibility measurements were performed on a single crystal of D-$Er_2Si_2O_7$ (as confirmed by Laue x-ray diffraction) using a Quantum Design PPMS with the dilution refrigerator and AC susceptometer. These measurements were performed at numerous temperatures with f = 1000 Hz, H_{AC} = 0.2 mT, and with the DC magnetic field applied transverse to the "average Ising direction" (x in Fig. 4.2.

Inelastic neutron scattering (INS) measurements were performed on approximately 5 grams of powder loaded in a Cu canister at the NIST Center for Neutron Research in Gaithersburg, MD, USA using the Multi-Axis Crystal Spectrometer (MACS) [86] with a fixed final energy (E_f) of 2.5 meV, the double focusing monochromator, and Be filters on the incident and scattered beams. Neutron diffraction measurements were performed on the same sample at the High Flux Isotope Reactor at Oak Ridge National Laboratory using the HB-2A (POWDER) diffractometer [87]. The HB-2A data was collected at 10 K, 2 K, and 0.280 K with the Ge(113) monochromator ($\lambda = 2.41$ Å) and a collimation of open-21'-12'. All errorbars shown in this work indicate $\pm$ one standard deviation.

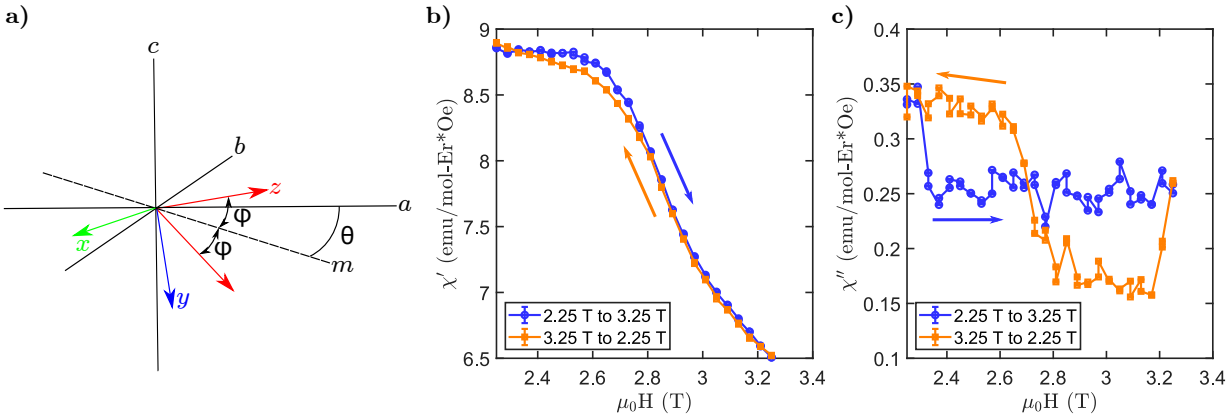

Figure 4.2: a) Schematic diagram showing the average Ising direction "m" and the two local Ising axes. The x-axis is transverse to both Ising axes. Only one of the two y-axes is shown for clarity. Here θ is the angle from the crystallographic a-axis and ϕ is the angle from the a-b plane. Leask *et al.* [2] previously found the single-ion g-tensor to be oriented towards θ = 28° and ϕ = 15°. In contrast, we found based on neutron diffraction data that the *ordered* the moments lie at θ = 21.3° and ϕ = 12.8°. For our transverse-field measurements, we chose to align the crystal perpendicular to the *ordered* moment. b-c) The real (χ') and imaginary (χ'') components of the AC susceptibility at $T = 0.1$ K, $f = 1000$ Hz, and $h_{ac} = 2$mT for a field ramp from 2.25 T to 3.25 T (blue circle) and a field ramp from 3.25 T to 2.25 T (orange square). A transition is observed at ∼2.65 T, which shows "hysteresis" in both the real and imaginary components of the susceptibility. It is unclear if this hysteresis is an experimental artifact and this is discussed further in the main text.

4.2.4 Results and Discussion

AC Susceptibility

AC susceptibility measurement results (at T = 0.1 K) with a field in the transverse direction (i.e. with AC and DC fields applied along x) are shown in Fig. 4.2b-c). The directions of the Ising axes (z) and transverse direction (x) in relation to the crystallographic axes is shown in Fig. 4.2a. We note that the magnetization along this transverse field direction of D-$Er_2Si_2O_7$ has not been previously studied. For the AC susceptibility measurements, we aligned the sample so that the field was applied along x, defined by the angles θ = 21.3° (the angle from the a-axis) and ϕ = 12.8° (the angle from the a-b plane) as determined by our neutron diffraction measurements discussed in section 4.2.4. The decision to use the moment direction found via neutron diffraction for the Ising direction - as opposed to the direction found by Leask *et. al* [2] - was based on the expectation that the ordered moment direction being determined in part by the *exchange* tensor, rather than solely the single-ion g-tensor. A common misconception about the TFIM is that it requires Ising-

like single ion anisotropy (e.g. $g_{zz} \gg g_{xx}, g_{yy}$), but in reality it is only required that the exchange anisotropy be Ising-like. In a low symmetry local environment like the Er^{3+} site in D-$Er_2Si_2O_7$, the two Ising axes do not have to be in the same direction. Hence, we feel that the ordered moment direction is a more appropriate representation of the relevant Ising axis.

The real (χ') and imaginary (χ'') components of the transverse-field susceptibility both show a transition at 2.65 T. A comparison of the measurements for increasing and decreasing field shows something similar to hysteresis, which would indicate a first order transition. However, the hysteresis does not behave as expected for first-order phase transitions - namely, the transition appears to occur at a *lower* field when the field is increased compared to when it is decreased, which is not expected for first order transitions, which are based on a nucleation and growth mechanism. Thus, it is currently unclear as to if this hysteresis is an experimental artifact or if it is intrinsic to the sample. Additional measurements at different temperatures and for wider magnetic field ranges are shown in Section B.3.1.

In a previous preprint version of this manuscript [69], a different set of AC susceptibility measurements was presented, which we later determined were obtained with the field not correctly oriented to the transverse (x) axis. This was shown via a subsequent set of DC magnetization measurements on the same crystal which showed a higher saturation magnetization than expected for that direction. This misorientation was confirmed by Laue x-ray diffraction to be 37° away from the transverse axis, approximately lying along the $(4\bar{9}1)$ direction. In the event that these measurements may still be useful to others, we have provided these DC magnetometry and AC susceptibility measurements in the Appendix (Section B.3.1).

Neutron Powder Diffraction

Neutron powder diffraction (NPD) data obtained at HB-2A was refined using the FullProf software [88] and the SARAh suite (using the Kovalev tables) [89, 90]. Peaks corresponding to D-$Er_2Si_2O_7$ and Cu (from the sample can) were observed at 10 K and 2 K (both are above T_N), but no sign of the impurity (Er_2SiO_5) was observed at these temperatures. This is likely due to the strongest nuclear peaks of Er_2SiO_5 occurring at positions obscured by nuclear peaks

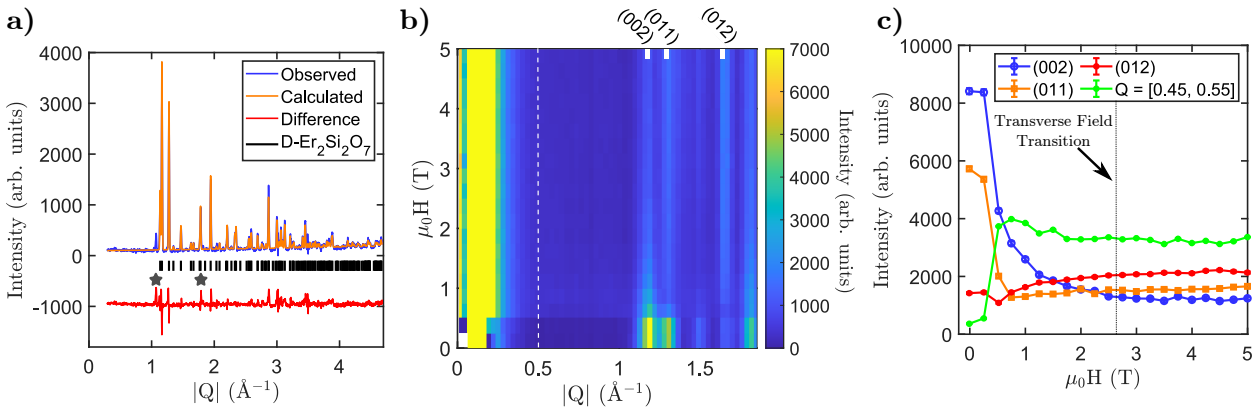

Figure 4.3: a) A Rietveld refinement of the magnetic structure of D-$Er_2Si_2O_7$. The observed intensities shown are after subtraction of 10 K data from 0.280 K data, and therefore are only due to magnetic order. Two impurity peaks are observed at 1.074 $Å^{-1}$ and at 1.819 $Å^{-1}$ - denoted by black stars - that correspond to the (110) and (310) reflections of Er_2SiO_5 (space group C2/c). These peaks are the only peaks not accounted for by the magnetic structure of D-$Er_2Si_2O_7$. b) Field versus momentum transfer (Q) elastic scattering (E $\in$ [-0.05,0.05] meV) data obtained on MACS (T_{avg} = 0.16 K) showing the evolution of Bragg peak intensities. White rectangles are shown to denote the Bragg reflections used for cuts in panel c. The white dashed line shows the location of the fourth cut in panel c. c) Evolution of the elastic intensity with field for (002), (011), (012), and Q = [0,45, 0.55] $Å^{-1}$. The Q = [0.45, 0.55] $Å^{-1}$ data is scaled by a factor of 10 for clarity. Data at 0 T, 3 T, and 5 T were obtained on the initial increase of the field after cooling from high temperature. All other field points were collected after the field had been increased to 8 T and returned to 0 T.

of D-$Er_2Si_2O_7$. A Rietveld analysis (Appendix B.2) of powder neutron diffraction data obtained at 10 K was also performed. The powder diffraction data at 2 K (Appendix B.2) shows diffuse scattering, as expected for a system approaching a continuous phase transition. Data at 0.280 K (below T_N) show an increase in intensity on peaks corresponding to the D-$Er_2Si_2O_7$ nuclear structure, aside from two peaks at 1.074 $Å^{-1}$ and 1.819 $Å^{-1}$ which can be indexed to the (110) and (310) positions of the impurity phase, Er_2SiO_5 (space group C2/c, a = 14.366(2) Å, b = 6.6976(6) Å, c = 10.3633(16) Å, α = 90°, β = 122.219(10)°, γ = 90°)[91]. The magnetism of Er_2SiO_5 has not previously been reported. Thus, we note in passing that since no magnetic impurity peaks were observed at 10 K or 2 K, the magnetic transition in Er_2SiO_5 is likely between 0.280 K and 2 K, to a $|\boldsymbol{k}| = 0$ ordered state. Fig. 4.3a shows the results of a Rietveld refinement on the magnetic structure of D-$Er_2Si_2O_7$. The data used for the refinement was a subtraction of the 10 K data from the 0.280 K data. A symmetry analysis of the allowed $|\boldsymbol{k}| = 0$ magnetic structures provides four irreducible representations. An attempt to fit each irreducible representation was made, with the

Γ_4 representation providing the best fit. The Γ_4 irreducible representation consists of three basis vectors; ψ_{10}, ψ_{11}, and ψ_{12} (see Section B.2 for the basis vector compositions). The coefficients for each basis vector are; C_{10} = 5.72(3), C_{11} = -2.34(6), and C_{12} = -1.45(6). These coefficients yield the magnetic structure shown in Fig. 4.1. This structure has the magnetic space group of $P2_1'/c$. Leask *et. al.* found the g-tensor axes to lie along θ = 28° (the angle from the a-axis) and ϕ = 15° (the angle from the a-b plane), whereas, we have found the moments to lie at θ = 21.3° and ϕ = 12.8°. This indicates that the ordered moments deduced from our refinement lie 6.9(5)° away from the single-ion Ising direction determined by Leask *et. al.* However, the overall ordered moment is similar. We measured an ordered moment of 6.56(3) μ_B at 250 mK and the moment found by Leask was 6.7 μ_B at 4.2 K. The discrepancy in the Ising axis direction is potentially due to the presence of the (unaccounted for, but small) Er_2SiO_5 impurity in our magnetic NPD data. Alternatively, it could be due to a difference in the exchange anisotropy directions compared to the single-ion anisotropy directions. The direction of the ordered moment direction would be influenced by both types of anisotropies. The details of the interactions in D-$Er_2Si_2O_7$ require further study, ideally by INS on single crystal samples.

Field-dependent Elastic Neutron Scattering

Elastic neutron scattering data measured using MACS, using the same powder sample as used at HB-2A, is shown in Fig. 4.3b and Fig. 4.3c. An "empty can" background was subtracted. Fig. 4.3b shows the field evolution of the elastic scattering at at an average temperature (T_{avg}) = 0.16 K. Magnetic Bragg peaks from the impurity (Er_2SiO_5) are not resolved, due to the coarser Q-resolution of MACS compared to HB-2A. Intensity versus field cuts for the (002), (011), and (012) reflections are shown in Fig. 4.3c. The intensity of the peaks does not change significantly between 0 T and 0.25 T, even though the 0.25 T data was measured after going to high field (see caption to Fig. 4.3 for more detail). Dramatic changes in magnetic peak intensities are observed between 0.25 T and 2 T. Since the experiment was performed on a powder sample, all field directions are averaged here, including the field perpendicular to the Ising direction, which we have shown induces a transition at 2.65 T (Fig. 4.2). Other field directions are already known to induce

transitions in the field range of about 0.5 T [2]. Overall, the dramatic changes in Bragg intensity all occur below about 1 T. Above 1 T, the intensity of the peaks gradually changes, likely due the Er^{3+} moments approaching saturation along the field direction, as much as would be allowed by the Ising axes. An interesting effect is observed away from the Bragg peaks, shown in Fig. 4.3c as a cut at Q = 0.5 $Å^{-1}$(integrated from 0.45 to 0.55 $Å^{-1}$). The incoherent background appears to increase in intensity at 0.5 T and beyond. The exact nature of this signal is not currently known, but it is not due to an irreversible change in sample environment such as water condensation on the cryostat (we have confirmed this by comparing to scans at similar field ranges taken before and after the dataset shown in Fig. 4.3c). It is possible that this background is indicative of short-range spin correlations. Near a second order transition, one does expect the critical behavior to manifest as a sharp increase of diffuse scattering. However, this diffuse scattering should diminish rapidly away from the transition, which we do not observe on the high-field side (the intensity seems to plateau after 2 T). We do not see any signatures of the transverse field transition at $\sim$2.65 T in our elastic neutron scattering data. It is likely that the transition field strongly depends on the field direction, thus very few grains in the powder would be in the correct orientation to probe this transition, leading to a small signal in the neutron scattering measurements.

Inelastic Neutron Scattering

Finally we turn to the INS data from MACS, shown in Fig. 4.4a-f. In zero field, two branches of excitations are observed at 0.2 meV and 0.6 meV, which we refer to as Branch 1 and Branch 2, respectively. The branches are gapped and appear to be dispersionless within the resolution of the measurement (the energy step size was chosen to be 0.1 meV, which is similar to the instrument resolution for our settings, $\sim$0.075 meV [86]). The gapped nature of the excitations is consistent with anisotropic interactions, such as Ising exchange, and the presence of two branches implies at least two non-equivalent sites in the magnetic unit cell. This can be easily understood based on the two local Ising axes. As discussed above, we have found a $|\boldsymbol{k}| = 0$ antiferromagnetic structure that consists of AFM moments which are collinear when considering sites with the same Ising axis orientation. Thus, each branch is expected to be two-fold degenerate. Something that is more

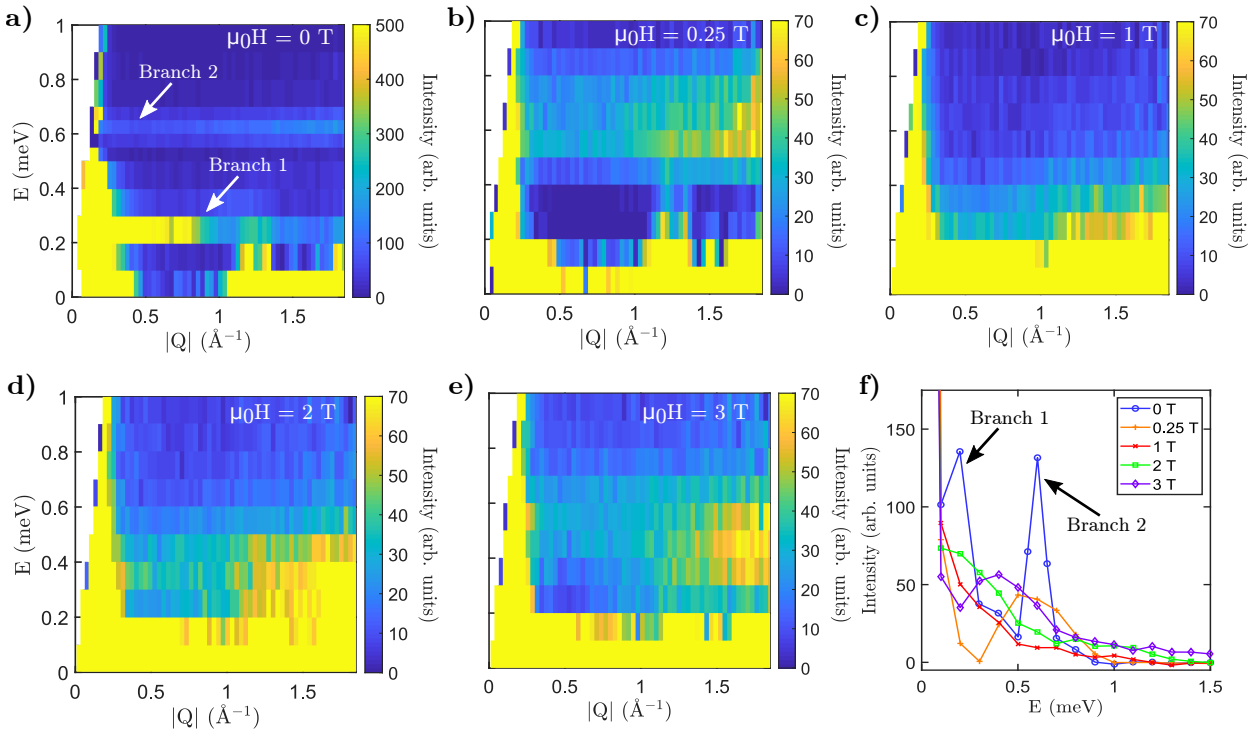

Figure 4.4: (a-e) Energy vs $|Q|$ slices at μ_0H = 0 T (a), 0.25 T (b), 1 T (c), 2 T (d), and 3 T (e) showing the evolution of two excitations. The average temperature for these slices are T_{avg} = 0.22 K, 0.18 K, 0.16 K, 0.17 K, and 0.18 K, respectively. Note: the scale factor for panel a) is higher than the other panels in order to make Branch 1 visible. Branch 1 is only visible in our 0 T data, while Branch 2 is observed to broaden and soften as the field increases to 1 T. f) Intensity vs energy cuts at Q = [1.45,1.55] Å^{-1} at various field strengths.

difficult to understand is that as the field increases, we observe only one branch clearly, despite there still being two distinct Ising axes. At 0.25 T (Fig. 4.4b), only Branch 2 remains, and is significantly broadened. The disappearance of Branch 1 might indicate a very low field transition for some field directions, but Leask *et. al* did not report any magnetic transitions below 0.5 T at 500 mK. However, Leask *et. al* did predict that the transition near 0.5 T was first order in nature for some field directions (significant hysteresis was observed in the simulated magnetization). The absence of Branch 1 in our 0.25 T data may be related to this predicted first order transition; the 0.25 T data was collected after the sample was subjected to a very high field (8 T), thus the data at 0.25 T represents the decreasing field part of the hysteresis curve, which is likely to be in a different state than the 0 T data. However, to understand all the details of the field evolution of excitations would require further study on single crystal samples.

We concern ourselves now with the behavior of Branch 2 at higher fields, which exhibits clearer signatures. As the field is increased to 1 T, Branch 2 broadens (likely due to the anisotropic g-tensor) and softens dramatically. The excitation becomes gapless near 1 T as expected for a field-induced second order phase transition. Beyond $\sim$ 1 T, the branch energy increases again, consistent with entering the field-polarized paramagnetic regime. No signature of the transverse field transition is observed in the inelastic spectrum. It is worth noting that we have not attributed any signatures in the INS spectrum to the impurity (Er_2SiO_5), even though it is also magnetic. Due to the relatively low concentration in the sample (9%), we expect the impurity will not contribute appreciably to the INS signal.

We also obtained INS data at fields up to 8 T (see Appendix B.4), where the excitations could in principle be modelled by linear spin wave theory. Additionally, Leask *et. al.* obtained exchange interactions based on a mean field approach to describing features in the magnetization curves (these parameters, when used in a Monte Carlo simulation, did reproduce many of the observed features of the magnetization curves in several directions [2]). Unfortunately, the exchange interactions as reported in that work are not uniquely assignable to specific pairs of ions in the unit cell, so a useful comparison to our data is greatly complicated. We would like to note that at least the interlayer interaction (along a) seems to be clearly defined [13], and this interaction is small compared to the other exchange interactions. This suggests that the magnetic interactions in D-$Er_2Si_2O_7$ could be quasi-2D. Indeed, the layered structure of Er^{3+} in D-$Er_2Si_2O_7$ also suggests that the magnetic interactions may be quasi-2D.

4.2.5 Conclusions

In this work we have used AC susceptibility, neutron diffraction, and inelastic neutron scattering to study the Ising-like antiferromagnetic order and field-induced behavior of the rare-earth pyrosilicate, D-$Er_2Si_2O_7$. AC susceptibility measurements with a field transverse to the Ising direction show a transition at a magnetic field strength of 2.65 T. Using neutron diffraction we have

[13] Referring to the notation in Ref. [2], this is the interaction between the atom on "sublattice 1" with itself in the next unit cell

determined the magnetic structure of D-$Er_2Si_2O_7$, which consists of moments pointing along a local direction which is close to the Ising direction determined by Leask *et. al* [2]. Our powder INS measurements reveal gapped excitations, one of which softens under an applied field and become gapless near 1 T. Due to both neutron scattering experiments being performed on powder samples, it is difficult to directly connect the transition observed in AC susceptibility on a single crystal to any signature in the neutron scattering data. However, we can state that there is a transition for a field applied perpendicular to the Ising axes, the zero-field INS spectra is consistent with Ising-like exchange, and the magnetic structure has been determined via neutron diffraction. This work sets the stage for future studies confirming the Ising-like nature of interactions in D-$Er_2Si_2O_7$ and for further study of the transverse field transition. Future work should include INS measurements on single crystals [34] in order to further elucidate the nature of the transverse-field-induced transitions in this material.

Chapter 5

Néel Ordering in the Distorted Honeycomb Pyrosilicate: C-$Er_2Si_2O_7$

5.1 Context

This chapter consists of my paper *Néel Ordering in the Distorted Honeycomb Pyrosilicate: C-$Er_2Si_2O_7$* which was published in the Journal of Physics: Condensed Matter in 2021* [**?**]. This work includes neutron diffraction, specific heat, and magnetometry measurements to characterize the ground state of C-$Er_2Si_2O_7$, which is isostructural to the quantum dimer magnet compound discussed in Chap. 3. We have found the C-$Er_2Si_2O_7$ magnetically orders into a collinear Néel state at 2.3 K, in stark contrast to $Yb_2Si_2O_7$ which does not magnetically order in the absence of a magnetic field. The discovery of this difference between the two compounds has set the stage for future work in understanding how the rare-earth ion affects the ground state nature of quantum magnets.

During the writing of this dissertation, a typo was found in the published version of the paper. In the section titled "Comparison to $Yb_2Si_2O_7$", the maximum free ion moment of Yb^{3+} and Er^{3+} was given, but labeled incorrectly and with one of the values being correct. This does not change the argument being presented. The maximum free ion moment of Yb^{3+} is 4.54 μ_B and the maximum free ion moment of Er^{3+} is 9.59 μ_B.

5.1.1 Contributions

G. Hester and C. M. Brown performed the neutron diffraction measurements. G. Hester analyzed the neutron diffraction data with assistance from S. S. Lim. T. N. DeLazzer, S. S. Lim,

*This is the Accepted Manuscript version of an article accepted for publication in the Journal of Physics: Condensed Matter. IOP Publishing Ltd is not responsible for any errors or omissions in this version of the manuscript or any version derived from it. The Version of Record is available online at DOI:10.1088/1361-648X/abd5f8.

and G. Hester performed the synthesis of C-$Er_2Si_2O_7$. G. Hester performed the magnetometry and specific heat measurements. The paper was primarily written by G. Hester with detailed comments from K. A. Ross.

5.2 Research Article

5.2.1 Overview

The rare-earth pyrosilicate family of compounds ($RE_2Si_2O_7$) hosts a variety of polymorphs, some with honeycomb-like geometries of the rare-earth sublattices, and the magnetism has yet to be deeply explored in many of the cases. Here we report on the ground state properties of C-$Er_2Si_2O_7$. C-$Er_2Si_2O_7$ crystallizes in the C 2/m space group and the Er^{3+} atoms form a distorted honeycomb lattice in the a-b plane. We have utilized specific heat, DC susceptibility, and neutron diffraction measurements to characterize C-$Er_2Si_2O_7$. Our specific heat and DC susceptibility measurements show signatures of antiferromagnetic ordering at 2.3 K. Neutron powder diffraction confirms this transition temperature and the relative intensities of the magnetic Bragg peaks are consistent with a collinear Néel state in the magnetic space group C 2'/m, with ordered moment of 6.61 μ_B canted 13° away from the c-axis toward the a-axis. These results are discussed in relation to the isostructural quantum dimer magnet compound $Yb_2Si_2O_7$.

5.2.2 Introduction

Recent efforts in the study of quantum magnetism and novel magnetic ground states have focused on the use of 4*f* magnetic atoms in different frustrated geometries (i.e. triangular [92, 93, 94], kagome [95], and pyrochlore lattices [96]) instead of the traditional 3*d* magnetic atoms, such as Cu^{2+} or Ni^{2+}. This is due to numerous advantages to 4*f* magnetic atoms over traditional 3*d* magnetic atoms. One of these advantages is 4*f* ions can often be interchanged for each other within the same structure, which tends to produce a wide variety magnetic behavior. Additionally - at the single-ion level - the effect of strong spin-orbit coupling of the 4*f* ions and the surrounding crystal electric field (CEF) is often to produce an energetically well-isolated doublet that can be mapped

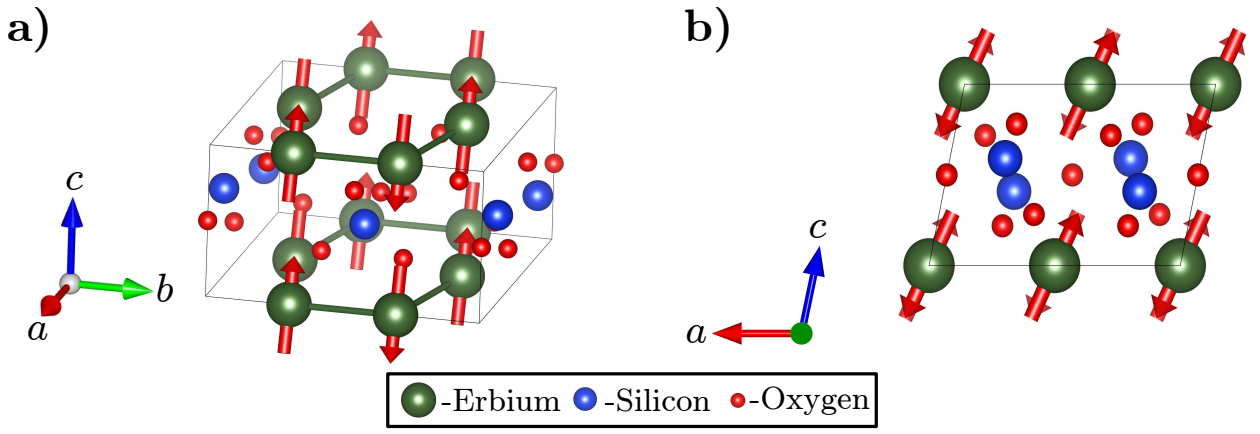

Figure 5.1: a) The crystal and magnetic structure (obtained from the refinement in Fig. 5.4a) of C-$Er_2Si_2O_7$. The Er^{3+} atoms form a distorted honeycomb lattice in the a-b plane. Here Er atoms are green, Si are blue, and O are red. b) View of the crystal and magnetic structure along the b-axis showing the separation between the layers. The interlayer distance is 4.722 Å, which is slightly larger then the nearest-neighbor bond distance of 3.477 Å. All panels of this figure were created using the Vesta software [58].

to an effective spin $\frac{1}{2}$ ($S_{\text{eff}} = 1/2$). These $S_{\text{eff}} = 1/2$ systems have been shown to exhibit many of the same quantum ground states expected for "bare" spin $\frac{1}{2}$ systems [7, 8, 9]. The highly localized $4f$ electrons are also advantageous as they lead to weak orbital overlap, and therefore weak superexchange (typically on the order of 1 K). This weak superexchange drives magnetic ordering transitions down in temperature, but also allows for field-induced transitions to generally be accessible with conventional, widely available superconducting magnets. Finally, the orbitally-active effective spins allow for bond-dependent exchange interactions, which can yield novel quantum phases such as the Kitaev quantum spin liquid [15, 97] or Quantum Spin Ice [16, 42]. The Kitaev model was originally derived for the honeycomb lattice and is therefore of particular relevance to this work, as C-$Er_2Si_2O_7$ forms a distorted honeycomb lattice of Er^{3+} ions in the a-b plane. Numerous magnetic honeycomb systems have been investigated in the context of the Kitaev model [67, 98, 99, 100], but the quantum spin liquid state of the pure Kitaev model has yet to be discovered in a real material. This provides impetus to study new honeycomb materials with strong spin-orbit coupling, which will aid theoretical and materials design efforts towards a Kitaev quantum spin liquid.

The rare-earth pyrosilicate family ($RE_2Si_2O_7$) of compounds was synthesized in the 1980's by Felsche [17]. Structures were determined for all the lanthanide atoms in this series, with many of the lanthanides exhibiting a dimorphic or polymorphic phase diagram. The interest in these compounds was primarily due to the Si-O-Si bonds in the $[Si_2O_7]^{6-}$ groups. Therefore, little work was done on the low temperature magnetic properties of the series at the time. The Er-based pyrosilicate compound $Er_2Si_2O_7$ can crystallize in three different structures depending on the synthesis temperature: the low-temperature phase P1 (Type B), the intermediate-temperature phase C2/m (Type C) and the high-temperature phase $P2_1/a$ (Type D) [17, 18]. We have recently begun exploring the low-temperature properties of some members of the rare-earth pyrosilicate series. In particular, we have studied D-$Er_2Si_2O_7$, which shows evidence of being a new experimental platform for studying the transverse-field Ising model [69]. Of more relevance to the current work, we have also studied the magnetic properties of $Yb_2Si_2O_7$[7], which forms the same C-type "thortveitite" structure as the title compound, C-$Er_2Si_2O_7$. We also note that $Lu_2Si_2O_7$, $Y_2Si_2O_7$ [101] and $Tm_2Si_2O_7$ [102] form the same structure. $Lu_2Si_2O_7$ and $Y_2Si_2O_7$ are non-magnetic, so they may provide a useful non-magnetic analog to C-$Er_2Si_2O_7$. Meanwhile, the magnetism of $Tm_2Si_2O_7$ has not been thoroughly investigated, though it does show a low-temperature Schottky-like anomaly in the specific heat [103], similar to $Yb_2Si_2O_7$. $Yb_2Si_2O_7$ does not magnetically order down to 50 mK in zero field and exhibits a field-induced phase like the triplon Bose-Einstein condensates observed in 3*d* transition metal-based dimer magnets. This brings us to the compound of current interest, C-$Er_2Si_2O_7$. C-$Er_2Si_2O_7$ is isostructural to $Yb_2Si_2O_7$, thus providing an opportunity to study how rare-earth substitution influences the magnetic ground state properties of quantum magnets with the same structures. In this thortveitite structure, the Er^{3+} ion resides in a distorted octahedral site at the $4g$ Wyckoff position, resulting in a CEF with C_2 point group symmetry. The Er-O bond lengths in this structure range from 2.234 - 2.279 Å. The [ErO_6] groups share three of their edges with adjacent groups, forming the honeycomb layers in the a-b plane. The magnetic transition temperature of C-$Er_2Si_2O_7$ has been reported to be 2.50(5) K previously [85, 104] - although the data was not shown - and magnetization measurements performed above room temperature have

been reported [105]. No further studies of the magnetic properties have been undertaken until this work.

5.2.3 Experimental Methods

Powder samples of C-$Er_2Si_2O_7$ were synthesized by grinding stoichiometric amounts of SiO_2 and Er_2O_3, pressing the reactants into a rod, and heating 8 times at 1300°C for 48 hours with thorough grinding between heatings. Phase purity was confirmed using powder x-ray diffraction. Refinement of 4 K neutron diffraction data yielded the lattice parameters: a = 6.8529(4) Å, b = 8.9446(5) Å, c = 4.7219(3) Å, $\alpha = 90°$, β = 101.763(4)°, $\gamma = 90°$. These parameters are consistent with previously published values [17]. The crystal structure and magnetic structure of C-$Er_2Si_2O_7$ are shown in Fig. 5.1.

Specific heat measurements were performed on a 1.1 mg piece of sintered powder C-$Er_2Si_2O_7$ using a Quantum Design PPMS with a dilution insert. Temperature dependent susceptibility measurements were performed on a powder sample of C-$Er_2Si_2O_7$ from the same batch, immobilized in eicosane wax, in a Quantum Design MPMS-XL system with a 100 Oe DC magnetic field. Field dependent magnetization measurements were performed on the same sample at a temperature of 1.8 K. Powder neutron diffraction measurements were performed on the BT-1 high resolution powder diffractometer at the NIST Center for Neutron Research with 60' collimation and the Ge(311) monochromator ($\lambda = 2.079$ Å). The neutron diffraction sample consisted of 3.5 grams of C-$Er_2Si_2O_7$ powder loaded in an aluminum sample canister, with 1 bar of helium exchange gas loaded at room temperature. The sample was cooled using a ^{3}He refrigerator, and measurements were performed between 0.3 and 4 K. All error bars shown in this work indicate one standard deviation.

Certain commercial equipment, instruments, or materials are identified in this document. Such identification does not imply recommendation or endorsement by the National Institute of Standards and Technology, nor does it imply that the products identified are necessarily the best available for the purpose.

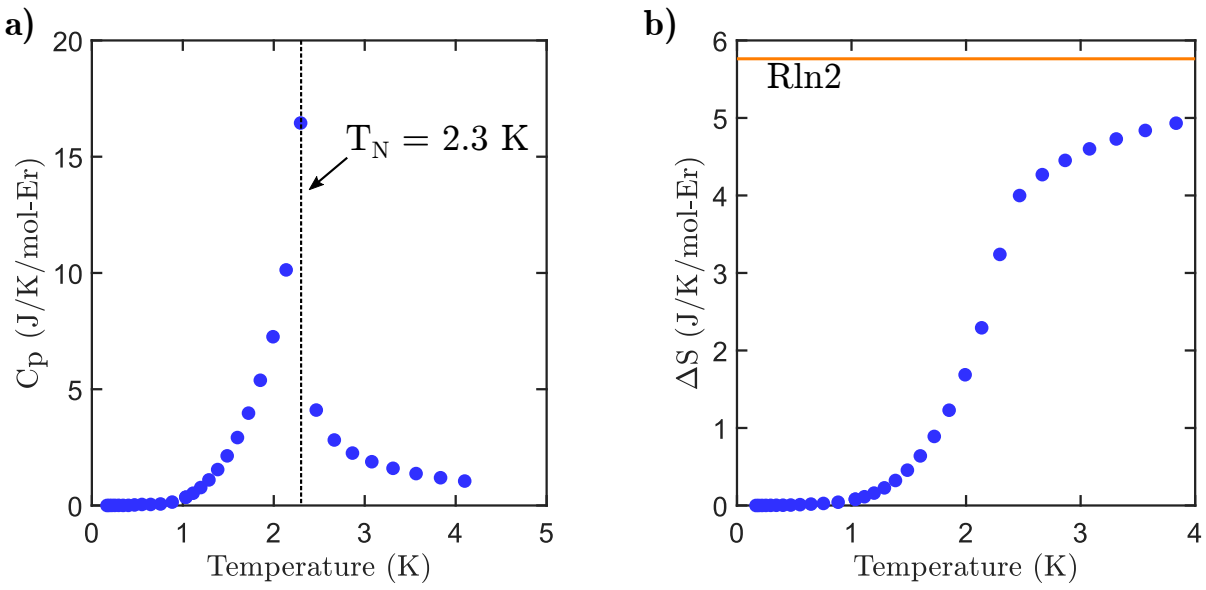

Figure 5.2: a) Heat capacity vs. temperature, $C_p(T)$, of a powder sample of C-$Er_2Si_2O_7$ using a Quantum Design PPMS with dilution insert. A lambda anomaly is observed at T_N = 2.3 K, indicative of a transition to long range magnetic order. b) Entropy calculated from the C_p vs. T shown in panel a. The entropy approaches Rln2 through the transition, consistent with what one would expect for an S_{eff} = 1/2 system.

5.2.4 Results and Discussion

Specific Heat and Magnetization

Specific heat data obtained between 150 mK and 4 K (Fig. B.1a) show a lambda anomaly at $T_N = 2.3$ K, indicating a transition to long range magnetic order. This transition temperature is close to the previously reported 2.50(5) K [85, 104], though the previous reports do not mention the type of measurement used to determine this or show any data. The entropy calculated from the specific heat is shown in Fig. B.1b. The entropy approaches Rln2 - the expected value for an S_{eff} = 1/2 system - but falls short of it, likely indicating that some short range correlations persist to temperatures higher than 4 K. The transition temperature is corroborated by the observation of a peak in the susceptibility, shown in Fig. A.13a-b. The sharp downturn in the susceptibility after the transition indicates the system enters an antiferromagnetic ground state. A Curie-Weiss fit to the inverse susceptibility is shown in Fig. A.13b. The fit was performed only for temperatures between 5 and 10 K, avoiding lower temperatures due to the onset of significant correlations, and higher temperatures due to the (likely) mixing of higher CEF levels. This fit yielded a Curie

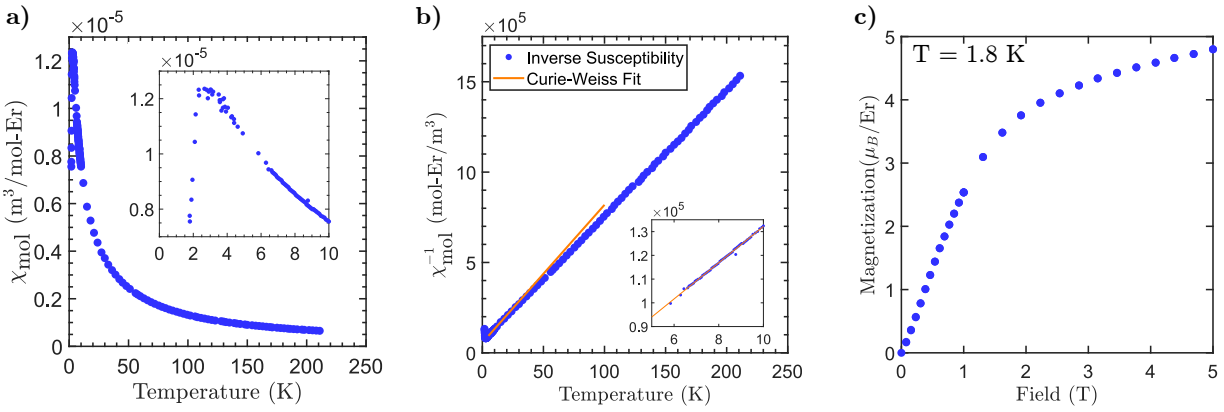

Figure 5.3: a) Susceptibility vs. temperature, $\chi(T)$, of a powder sample of C-$Er_2Si_2O_7$ in an applied field of 0.01 T. A sharp drop-off of the susceptibility occurs at 2.3 K, consistent with antiferromagnetic order. Susceptibility values are shown in SI units (m^3/mol-Er), the value in Gaussian units (emu/mol-Er) can be obtained by multiplying by 4π x 10^{-6}. (inset) Zoom-in of the low temperature region of $\chi(T)$. b) $\chi^{-1}(T)$ and fit of the Curie-Weiss law. The fit was limited to the temperature range of 5 - 10 K, yielding an effective moment of $\mu_{\text{eff}} = 9.1(5)\ \mu_B$, and a Curie-Weiss temperature of $\theta_{CW} = -7.3(2)$ K. (inset) Zoom in on the region where the Curie-Weiss fit was performed. c) Field dependent magnetization measurements performed at 1.8 K on a powder of C-$Er_2Si_2O_7$. At 5 T the magnetization appears to be approaching the saturated limit, and powder-averaged moment of 4.8 μ_B is observed.

constant of 10.4(1) mol-Er·K/emu (8.30(12) $\times$ 10^5 mol-Er·K/m^3), corresponding to an effective moment of μ_{eff} =9.1(5) μ_B, which is below the free-ion value $\mu_{\text{eff}}^{\text{free}} = g_J\sqrt{J(J+1)} = 9.58\mu_B$, where $J = 15/2$ is the total angular momentum and $g_J = 6/5$ is the Lande g-factor for Er^{3+}. The Curie-Weiss temperature was θ_{CW}=-7.3(2) K. This yields a frustration index ($f = \theta_{CW}/T_N$) of 3.2, indicating the system is only lightly frustrated. However, we note that Curie-Weiss fits can prove unreliable for rare-earth ions, with significant non-linearity in the inverse susceptibility arising from CEF effects. As the first crystal field level energy is not known for C-$Er_2Si_2O_7$, it is uncertain how accurate this fit is, even within this low temperature regime.

The field dependence of the magnetization at T=1.8 K is shown in Fig. A.13c. The magnetization is approximately linear up to 1 T, where it then begins to saturate near 5 T, though we note that a fully saturated state is not expected due to mixing with higher CEF levels as the field is increased. The powder averaged "saturated" moment at 5 T is nearly 4.8 μ_B, which falls well below the maximum allowed value of $\mu_{\text{eff}}^{\text{free}} = 9.58\mu_B$. This is not surprising, as the Kramer's doublet CEF ground state likely carries a strongly anisotropic g-factor, which will appear as a reduced

saturated moment on powder averaged data. Further, the ground state CEF wavefunctions likely do not solely consist of the maximum J_z eigenstates, which will also reduce the observed magnetic moment compared to the maximum possible value.

Neutron Diffraction

Powder neutron diffraction measurements obtained using BT-1 were refined using the FullProf software [88] and the SARAh suite (using the Kovalev tables) [89, 90]. The resulting Rietveld refinement for the magnetic structure of C-$Er_2Si_2O_7$ on the data obtained at 320 mK with 4 K data subtracted is shown in Fig. 5.4a. A symmetry analysis of the allowed $|\boldsymbol{k}|$ = 0 magnetic structures for C-$Er_2Si_2O_7$ provided four possible irreducible representations. The Rietveld refinement of C-$Er_2Si_2O_7$ yielded a $|\boldsymbol{k}|$ = 0 magnetic structure in the Γ_4 irreducible representation with the space group C2′/m. The Γ_4 irreducible representation contained two basis vectors for atom 1: ψ_5 = (2,0,0) and ψ_6 = (0, 0, 2). The basis vectors for atom 2 are the negative of the basis vectors for atom 1, guaranteeing colinear antiferromagnetism. The coefficients for these basis vectors are C_5 = -0.84(3) and C_6 = 3.03(1). These coefficients yield the magnetic structure shown in Fig. 5.1. The structure is a simple Néel structure with the moments canted 13° away from the c-axis toward the a-axis. Multiplying the coefficients by their respective basis vectors and considering the non-orthogonal axes, the ordered moment extracted from the fit is 6.61 μ_B.

The thermal evolution of the (110) magnetic Bragg peak intensity is shown in Fig. 5.4b-c. The data shown in Fig. 5.4c is a sum of the intensity over the full detector sweep used (i.e. the range of $|Q|$ values shown for the example peaks in panel b). The magnetic intensity shows the typical shape for a second order antiferromagnetic transition with a Néel temperature of 2.3 K. An attempt was made to fit the intensity in the proximity of the Néel temperature to extract the order parameter's critical exponent, β. However, the point density in the proximity of T_N was too low to accurately determine the critical exponent. Additionally, there is critical scattering that persists above T_N that further complicates the fitting of the critical exponent. The dashed line on this figure is a guide to the eye.

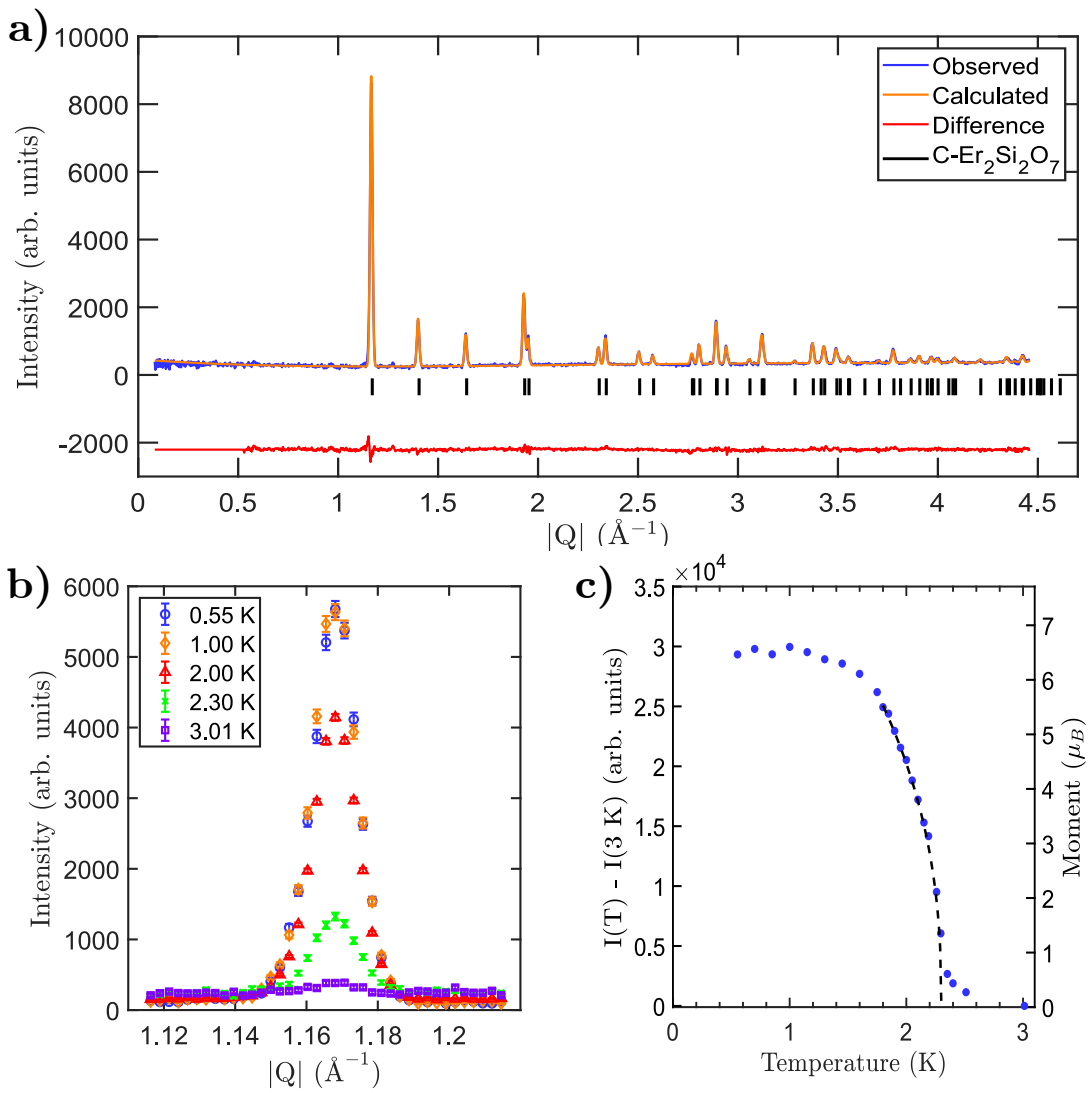

Figure 5.4: a) Rietveld refinement of neutron diffraction data measured at 320 mK with the 4 K data (nuclear Bragg peaks) subtracted, which is well fit by the $|\boldsymbol{k}| = 0$ structure shown in Fig. 5.1. b) A selection of peaks from parametric scans over the (110) Bragg peak, used for the order-parameter curve in panel c. c) Evolution of the (110) Bragg peak intensity with temperature. The black dashed line is a guide to the eye showing the extrapolation to the Néel temperature of 2.3 K, as expected based on the thermodynamic measurements above. The right-side axis shows the corresponding ordered moment, determined based on the refinement of the 320 mK data. Error bars are smaller than the points shown. Note: each intensity point shown is the sum of the intensity over the whole peak between Q = [1.11, 1.21] Å^{-1}.

Comparison to $Yb_2Si_2O_7$

As C-$Er_2Si_2O_7$ is isostructural to $Yb_2Si_2O_7$, it is worthwhile to consider why C-$Er_2Si_2O_7$ magnetically orders and $Yb_2Si_2O_7$ does not (in the absence of a magnetic field). The difference in ground states may be due to slight differences in bond lengths. The nearest-neighbor and next-nearest-neighbor bond lengths differ by 3.5% in $Yb_2Si_2O_7$, while the difference is only 2.5% for C-$Er_2Si_2O_7$. This indicates that C-$Er_2Si_2O_7$ is closer, at least in the sense of the bond lengths, to being a "perfect" honeycomb lattice. It is well-known that the ground-state of a structurally isotropic honeycomb lattice with nearest-neighbor antiferromagnetic XXZ exchange is the Néel state [106], due to the bipartite nature of the lattice. Likewise, the presence of more pronounced structural dimers in $Yb_2Si_2O_7$ compared to C-$Er_2Si_2O_7$ would naturally seem to lead to a dimerized quantum (singlet) state. However, the details of the exchange interactions in rare earth insulators is not only a matter of bond lengths — it also depends on the bond angles and the nature of the angular momentum states involved in the exchange [107]. We therefore expect some differences between C-$Er_2Si_2O_7$ and $Yb_2Si_2O_7$ to arise due to the presence of different strengths of anisotropic exchange. It would be reasonable to expect dipolar interactions to be stronger in C-$Er_2Si_2O_7$ due to the higher overall moment Er^{3+} ($\mu_{\text{eff}} = 9.1\ \mu_B$) in comparison to that of Yb^{3+} ($\mu_{\text{eff}} = 3.0\ \mu_B$) in this structure. Ideally, the exchange interactions of C-$Er_2Si_2O_7$ could be extracted via high-field inelastic neutron scattering, but this requires single crystal samples. We have not been successful in growing single crystals of C-$Er_2Si_2O_7$ via the optical floating zone technique because the high-temperature polymorph, D-$Er_2Si_2O_7$, is stabilized from the melt instead [34].

5.2.5 Conclusions

We have used specific heat, magnetic susceptibility, and neutron diffraction measurements to explore the low-temperature properties and magnetic structure of C-$Er_2Si_2O_7$. Our specific heat measurements show a sharp lambda-like anomaly at T_N = 2.3 K indicating a transition to long range magnetic order. This is corroborated by magnetic susceptibility measurements and neutron powder diffraction, which both reveal an antiferromagnetic transition at 2.3 K. Furthermore, the

neutron diffraction measurements allowed for the determination of the magnetic structure below 2.3 K. The ordered magnetic structure consists of a $|k| = 0$ antiferromagnetic Néel state, with 6.8 μ_B moments pointing in the a-c plane (13° from c). The different ground states of C-$Er_2Si_2O_7$ and the isostructural quantum dimer magnet system $Yb_2Si_2O_7$ are interesting from the perspective of understanding how the relevant rare-earth species affects the nature of exchange interactions in quantum magnets of fixed geometry. One possible avenue for future work, which would not require single crystals, is the measurement of the crystal field parameters for Er^{3+} in C-$Er_2Si_2O_7$. The C_2 point group symmetry results in eight independent Steven's parameters. These can likely be determined via inelastic neutron scattering, since there are also eight Kramer's doublets for the Er^{3+} ion ($J = \frac{15}{2}$), thus their energies and relative intensities provide enough constraints to determine the crystal field Hamiltonian. This would also allow some insight into the crystal field Hamiltonian for $Yb_2Si_2O_7$, an important open question that cannot be easily addressed using inelastic neutron scattering directly due to there being fewer Kramer's doublets available (only four in that case), which can result in an under-constrained fit [108]. An additional avenue for future work would be the determination of the exchange interactions for C-$Er_2Si_2O_7$ using inelastic neutron scattering on single crystal samples, if they become available. This would be of great benefit to further enable the understanding of how different rare-earth species affect the nature of the exchange interactions in quantum magnets.

Chapter 6

Summary and Future Work

6.1 Summary

In this dissertation, I have outlined our experiments and results on three members of the rare-earth pyrosilicate family of compounds: $Yb_2Si_2O_7$, D-$Er_2Si_2O_7$, and C-$Er_2Si_2O_7$. In Chapter 3, I presented our paper, *Novel Strongly Spin-Orbit Coupled Quantum Dimer Magnet: $Yb_2Si_2O_7$*. In this paper we utilized heat capacity, ultrasound velocity, and neutron scattering measurements to characterize the quantum dimer magnet ground state and field-induced phase of $Yb_2Si_2O_7$. At zero field, we observed no signatures of magnetic ordering down to 50 mK, but a Schottky anomaly which released R ln 2 of entropy per mole, consistent with an effective spin-$\frac{1}{2}$ picture, was measured via heat capacity. This lack of magnetic ordering in conjunction with our observation of a coherent triplon excitation at zero-field confirms that $Yb_2Si_2O_7$ is a new, rare-earth example of a quantum dimer magnet ground state. When a magnetic field is applied along the c-axis of this system, a transition is observed in ultrasound velocity and heat capacity measurements into a $|\overrightarrow{k}|$ = 0 antiferromagnetic structure. This is corroborated by the emergence of a Goldstone mode in the inelastic neutron spectrum, consistent with the system spontaneously breaking a continuous symmetry. The Goldstone mode is expected for a field-induced triplon BEC, indicating $Yb_2Si_2O_7$ may be the first field-induced triplon BEC crafted with rare-earth ions. As the magnetic field strength is increased, an unexpected change in the ultrasound velocity is observed at H_m = 1.2 T, but the Goldstone mode persists, indicating this state still spontaneously breaks a continuous symmetry. The exact cause for this transition is not currently understood, but recent theoretical works by Flynn, et. al. [84] indicated that this signature may arise due to competing forms of weak anisotropy. As the field is increased to 1.4 T, the system exits the antiferromagnetic phase and is now a field-polarized paramagnet. In the field-polarized paramagnet regime, we were able to fit the inelastic neutron scattering spectrum using linear spin-wave theory, yielding exchange interactions

that are U(1) symmetric, as required for a field-induced triplon BEC. These measurements provide strong evidence that $Yb_2Si_2O_7$ is the first rare-earth based triplon BEC. The naturally lower energy exchange interactions of the rare-earth atoms - due to the highly localized $4f$ electrons - result in very low critical fields that are accessible by virtually all laboratory based magnets, something that is not true for many of the $3d$ transition metal based BEC systems. Additionally, the inherent anisotropy expected from a rare-earth ion allows for the possibility of probing how the BEC theory breaks down in the regime of weak anisotropy. Overall, $Yb_2Si_2O_7$ provides an exciting playground for probing BEC physics and adds another "simple" quantum state to the roster of states that have been observed both in bare spin-$\frac{1}{2}$ systems and pseudo spin-$\frac{1}{2}$ systems.

Our paper, *Magnetic properties of the Ising-like rare-earth pyrosilicate: D-$Er_2Si_2O_7$*, is presented in Chapter 4. In this work, we used AC susceptibility, neutron diffraction, and powder inelastic neutron scattering to characterize the ground state and field-induced behavior of the quantum magnet, D-$Er_2Si_2O_7$. D-$Er_2Si_2O_7$ magnetically orders at 1.9 K and a Rietveld refinement of our neutron diffraction measurements confirms the system magnetically orders in a $|\overrightarrow{k}| = 0$ magnetic structure. This structure is consistent with the previously predicted structure derived from magnetometry measurements and Monte-Carlo simulations [2]. Our zero-field powder inelastic neutron scattering spectrum show two excitations, one at 0.2 meV and one at 0.6 meV. The latter excitation softens in an applied magnetic field, reaching zero energy near 1 T, consistent with the system undergoing a quantum phase transition. The inelastic neutron scattering was performed on a powder which means the field is applied in all directions. It was not possible to see signatures of TFIM if they are present. However, this work does give a hint that D-$Er_2Si_2O_7$ may be a TFIM system. Only a few experimental realizations of the TFIM are currently known, yet this model is highly relevant regarding non-equilibrium quantum dynamics [77] and quantum computing [109]. If D-$Er_2Si_2O_7$ can be confirmed to be a new transverse field Ising model system, it will allow for the advancement of theoretical understanding of the TFIM and anisotropic exchange in rare-earth based compounds.

Chapter 5 consists of our paper, *Néel Ordering in the Distorted Honeycomb Pyrosilicate: C-$Er_2Si_2O_7$*. In this work, we used powder neutron diffraction, heat capacity, and magnetometry to characterize the magnetic order in C-$Er_2Si_2O_7$. Our heat capacity and magnetometry data found the Néel temperature for the magnetic ordering to be 2.3 K. We then performed a Rietveld refinement on the powder neutron diffraction data to find a structure consistent with a collinear Néel state in the magnetic space group C2'/m, with ordered moment of 6.61 μ_B canted 13° away from the c-axis toward the a-axis. C-$Er_2Si_2O_7$ is isostructural to the quantum dimer magnet compound, $Yb_2Si_2O_7$, yet C-$Er_2Si_2O_7$ magnetically orders while $Yb_2Si_2O_7$ does not magnetically order in zero field. The understanding for this difference is not currently clear, but it is not surprising given the sensitivity of magnetic states to the exchange and single ion anisotropy.

6.2 Future Work

There are numerous possible avenues for research in the pyrosilicate family of compounds I have discussed in this work. Regarding $Yb_2Si_2O_7$, there are a few outstanding questions: (1) How isotropic is this system? We are able to state that the anisotropy must be less than 16% of the $\overline{J}_{\text{intra}}$ exchange interaction strength, but this only sets the upper bound for the anisotropy. (2) How does the system act for different field directions? (3) Does the transition lie within the BEC universality class? The first two of these questions can be addressed by performing inelastic neutron scattering measurements along a different field direction, allowing for more robust fitting of the spin waves with linear spin wave theory. The third question may be addressed by performing numerous low temperature magnetic field sweeps that probe the magnetization of the system, such as magnetometry. One other extremely promising avenue that expands upon the unique features of $Yb_2Si_2O_7$ is in the realm of Bose-glass physics. The Bose-glass state in a magnetic system can be realized by doping a BEC compound with non-magnetic impurities. These impurities affect the field induced phases of the system and exhibit a form of Anderson localization. A rare-earth based system is ideal for this type of study due to the interchangeability of the lanthanide atoms.

In the Ising-like material, D-$Er_2Si_2O_7$, the most pressing question is what is the nature of the exchange interactions and how are (might) these be connected to quantum criticality. This question can likely be resolved by performing single crystal inelastic neutron scattering measurements with the field applied transverse to the Ising direction. These measurements would allow for a tracking of the mode softening and high-field data can be fit with linear spin wave theory to extract the exchange parameters. With the exchange interactions and tracking of the mode softening we will be able to further study of the phase transition at 2.65 T in a transverse field, thus shedding light on any quantum criticality in the system.

Finally, the compound C-$Er_2Si_2O_7$ provides a unique opportunity to better understand exchange interactions in rare earth oxides. Measurement of the exchange interactions of C-$Er_2Si_2O_7$, if single crystals become available, may show why C-$Er_2Si_2O_7$ magnetically orders. Additionally, if single crystals do not become available, powder inelastic neutron scattering can be used to measure the crystal electric field levels. Since C-$Er_2Si_2O_7$ has the same structure as $Yb_2Si_2O_7$ these parameters can be scaled to garner an understanding of $Yb_2Si_2O_7$'s crystal electric field [110]. Overall, the rare-earth pyrosilicate family of compounds shows promise for being a new system of compounds that can advance our understanding of the ground states of rare-earth based quantum magnets.

Bibliography

[1] B. Zygelman, *A First Introduction to Quantum Computing and Information* (2018).

[2] M. Leask, P. Tapster, and M. Wells, Journal of Physics C: Solid State Physics **19**, 1173 (1986).

[3] P. W. Shor, in *Proceedings 35th annual symposium on foundations of computer science* (Ieee, 1994), pp. 124–134.

[4] P. Kairys, A. D. King, I. Ozfidan, K. Boothby, J. Raymond, A. Banerjee, and T. S. Humble, arXiv preprint arXiv:2003.01019 (2020).

[5] H.-L. Huang, D. Wu, D. Fan, and X. Zhu, Science China Information Sciences **63**, 1 (2020).

[6] L. Henriet, L. Beguin, A. Signoles, T. Lahaye, A. Browaeys, G.-O. Reymond, and C. Jurczak, Quantum **4**, 327 (2020).

[7] G. Hester, H. S. Nair, T. Reeder, D. R. Yahne, T. N. DeLazzer, L. Berges, D. Ziat, J. R. Neilson, A. A. Aczel, G. Sala, et al., Phys. Rev. Lett. **123**, 027201 (2019).

[8] J. G. Rau and M. J. P. Gingras, Phys. Rev. B **98**, 054408 (2018).

[9] L. S. Wu, S. E. Nikitin, Z. Wang, W. Zhu, C. D. Batista, A. M. Tsvelik, A. M. Samarakoon, D. A. Tennant, M. Brando, L. Vasylechko, et al., Nature Communications **10** (2019).

[10] G. Hester, T. N. DeLazzer, S. S. Lim, C. M. Brown, and K. A. Ross, Journal of Physics: Condensed Matter **33**, 125804 (2020).

[11] M. P. Shores, E. A. Nytko, B. M. Bartlett, and D. G. Nocera, Journal of the American Chemical Society **127**, 13462 (2005).

[12] J. G. Bednorz and K. A. Müller, Zeitschrift für Physik B Condensed Matter **64**, 189 (1986).

[13] H. Tanaka, F. Yamada, T. Ono, T. Sakakibara, Y. Uwatoko, A. Oosawa, K. Kakurai, and K. Goto, Journal of Magnetism and Magnetic Materials **310**, 1343 (2007).

[14] C. Balz, B. Lake, A. N. Islam, Y. Singh, J. A. Rodriguez-Rivera, T. Guidi, E. M. Wheeler, G. G. Simeoni, and H. Ryll, Phys. Rev. B **95**, 174414 (2017).

[15] A. Kitaev, Annals of Physics **321**, 2 (2006).

[16] K. A. Ross, L. Savary, B. D. Gaulin, and L. Balents, Phys. Rev. X **1**, 021002 (2011).

[17] J. Felsche, Journal of The Less-Common Metals **21**, 1 (1970).

[18] Y. I. Smolin and Y. F. Shepelev, Acta Crystallographica Section B **26**, 484 (1970).

[19] V. Zapf, M. Jaime, and C. D. Batista, Reviews of Modern Physics **86**, 563 (2014).

[20] T. Matsubara and H. Matsuda, Progress of Theoretical Physics **16**, 569 (1956).

[21] O. Nohadani, S. Wessel, and S. Haas, Phys. Rev. Lett. **95**, 227201 (2005).

[22] H. Kageyama, M. Nishi, N. Aso, K. Onizuka, T. Yosihama, K. Nukui, K. Kodama, K. Kakurai, and Y. Ueda, Phys. Rev. Lett. **84**, 5876 (2000).

[23] L. Onsager, Physical Review **65**, 117 (1944).

[24] A. W. Kinross, M. Fu, T. J. Munsie, H. A. Dabkowska, G. M. Luke, S. Sachdev, and T. Imai, Phys. Rev. X **4**, 031008 (2014).

[25] J. Chadwick, Nature **129**, 312 (1932).

[26] W. Bothe and H. Becker, Journal for Physics **66**, 289 (1930).

[27] I. Joliot-Curie and F. Joliot-Curie, *Émission de protons de grande vitesse par les substances hydrogénées sous l'influence des rayons tres pénétrants* (Gauthier-Villars, 1932).

[28] T. E. Mason, T. J. Gawne, S. E. Nagler, M. B. Nestor, and J. M. Carpenter, Acta Crystallographica Section A **69**, 37 (2013).

[29] T. Chatterji, *Magnetic neutron scattering* (Elsevier, 2006).

[30] G. L. Squires, *Introduction to the theory of thermal neutron scattering* (Courier Corporation, 1996).

[31] V. O. Garlea, B. C. Chakoumakos, S. A. Moore, G. B. Taylor, T. Chae, R. G. Maples, R. A. Riedel, G. W. Lynn, and D. L. Selby, Applied Physics A: Materials Science and Processing **99**, 531 (2010).

[32] G. Ehlers, A. A. Podlesnyak, J. L. Niedziela, E. B. Iverson, and P. E. Sokol, Review of Scientific Instruments **82**, 085108 (2011).

[33] *Physical Property Measurement System - Heat Capacity Option User's Manual*, Quantum Design, San Deigo, CA, 11th ed. (2004).

[34] H. Nair, T. DeLazzer, T. Reeder, A. Sikorski, G. Hester, and K. Ross, Crystals **9**, 10 (2019), ISSN 2073-4352.

[35] *Physical Property Measurement System - Dilution Refrigerator User's Manual*, Quantum Design, San Deigo, CA, 6th ed. (2013).

[36] *Magnetic Property Measurement System - MPMS 3 User's Manual*, Quantum Design, San Deigo, CA, 15th ed. (2016).

[37] V. S. Zapf, D. Zocco, B. R. Hansen, M. Jaime, N. Harrison, C. D. Batista, M. Kenzelmann, C. Niedermayer, A. Lacerda, and A. Paduan-Filho, Phys. Rev. Lett. **96**, 077204 (2006).

[38] M. Jaime, V. F. Correa, N. Harrison, C. D. Batista, N. Kawashima, Y. Kazuma, G. A. Jorge, R. Stern, I. Heinmaa, S. A. Zvyagin, et al., Phys. Rev. Lett. **93**, 087203 (2004).

[39] E. C. Samulon, Y. J. Jo, P. Sengupta, C. D. Batista, M. Jaime, L. Balicas, and I. R. Fisher, Phys. Rev. B **77**, 214441 (2008).

[40] A. A. Aczel, Y. Kohama, C. Marcenat, F. Weickert, M. Jaime, O. E. Ayala-Valenzuela, R. D. McDonald, S. D. Selesnic, H. A. Dabkowska, and G. M. Luke, Phys. Rev. Lett. **103**, 207203 (2009).

[41] A. A. Aczel, Y. Kohama, M. Jaime, K. Ninios, H. B. Chan, L. Balicas, H. A. Dabkowska, and G. M. Luke, Phys. Rev. B **79**, 100409 (2009).

[42] M. Hermele, M. P. A. Fisher, and L. Balents, Phys. Rev. B **69**, 064404 (2004).

[43] S. Onoda and Y. Tanaka, Phys. Rev. Lett. **105**, 047201 (2010).

[44] M. J. Gingras and P. A. McClarty, Reports on Progress in Physics **77**, 056501 (2014).

[45] G. Jackeli and G. Khaliullin, Phys. Rev. Lett. **102**, 017205 (2009).

[46] A. M. Hallas, J. P. Gaudet, N. P. Butch, M. Tachibana, R. S. Freitas, G. M. Luke, C. R. Wiebe, and B. D. Gaulin, Phys. Rev. B **93**, 100403 (2016).

[47] L. S. Wu, W. J. Gannon, I. A. Zaliznyak, A. M. Tsvelik, M. Brockmann, J.-S. Caux, M. S. Kim, Y. Qiu, J. R. D. Copley, G. Ehlers, et al., Science **352**, 1206 (2016).

[48] S. Ono, J. Despault, L. Calvert, and J. Taylor, Journal of the Less Common Metals **22**, 51 (1970).

[49] P. Gegenwart, H. Aoki, T. Cichorek, J. Custers, N. Harrison, M. Jaime, M. Lang, A. Ochiai, and F. Steglich, Physica B: Condensed Matter **312**, 315 (2002).

[50] J. G. Rau, L. S. Wu, A. F. May, L. Poudel, B. Winn, V. O. Garlea, A. Huq, P. Whitfield, A. E. Taylor, M. D. Lumsden, et al., Phys. Rev. Lett. **116**, 257204 (2016).

[51] I. Kimchi, A. Nahum, and T. Senthil, Phys. Rev. X **8**, 31028 (2018).

[52] A. Ochiai, T. Inukai, and T. Matsumura, Journal of the Physical Society of Japan **76** (2007).

[53] Y. Kato, M. Kosaka, H. Nowatari, Y. Saiga, A. Yamada, T. Kobiyama, S. Katano, K. Ohoyama, H. Suzuki, N. Aso, et al., Journal of the Physical Society of Japan **77** (2008).

[54] D. D. Khalyavin, D. T. Adroja, P. Manuel, A. Daoud-Aladine, M. Kosaka, K. Kondo, K. A. McEwen, J. H. Pixley, and Q. Si, Phys. Rev. B **87**, 220406 (2013).

[55] Y. Nakanishi, F. Shichinomiya, M. Koseki, G. Koseki, R. Kashiwazaki, K. Deto, M. Nakamura, M. Yoshizawa, and M. Kosaka, Journal of Physics: Conference Series **400** (2012).

[56] K. Hara, S. Matsuda, E. Matsuoka, K. Tanigaki, A. Ochiai, S. Nakamura, T. Nojima, and K. Katoh, Phys. Rev. B **85**, 144416 (2012).

[57] S. Kittaka, T. Sugiyama, Y. Shimura, T. Sakakibara, S. Matsuda, and A. Ochiai, Journal of the Korean Physical Society **62**, 2088 (2013).

[58] K. Momma and F. Izumi, Journal of Applied Crystallography **44**, 1272 (2011).

[59] *See Supplemental Information*.

[60] R. T. Azuah, L. R. Kneller, Y. Qiu, P. L. Tregenna-Piggott, C. M. Brown, J. R. Copley, and R. M. Dimeo, Journal of Research of the National Institute of Standards and Technology **114**, 341 (2009).

[61] Z. Wang, D. L. Quintero-Castro, S. Zherlitsyn, S. Yasin, Y. Skourski, A. T. M. N. Islam, B. Lake, J. Deisenhofer, and A. Loidl, Phys. Rev. Lett. **116**, 147201 (2016).

[62] O. Chiatti, A. Sytcheva, J. Wosnitza, S. Zherlitsyn, A. A. Zvyagin, V. S. Zapf, M. Jaime, and A. Paduan-Filho, Phys. Rev. B **78**, 094406 (2008).

[63] Y. Kohama, A. V. Sologubenko, N. R. Dilley, V. S. Zapf, M. Jaime, J. A. Mydosh, A. Paduan-Filho, K. A. Al-Hassanieh, P. Sengupta, S. Gangadharaiah, et al., Phys. Rev. Lett. **106**, 1 (2011), ISSN 00319007.

[64] T. Giamarchi, C. Rüegg, and O. Tchernyshyov, Nature Physics **4**, 198 (2008).

[65] F.-Y. Li, Y.-D. Li, Y. Yu, A. Paramenkanti, and G. Chen, Phys. Rev. B **95**, 1 (2017).

[66] S. Hwan Chun, J. W. Kim, J. Kim, H. Zheng, C. C. Stoumpos, C. D. Malliakas, J. F. Mitchell, K. Mehlawat, Y. Singh, Y. Choi, et al., Nature Physics **11**, 462 (2015).

[67] G. Jackeli and G. Khaliullin, Phys. Rev. Lett. **110**, 1 (2013).

[68] J. Chaloupka and G. Khaliullin, Phys. Rev. B **92**, 1 (2015).

[69] G. Hester, T. N. DeLazzer, D. R. Yahne, C. L. Sarkis, H. D. Zhao, J. A. R. Rivera, S. Calder, and K. A. Ross, pp. 1–10 (2020), arXiv:2008.00041.

[70] W. Wolf, Brazilian Journal of Physics **30**, 794 (2000).

[71] M. E. Fisher, Physica A: Statistical Mechanics and its Applications **106**, 28 (1981).

[72] A. Dutta, G. Aeppli, B. K. Chakrabarti, U. Divakaran, T. F. Rosenbaum, and D. Sen, *Quantum phase transitions in transverse field spin models: from statistical physics to quantum information* (Cambridge University Press, 2015).

[73] Z. Wang, T. Lorenz, D. I. Gorbunov, P. T. Cong, Y. Kohama, S. Niesen, O. Breunig, J. Engelmayer, A. Herman, J. Wu, et al., Phys. Rev. Lett. **120**, 207205 (2018).

[74] Z. Wang, M. Schmidt, A. Loidl, J. Wu, H. Zou, W. Yang, C. Dong, Y. Kohama, K. Kindo, D. I. Gorbunov, et al., Phys. Rev. Lett. **123**, 67202 (2019).

[75] P. Beauvillain, J. P. Renard, I. Laursen, and P. J. Walker, Phys. Rev. B **18**, 3360 (1978).

[76] M. J. P. Gingras and P. Henelius, Journal of Physics: Conference Series **320**, 012001 (2011).

[77] D. Silevitch, C. Tang, G. Aeppli, and T. Rosenbaum, Nature Communications **10** (2019).

[78] A. M. Hallas, J. Gaudet, and B. D. Gaulin, Annual Review of Condensed Matter Physics pp. 105–124 (2017).

[79] J. S. Gardner, M. J. P. Gingras, and J. E. Greedan, Reviews of Modern Physics **82**, 53 (2010).

[80] W. Liu, Z. Zhang, J. Ji, Y. Liu, J. Li, X. Wang, H. Lei, G. Chen, and Q. Zhang, Chinese Physics Letters **35** (2018).

[81] M. Baenitz, P. Schlender, J. Sichelschmidt, Y. A. Onykiienko, Z. Zangeneh, K. M. Ranjith, R. Sarkar, L. Hozoi, H. C. Walker, J. C. Orain, et al., Phys. Rev. B **98**, 220409(R) (2018).

[82] M. M. Bordelon, E. Kenney, C. Liu, T. Hogan, L. Posthuma, M. Kavand, Y. Lyu, M. Sherwin, N. P. Butch, C. Brown, et al., Nature Physics **15**, 1058 (2019).

[83] J. Xing, L. D. Sanjeewa, J. Kim, G. R. Stewart, A. Podlesnyak, and A. S. Sefat, Phys. Rev. B **100**, 220407(R) (2019).

[84] M. O. Flynn, T. E. Baker, S. Jindal, and R. R. P. Singh, arXiv: 2001.08219 (2020).

[85] A. Maqsood, Journal of Materials Science **16**, 2198 (1981).

[86] J. A. Rodriguez, D. M. Adler, P. C. Brand, C. Broholm, J. C. Cook, C. Brocker, R. Hammond, Z. Huang, P. Hundertmark, J. W. Lynn, et al., Measurement Science and Technology **19**, 1 (2008).

[87] V. O. Garlea, B. C. Chakoumakos, S. A. Moore, G. B. Taylor, T. Chae, R. G. Maples, R. A. Riedel, G. W. Lynn, and D. L. Selby, Applied Physics A **99**, 531 (2010).

[88] J. Rodríguez-Carvajal, Physica B: Condensed Matter **192**, 55 (1993).

[89] A. Wills, Z Kristallogr **30**, 39 (2009).

[90] A. Wills, Physica B: Condensed Matter **276**, 680 (2000).

[91] D. Phanon and R. Černỳ, Zeitschrift für anorganische und allgemeine Chemie **634**, 1833 (2008).

[92] R. Sarkar, P. Schlender, V. Grinenko, E. Haeussler, P. J. Baker, T. Doert, and H.-H. Klauss, Phys. Rev. B **100**, 241116 (2019).

[93] D. R. Yahne, L. D. Sanjeewa, A. S. Sefat, B. S. Stadelman, J. W. Kolis, S. Calder, and K. A. Ross, Phys. Rev. B **102**, 104423 (2020).

[94] J. A. M. Paddison, M. Daum, Z. Dun, G. Ehlers, Y. Liu, M. B. Stone, H. Zhou, and M. Mourigal, Nature Physics **13**, 117 (2016).

[95] M. Ashtar, J. Guo, Z. Wan, Y. Wang, G. Gong, Y. Liu, Y. Su, and Z. Tian, Inorganic Chemistry **59**, 5368 (2020).

[96] J. G. Rau and M. J. Gingras, Annual Review of Condensed Matter Physics (2019).

[97] G. Jackeli and G. Khaliullin, Phys. Rev. Lett. **102**, 2 (2009).

[98] A. Banerjee, C. A. Bridges, J.-Q. Yan, A. A. Aczel, L. Li, M. B. Stone, G. E. Granroth, M. D. Lumsden, Y. Yiu, J. Knolle, et al., Nature Materials **15**, 733 (2016).

[99] Y. Choi, C. Lee, S. Lee, S. Yoon, W.-J. Lee, J. Park, A. Ali, Y. Singh, J.-C. Orain, G. Kim, et al., Phys. Rev. Lett. **122**, 167202 (2019).

[100] S. Hwan Chun, J. W. Kim, J. Kim, H. Zheng, C. C. Stoumpos, C. D. Malliakas, J. F. Mitchell, K. Mehlawat, Y. Singh, Y. Choi, et al., Nature Physics **11**, 462 (2015).

[101] G. u. J. Redhammer and G. Roth, Acta Crystallographica Section C: Crystal Structure Communications **59**, i103 (2003).

[102] V. Kahlenberg and P. Aichholzer, Acta Crystallographica Section E: Structure Reports Online **70**, i34 (2014).

[103] M. Ciomaga Hatnean, O. A. Petrenko, M. R. Lees, T. E. Orton, and G. Balakrishnan, Crystal Growth & Design **20**, 6636 (2020).

[104] A. Maqsood, B. M. Wanklyn, and G. Garton, Journal of Crystal Growth **46**, 671 (1979).

[105] S. Ameer, A. Faraz, A. Maqsood, and N. M. Ahmad, Journal of Nano Research **17**, 85 (2012).

[106] J. B. Fouet, P. Sindzingre, and C. Lhuillier, European Physical Journal B **20**, 241 (2001).

[107] J. G. Rau and M. J. P. Gingras, Phys. Rev. B **98**, 054408 (2018).

[108] C. Sarkis, J. G. Rau, L. Sanjeewa, M. Powell, J. Kolis, J. Marbey, S. Hill, J. Rodriguez-Rivera, H. Nair, D. Yahne, et al., Phys. Rev. B **102**, 134418 (2020).

[109] J.-i. Inoue, The European Physical Journal Special Topics **224**, 149 (2015).

[110] A. Bertin, Y. Chapuis, P. D. de Réotier, and A. Yaouanc, Journal of Physics: Condensed Matter **24**, 256003 (2012).

[111] M. Rotter, D. Manh Le, J. Keller, L. G. Pascut, T. Hoffmann, M. Doerr, R. Schedler, P. Fabi, S. Rotter, M. Banks, et al., *Mcphase users manual: Symmetry considerations for crystal field parameters*, URL http://www2.cpfs.mpg.de/~rotter/homepage_mcphase/manual/manual.html.

[112] A. Abragam and B. Bleaney, *Electron paramagnetic resonance of transition ions* (OUP Oxford, 2012).

[113] J. Quilliam, K. Ross, A. Del Maestro, M. Gingras, L. Corruccini, and J. Kycia, Physical Review Letters **99**, 097201 (2007).

[114] Q. Gu and J. L. Shen, Eur. Phys. J. B **18**, 63 (2000).

[115] M. Troyer, H. Tsunetsugu, and D. Würtz, Physical Review B **50**, 13515 (1994).

[116] G. Quirion, X. Han, and M. L. Plumer, Phys. Rev. B **84**, 014408 (2011).

[117] S. Toth and B. Lake, Journal of Physics Condensed Matter **27** (2015).

[118] A. Scheie, Journal of Low Temperature Physics **193**, 60 (2018).

Appendix A

Supplemental Information on $Yb_2Si_2O_7$

A.1 Sample Preparation

Polycrystalline $Yb_2Si_2O_7$ was synthesized by combining stoichiometric amounts of Yb_2O_3 and SiO_2, pressing under hydrostatic pressure of $\sim$480 kPa, and heating 4-5 times at 1350°C for 48 hours, with regrinding between heatings to promote reaction, until phase purity was achieved (as confirmed by powder x-ray diffraction in air). Sintered cylindrical rods with diameter of 8 mm were prepared from these powders for optical floating zone crystal growth. A Crystal Systems furnace (FZ-T-10000-H-VIII-VPO-PC) was used for the crystal growth. Multiple growths were performed to optimize the parameters. The most successful growths were performed with 1.5 kW lamps (70-73% power), with a growth rate of 3-5 mm/hr, under an atmosphere of flowing oxygen (1-2L / min), with a counterrotation of the upper and lower rods of 20 rpm. Every growth resulted in cracked boules, which upon further study by Laue x-ray diffraction, were found to be multi-crystalline. The boules were broken into separate single crystals (typical size approximately 3 $\times$ 3 $\times$ 2 mm^3) which were clear and colorless (see Fig. 1c of main text).

A.2 Crystal Electric Field Considerations

The low point group symmetry of Yb^{3+} in $Yb_2Si_2O_7$ (C_2) leads to nine independent Steven's parameters in a crystal field Hamiltonian [111]. Determining these experimentally, for example by an inelastic neutron scattering measurement of the single ion energy levels, is an underdetermined problem, since such an experiment only gives access to three transitions (between the four Kramers doublets). Thus, the CEF ground state for $Yb_2Si_2O_7$ is experimentally unknown. However, our observations do restrict some of the properties of the CEF ground state. Perhaps most significantly, we find that the $\psi_{1,\pm1}$ modes are not easily visible via inelastic neutron scattering at E_i = 1.55 meV. This can be explained if the CEF ground state doublet for Yb^{3+} does not have a significant matrix

element for transitions induced by J_+ or J_-. For example, a CEF ground state doublet that is composed primarily of a single $|J_z\rangle$ eigenstate (except $|J_z\rangle = \pm 1/2$), will have vanishingly small matrix elements to the excited $\psi_{1,\pm 1}$ states, as discussed below.

Assuming XXZ symmetry for the intradimer interactions, the dimer eigenstates are given by:

$$
\begin{aligned}
|\psi_{0,0}\rangle &= \frac{1}{\sqrt{2}}(|\uparrow\downarrow\rangle - |\downarrow\uparrow\rangle) \\
|\psi_{1,+1}\rangle &= |\uparrow\uparrow\rangle \\
|\psi_{1,-1}\rangle &= |\downarrow\downarrow\rangle \\
|\psi_{1,0}\rangle &= \frac{1}{\sqrt{2}}(|\uparrow\downarrow\rangle + |\downarrow\uparrow\rangle)
\end{aligned}
$$

where the pseudo-spins can be identified as the CEF Kramer's doublet ground states $|\pm\rangle$, i.e., $|\uparrow\rangle = |+\rangle$ and $|\downarrow\rangle = |-\rangle$. These Kramer's doublet wavefunctions can be expressed as linear combinations of $\mathsf{J_z}$ eigenstates, $|J, M_J\rangle$, within a constant J manifold [112]:

$$
\begin{aligned}
|+\rangle &= \sum_{M_J=-J}^{J} C_{M_J}|J, M_J\rangle, \\
|-\rangle &= \sum_{M_J=-J}^{J} C^*_{M_J}(-1)^{J-M_J}|J, -M_J\rangle
\end{aligned}
$$

The neutron scattering intensity for transitions from the ground state to the excited states of an isolated dimer are proportional to:

$$
\begin{aligned}
I \propto &\langle\psi_{0,0}|\mathsf{J_{z1}}|\psi_{1,\pm1}\rangle^2 + \langle\psi_{0,0}|\mathsf{J_{+1}}|\psi_{1,\pm1}\rangle^2 + \langle\psi_{0,0}|\mathsf{J_{-1}}|\psi_{1,\pm1}\rangle^2 + \dots \\
&\langle\psi_{0,0}|\mathsf{J_{z2}}|\psi_{1,\pm1}\rangle^2 + \langle\psi_{0,0}|\mathsf{J_{+2}}|\psi_{1,\pm1}\rangle^2 + \langle\psi_{0,0}|\mathsf{J_{-2}}|\psi_{1,\pm1}\rangle^2,
\end{aligned}
$$

where, for example, $\mathsf{J_{z1}}$ indicates the operator acts on site 1.

As a concrete example, for $|\pm\rangle = |7/2, \pm 7/2\rangle$ (which we abbreviate as $|\pm 7/2\rangle$), the first term gives,

$$\frac{1}{2}\Big(\langle 7/2|\mathsf{J_{z1}}|\pm 7/2\rangle\langle -7/2|\pm 7/2\rangle - \langle -7/2|\mathsf{J_{z1}}|\pm 7/2\rangle\langle 7/2|\pm 7/2\rangle\Big)^2 = 0,$$

since whenever the left inner product of each term (corresponding to site 1) is non-zero (for instance, in the first term, when working with the upper sign), the right inner product (corresponding to site 2) is zero. Meanwhile the second term gives,

$$\frac{1}{2}\Big(\langle 7/2|\mathsf{J_{+1}}|\pm 7/2\rangle\langle -7/2|\pm 7/2\rangle - \langle -7/2|\mathsf{J_{+1}}|\pm 7/2\rangle\langle 7/2|\pm 7/2\rangle\Big)^2 = 0,$$

since the raising operator does not connect $|-7/2\rangle$ to $|7/2\rangle$. All other terms behave similarly. Meanwhile, by similar arguments, one can see that the intensity for the transition from $\psi_{0,0}$ to $\psi_{1,0}$ is non-zero so long as there is a non-zero overlap of $\langle\pm|\mathsf{J_z}|\pm\rangle$, which is generally expected to be true except in some "accidental" cases where $\sum_{M_J} M_J|C_{M_J}|^2$ sums to zero.

The Kramer's doublet composition for $Yb_2Si_2O_7$ is currently unknown. Based on the reasoning presented here and our observation of INS intensity only in the $\psi_{1,0}$ mode, we anticipate that the doublet has relatively weak matrix elements for the raising and lowering operators (e.g. $\langle -|\mathsf{J_+}|+\rangle$) compared to $\langle\pm|\mathsf{J_z}|\pm\rangle$. However, the g-values inferred based on (nearly) saturated magnetization at $H = 5$T ($g_a* = 3.2$, $g_b = 2.0$, $g_c = 4.8$) are not strictly Ising-like, implying there are *non-zero* matrix elements $\langle -|\mathsf{J_\pm}|+\rangle$.

A.3 Specific Heat Fitting

Modelling the specific heat arising from the excitation of triplons with dispersion relation $\epsilon(k)$ is a fairly non-trivial problem. In the very low-temperature limit, this can be accomplished [113] simply by considering a model of non-interaction Bosons, giving

$$C_m(T) = k_B\beta^2 \sum_{\boldsymbol{k},\alpha} [\epsilon_\alpha(\boldsymbol{k})]^2 \frac{e^{\beta\epsilon_\alpha(\boldsymbol{k})}}{[e^{\beta\epsilon(\boldsymbol{k})}-1]^2}. \tag{A.1}$$

As this expression neglects the fact that triplons are hard-core Bosons and interactions must be taken into account, it is not applicable at temperatures approaching the gap energy and higher. To fit the specific heat from low temperature to above the triplon band, one can instead estimate the appropriate specific heat with the following expression,

$$C_{\mathrm{m}}(T) = \frac{\beta^2}{2}\left[\frac{\sum_{\alpha,\boldsymbol{k}}[\epsilon_\alpha(\boldsymbol{k})]^2 e^{-\beta\epsilon_\alpha(\boldsymbol{k})}/\Omega}{1+\sum_{\alpha,\boldsymbol{k}} e^{-\beta\epsilon_{\alpha\boldsymbol{k}}}/\Omega} - \left(\frac{\sum_{\alpha,\boldsymbol{k}} \epsilon_\alpha(\boldsymbol{k}) e^{-\beta\epsilon_\alpha(\boldsymbol{k})}/\Omega}{1+\sum_{\alpha,\boldsymbol{k}} e^{-\beta\epsilon_\alpha(\boldsymbol{k})}/\Omega}\right)^2\right] \tag{A.2}$$

which is taken from Refs. [114, 115]. The index α labels the three possible triplon bands and Ω is the volume of the Brillouin zone. In the case of Heisenberg interactions, the three triplon bands become degenerate in zero field, hence the expression can be simplified to

$$C_{\mathrm{m}}(T) = \frac{\beta^2}{2}\left[\frac{3\sum_{\boldsymbol{k}}[\epsilon(\boldsymbol{k})]^2 e^{-\beta\epsilon(\boldsymbol{k})}/\Omega}{1+3\sum_{\boldsymbol{k}} e^{-\beta\epsilon_{\boldsymbol{k}}}/\Omega} - \left(\frac{3\sum_{\boldsymbol{k}} \epsilon(\boldsymbol{k}) e^{-\beta\epsilon(\boldsymbol{k})}/\Omega}{1+3\sum_{\boldsymbol{k}} e^{-\beta\epsilon(\boldsymbol{k})}/\Omega}\right)^2\right] \tag{A.3}$$

In order to fit the data in Fig. 2a of the main document, we use the above expression and the following dispersion relation:

$$\epsilon(\boldsymbol{k}) = J_{\text{intra}} + 2J_{\text{inter}}\cos(k_x/2)\cos(k_y/2) \tag{A.4}$$

which fairly effectively reproduces the form of the triplon dispersion measured with inelastic neutron scattering in zero field. The fit of the data is very successful, indicating that fairly isotropic interactions can adequately describe the physics of this system. While slightly anisotropic interactions (which would lift the degeneracy of the triplon bands) could also fit the data, they are not necessary. The resulting exchange constants $J_{\text{intra}} = 0.236$ meV and $J_{\text{inter}} = 0.063$ meV are fairly close to the values obtained from the spin-wave analysis (J_{intra} = 0.217(3) meV and J_{inter} = 0.089(1) meV, see section on fitting the field polarized spinwaves below). In any case, we should not expect perfect agreement as this form of the specific heat is an approximation and assumes that the triplon dispersion is independent of temperature, which is unlikely to be true. Whereas the fitting of the specific heat data will primarily be affected by the shape of the dispersion at around 1 K (at the

specific heat maximum), the inelastic neutron scattering measurements were performed at much lower temperatures (50 mK).

A.4 Ultrasound Velocity Measurements

Sound velocity measurements were performed as a function of field applied along c^* at fixed temperature (as presented in the main text) and as a function of temperature at fixed field (as presented in Fig. SA.1). The ultrasound velocity experiments were performed down to 50 mK using a pulsed, time-of-flight interferometer. 30 MHz transducers were glued to parallel surfaces so as to propagate longitudinally polarized sound waves along the c^*-axis. The absolute velocity of the quasi-longitudinal mode studied here was approximately 3000 m/s and relative changes in velocity ($\Delta v/v$) were measured with high precision using a phase-lock loop. Antiferromagnetic phase boundaries could be determined at low temperatures (below 150 mK) from the field sweeps by selecting a sharp change in slope (H_{c1}) and a minimum in sound velocity (H_{c2}). As the temperature is raised, these anomalies are significantly broadened and it becomes impossible to determine phase boundaries from the field sweeps. The top of the antiferromagnetic "dome" was thus determined from small anomalies (abrupt changes in slope) in the temperature sweeps shown in Fig. SA.1. These anomalies are entirely consistent with the peaks found in low-temperature specific heat measurements.

The inset of Fig. 4c in the main text shows a comparison of the sound velocity field sweep with the field-derivative of the neutron Bragg intensity, dI/dB, which is proportional to $d(m_z^2)/dB = 2m_z\chi$. The agreement is excellent and this suggests that the sound velocity is well coupled to the uniform longitudinal magnetization. However, a standard theoretical treatment gives a somewhat different relationship between magnetization and sound velocity. Assuming a linear-quadratic magnetoelastic coupling term in the free energy

$$F_{me} = \frac{1}{2}\kappa\epsilon_n m_z^2$$

where κ is a magnetoelastic coupling constant related to a particular element of the strain tensor, ϵ_n. Following the work of Quirion *et al.* [116], amongst others, the elastic constant is renormalized as

$$C_{mn} = \frac{\partial^2 F}{\partial \epsilon_m \partial \epsilon_n} - \frac{\partial^2 F}{\partial m_z \partial \epsilon_m} \left(\frac{\partial^2 F}{\partial m_z^2} \right)^{-1} \frac{\partial^2 F}{\partial m_z \partial \epsilon_n}$$

For the particular mode studied here,

$$C_{33} = C_{33}^0 - \left(\frac{\partial^2 F}{\partial m_z \partial \epsilon_3} \right)^2 \left(\frac{\partial^2 F}{\partial m_z^2} \right)^{-1}$$

$$C_{33} = C_{33}^0 - (2\kappa m_z)^2 a^{-1} = C_{33}^0 - \kappa^2 m_z^2 \chi_z$$

Relative changes in sound velocity can then be related to relative changes in elastic constant through

$$\frac{\Delta v}{v} = \frac{\Delta C_{33}}{2C_{33}^0} = -\frac{\kappa^2 m_z^2 \chi}{2C_{33}^0}$$

There are thus two striking differences between this simple theory and the results. 1. As mentioned above, experimentally $\Delta v/v \propto |m|\chi$ whereas the theory predicts $\Delta v/v \propto m^2\chi$. As such, the dip at H_{c2} is less pronounced experimentally than theoretically. 2. The area under the curve $\int_0^{B_{\text{sat.}}} (\Delta v/v) dB$, which according to theory should simply give $m_{\text{sat.}}^3$, is in reality strongly temperature dependent. Hence, in the future, a more elaborate theoretical treatment of sound velocity for such a system, including coupling to the antiferromagnetic order parameter and spin fluctuations, would be valuable and might provide a more quantitative understanding of these results.

A.5 Single Crystal Neutron Scattering

Five single crystals were co-aligned using Laue X-ray scattering to achieve an overall mass of 1.1 g and a mosaic spread of less than 3° of the dominant grain. The crystal mount is shown in Fig. SA.2. One of the crystals was later discovered to contain a misaligned grain, which is visible in the neutron scattering data. The elastic scattering (-0.1 meV to 0.1 meV) shows Bragg peaks from the misaligned grain, highlighted by red circles in Fig. SA.3. Figure SA.4 shows inelastic slices for

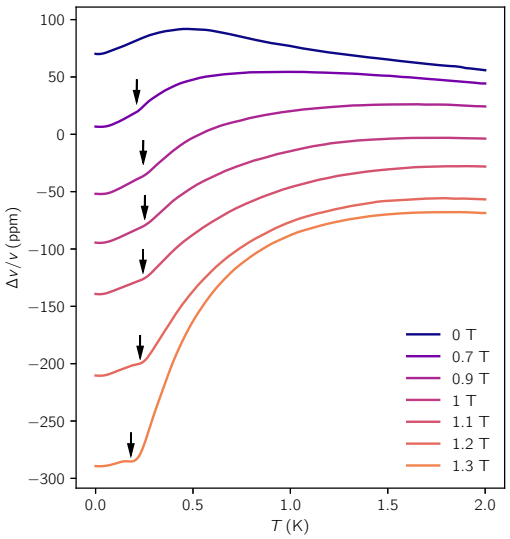

Figure A.1: Ultrasound velocity measurements as a function of temperature at constant magnetic field. Arrows indicate anomalies associated with antiferromagnetic ordering.

every applied magnetic field setting ($H||c$). The path through reciprocal space shown in these plots is illustrated to the right of the figure. At low fields, the presence of the misaligned grain is clearly observed, manifesting as what looks like an additional excitation branch in portions of the HK0 plane. It is particularly prevalent at ($\overline{0.1}$,$\overline{1}$,0) and ($\overline{1}$,$\overline{1}$,0). The excitations of this misaligned grain are not visible for fields greater than 1.25 T. This may be due to the overall decrease in inelastic intensity which occurs due to the development of strong magnetic Bragg peaks. Additionally, for field values near H_{c1} the $S_z = \pm 1$ modes (which we have called $\psi_{1,\pm 1}$ above) are (barely) visible near the ($\overline{1}$,1,0) reciprocal lattice point (also shown in Fig. S6 as line cuts). This indicates that the aforementioned transition matrix elements from the ground state to the $\psi_{1,\pm 1}$ states are small but non-zero.

Figure A.2: The coalignment of five crystals used for the inelastic neutron scattering measurement.

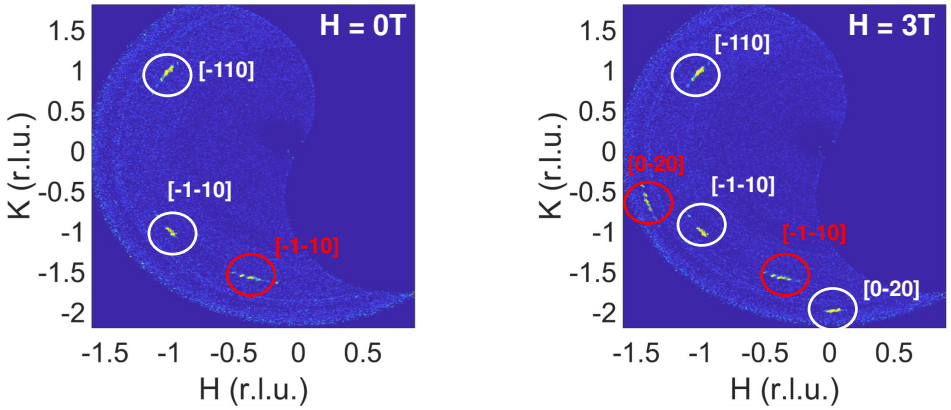

Figure A.3: Slices taken at the elastic line (integrated from $E = -0.1$ to 0.1 meV) with E_i = 1.55 meV. Bragg peaks (both nuclear and magnetic in origin) arising from the main grain are labeled in white. Bragg peaks from the misaligned grain are circled in red. The HKL values for reflections from the misaligned grain were determined based on their 2θ values.

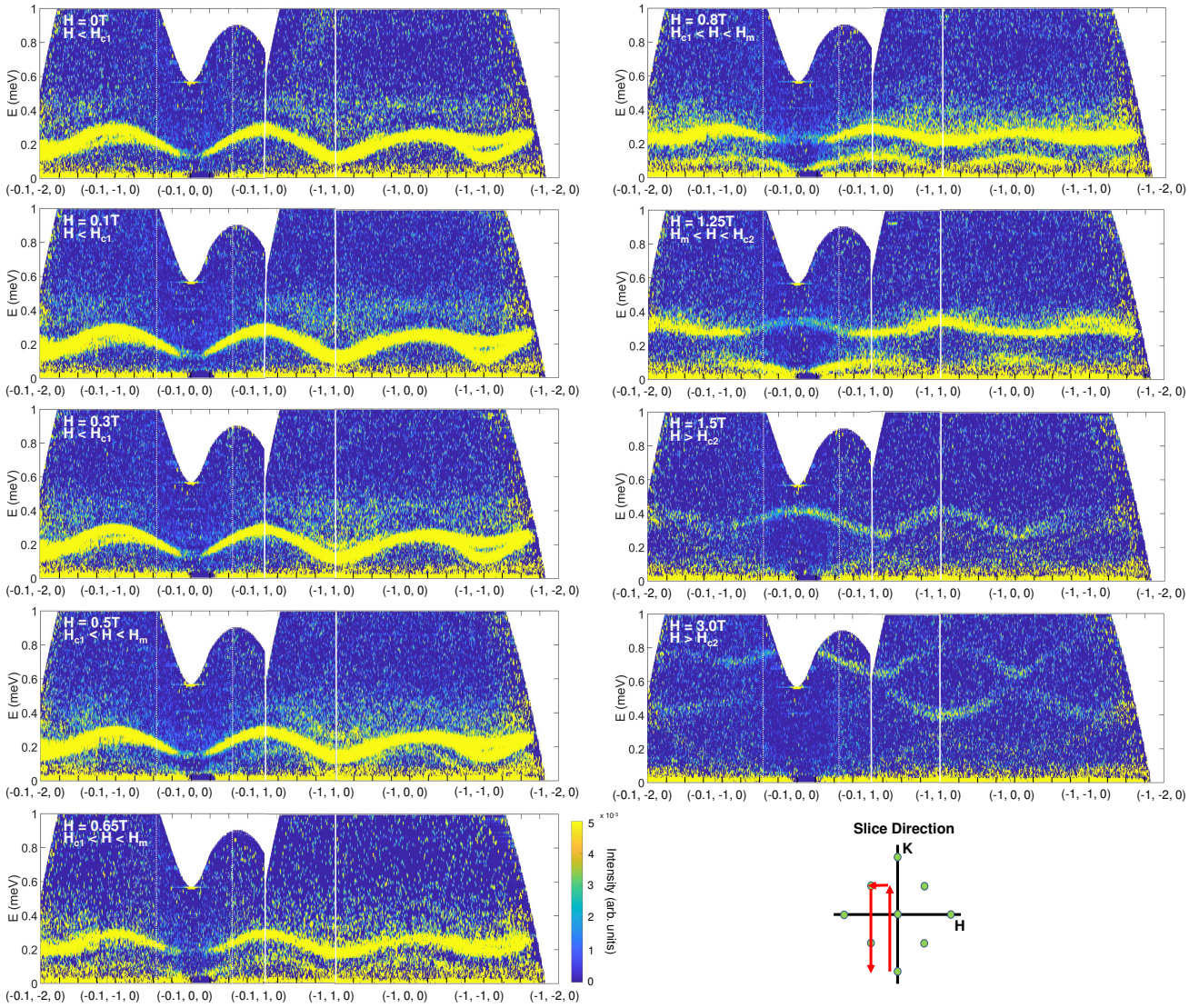

Figure A.4: INS data at 50mK shown for an "open-rectangular" path of reciprocal space (shown in the bottom right of the figure), for all the magnetic field strengths measured.

Fig. SA.5 shows line cuts taken at $|Q| = 0.2362$ Å^{-1} for all the measured field strengths. The primary excitation ($\psi_{1,0}$) does not change in energy below H_{c1} indicating its angular momentum projection along the magnetic field is 0. Thus we conclude that this excitation is the excitation to the $S_{tot} = 0$, $S_z = 0$ mode. Additionally, the development of the branch connected to the Goldstone mode is visible at ~ 0.08 meV and is only observed for fields between H_{c1} and H_{c2}.

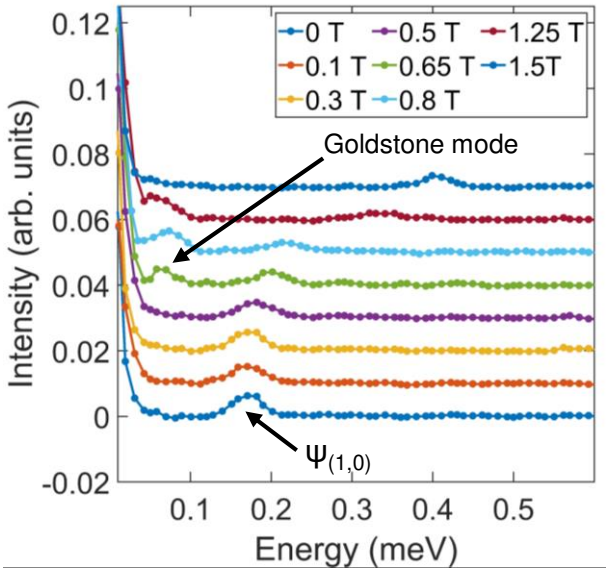

Figure A.5: Intensity vs. energy cuts of the inelastic neutron spectrum at $|Q| = 0.2362$ Å^{-1}. The excitation branch *leading* to the Goldstone mode is visible as a low energy peak between H_{c1} (0.4 T) and H_{c2} (1.4 T). Below H_{c1}, the peak near 0.19 meV remains at constant energy, identifying it as a $S_z = 0$ excitation (ψ_0)

Fig. SA.6 shows line cuts on a logarithmic intensity scale, taken at $(\bar{1}, 1, 0)$ for three different magnetic field strengths: 0.3 T, 0.5 T, and 3 T. The 3 T data is shown as a reference to what the expected background would be for this energy range. At 0.3 T and 0.5 T the main $\psi_{1,0}$ excitation is observed at ~ 0.12 meV and ~ 0.14 meV, respectively. At H = 0.3T and 0.5T, two weak excitations are seen to split off of the main line, which can likely be identified as the $\psi_{1,\pm1}$ states. The weak intensity of these modes is likely due to the effect of the crystal electric field on the matrix elements for the transitions, as discussed above.

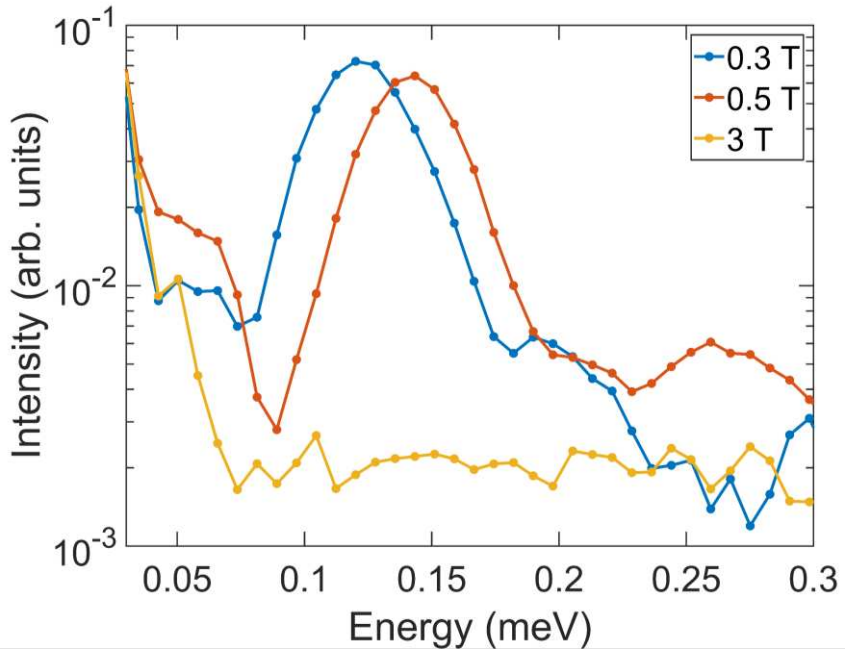

Figure A.6: Cuts of the inelastic neutron spectrum at (-1, 1, 0), integrating over H = [-1.1,-0.9] and K = [0.75,1.25] r.l.u. for three different magnetic field strengths. The sharp large peaks in 0.3 T and 0.5 T are the S_z = 0 mode observed at all field values. On the lower and higher energy sides of this peak additional features from the $S_z = \pm 1$ modes are observed.

A.6 Fits to Field-Polarized Spin Waves

The spin wave dispersions measured in the field-polarized limit ($H = 3$T) were fit using linear spin wave theory (LSWT) as implemented by the SpinW package [117], which evaluates the goodness of fit based on agreement between the measured and calculated dispersions (and does not include comparisons of intensities). Several types of fits were attempted, as described further below. Each fit was performed using the "particle swarm optimizer" algorithm for 10 runs with 100 iterations per run, and a maximum number of function evaluations of 1×10^5. The outputs for each fit are shown in Table A.1.

The magnetic structure was optimized for each new set of trial parameters (our addition to the pre-existing SpinW fitting routine). The reference frame chosen by SpinW is $x = a$, $y = b$, and $z = c^*$, so for our fits involving an XXZ form of the interaction Hamiltonian (where we have assume

Table A.1: Parameters from the various types of fits (and comparing to the result of fitting the zero field C_p). The quoted error for the parameters extracted from spin wave fits is from the standard deviation of the respective parameters in the 10 runs.

	Unconstrained Heisenberg	Constrained Heisenberg	XXZ/Heisenberg	Specific Heat
J_{intra} (meV)	0.18(2)	0.217(3)	$J_{\text{intra, XX}}$ = 0.190(3), $J_{\text{intra, Z}}$ = 0.180(4)	0.236(4)
J_{inter} (meV)	0.12(1)	0.089(1)	0.121(1)	0.06(2)
g_{zz}	4.82(5)	4.68(1)	4.8 (fixed)	N/A

$z = c$, i.e. the field direction, which we call the "experimental coordinate frame"), we performed a coordinate transformation on the XXZ exchange matrix and constrained the variation of the resulting (non-diagonal) matrix elements to ensure XXZ symmetry in the experimental frame. **All of our exchange parameters and symmetries mentioned below and in the main text are with respect to the a^*, b, c basis, i.e., the experimental frame.** Fits were performed with data taken from the following slices: (-1K0), (H00), (H10), (-HH0), (H-2H0), and (-0.1K0). The spin waves were fit to the Hamiltonian below:

$$H = \sum_{<i,j>} \boldsymbol{S_i}\ \bar{J}_{\text{intra}} \boldsymbol{S_j} + \sum_{<<i,j>>} \boldsymbol{S_i}\ \bar{J}_{\text{inter}} \boldsymbol{S_j} + \sum_i \boldsymbol{B}\ \bar{g}\ \boldsymbol{S_i}$$

where $\bar{J}_{\text{intra}}$ and $\bar{J}_{\text{inter}}$ are the intra- and interdimer exchange interaction tensors as labeled in Fig. 1a of the main text, and $\bar{g}$ denotes the g-tensor. For the two exchange tensors, the lowest possible symmetry is (based on the space group symmetries):

$$\bar{J}_{\text{intra}} = \begin{bmatrix} A_1 & 0 & D_1 \\ 0 & B_1 & 0 \\ D_1 & 0 & C_1 \end{bmatrix}$$

$$\bar{J}_{\text{inter}} = \begin{bmatrix} A_2 & E & D_2 \\ E & B_2 & F \\ D_2 & F & C_2 \end{bmatrix}$$

Using these full symmetry-allowed forms would constitute fitting 10 independent parameters, which for our data set is infeasible. Therefore, we started with the lowest possible symmetry that one would expect given the observation of a Goldstone mode with the field applied along the c-axis, which is an XXZ type interaction. However, we did not fit $\bar{J}_{\text{inter}}$ as XXZ due to a direct correlation between $J_{\text{intra, Z}}$ and $J_{\text{inter, Z}}$. With this in consideration, we fit the exchange interactions as XXZ for J_{intra} and Heisenberg for J_{inter} shown in Fig. SA.7. The extracted parameters are: $J_{\text{intra, XX}}$ = $0.190(3)$ meV, $J_{\text{intra, Z}}$ = $0.180(4)$ meV, and J_{inter} = $0.121(1)$ meV. Additionally, we would like to remind the reader that we are using the convention of positive J meaning antiferromagnetic exchange. This fit shows good qualitative agreement, however, along certain directions (such as (H00), (H10), and (-0.1K0)) it fails to reproduce some intensity features. Additionally, the shape of the dispersions do not exactly match, which is particularly evident along (H00) and (-0.1,K,0). The reason for this disagreement is uncertain, but suggests that weaker in-plane anisotropies are responsible.

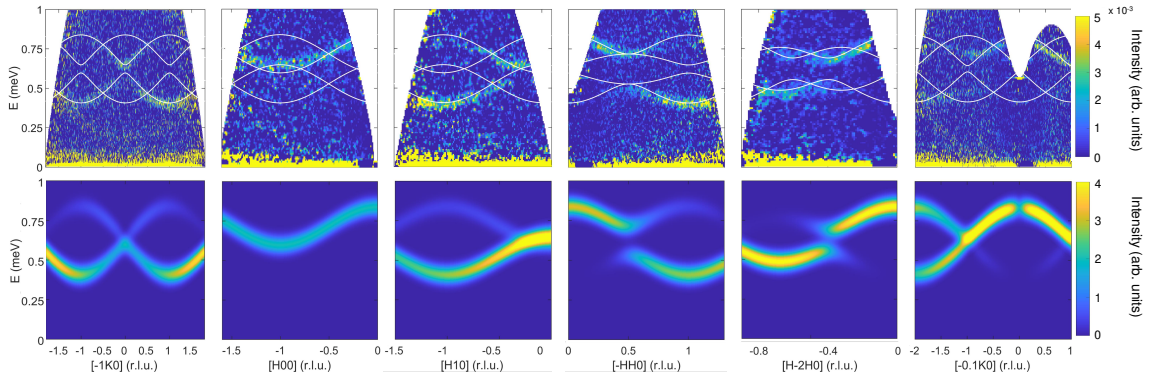

Figure A.7: (top row) Overlays of dispersion on the inelastic neutron scattering data using the J_{intra} XXZ and J_{inter} Heisenberg fit parameters. The extracted parameters from this fit are: $J_{\text{intra, XX}}$ = $0.190(3)$ meV, $J_{\text{intra, Z}}$ = $0.180(4)$ meV, and J_{inter} = $0.121(1)$ meV. There are four bands due to having 4 magnetic atoms in the unit cell of $Yb_2Si_2O_7$. (bottom row) Calculated neutron spectra for the same set of parameters.

We also include fits for Heisenberg symmetry on both J_{intra} and J_{inter}. In these fits we also let the z component of the g-tensor g_c vary ± 0.5 from the value we infer from magnetization measurements (4.8). The extracted parameters from the fit shown in Fig. SA.8 are: J_{intra} = $0.18(2)$

meV, $J_{\text{inter}} = 0.12(1)$ meV, and $g_c = 4.82(5)$. Visually, the Heisenberg fit produces similar results to the XXZ fit, which is as expected since the intensities and dispersions of the in-plane (HK0) spin waves should be determined by the in-plane interactions only (the z exchange acts like g_c and serves only to shift the bands up and down).

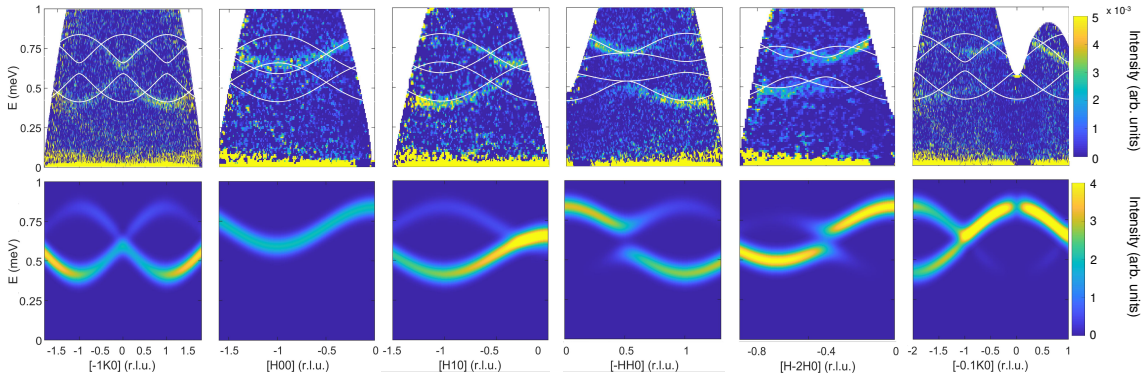

Figure A.8: (top row) Overlays of dispersion on the inelastic neutron scattering data using the J_{intra} Heisenberg and J_{inter} Heisenberg fit parameters. The extracted parameters from this fit are: $J_{\text{intra}} = 0.18(2)$ meV, $J_{\text{inter}} = 0.12(1)$ meV, and $g_c = 4.82(5)$. There are four bands due to having 4 magnetic atoms in the unit cell of $Yb_2Si_2O_7$. (bottom row) Calculated neutron spectra for the same set of parameters.

Considering qualitative agreement with the measured intensities (rather than just the dispersion relations), we found that Heisenberg parameters constrained in the following way could provide a better agreement: J_{intra} constrained between 0.18 and 0.3 while J_{inter} was constrained between 0 and 0.1. This range was roughly determined by manually adjusting the parameters and observing how the intensities of the spectra changed. The parameters from this constrained fit are: $J_{\text{intra}} = 0.217(3)$ meV, $J_{\text{inter}} = 0.089(1)$ meV, and $g_c = 4.68(1)$. This was the most consistent fit we obtained considering both dispersions and intensities. These constrained fits are shown in Fig. SA.9 below. While the same issues exist regarding the agreement of dispersion relations for (H,0,0) and (-0.1,K,0) directions, the intensity of trade-off between the upper and lower branches along (-1,K,0) is captured better. In the main text we have adopted these parameters obtained from this version of the fit.

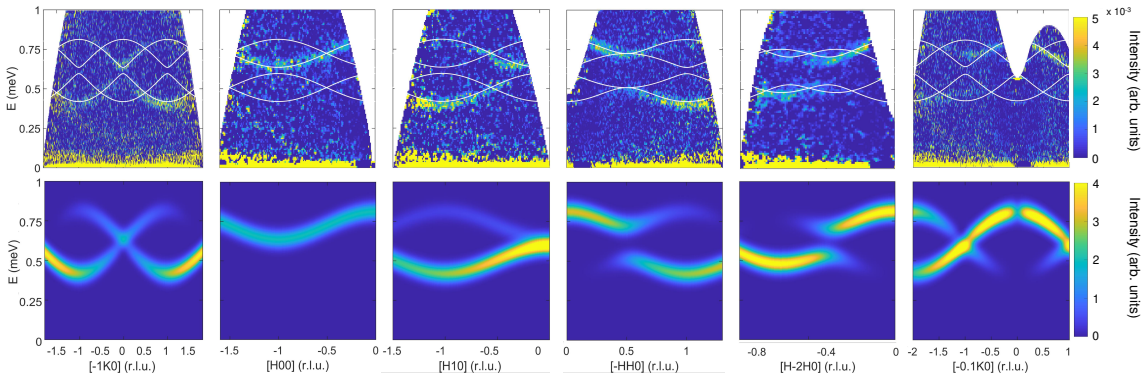

Figure A.9: (top row) Overlays of dispersion on the inelastic neutron scattering data using the J_{intra} Heisenberg and J_{inter} Heisenberg fit parameters that were constrained in fitting. The parameters from this fit are: $J_{\text{intra}} = 0.217(3)$ meV, $J_{\text{inter}} = 0.089(1)$ meV, and $g_c = 4.68(1)$. There are four bands due to having 4 magnetic atoms in the unit cell of $Yb_2Si_2O_7$. (bottom row) Calculated neutron spectra for the same set of parameters.

In addition to the aforementioned improvements, the fit from Fig. SA.9 also provides a more realistic H_{c1} value if an isolated dimer model is considered. The calculation of the isolated dimer model triplet splitting is shown in Fig. SA.10, where the lower band and upper band lines are determined from the measured dispersion of the H = 0 T spin wave excitation (see main text).

A.7 Powder Neutron Diffraction

Neutron powder diffraction data (taken on the instrument BT1 at the NIST Center for Neutron Research) confirms a lack of long range magnetic order in zero applied field. No magnetic Bragg peaks are observed at 300 mK (see the high vs. low temperature difference plot in Fig. SA.11).

A.8 Powder Synchotron X-Ray Diffraction

Synchrotron X-ray powder diffraction was performed using the Advanced Photon Source at Argonne National Laboratory using the 11-BM beamline with λ = 0.4122Å. Rietveld refinement of the data agrees well with the previously published structure of $Yb_2Si_2O_7$ [17]. Refined structural parameters at 295 K are listed in Table A.2.

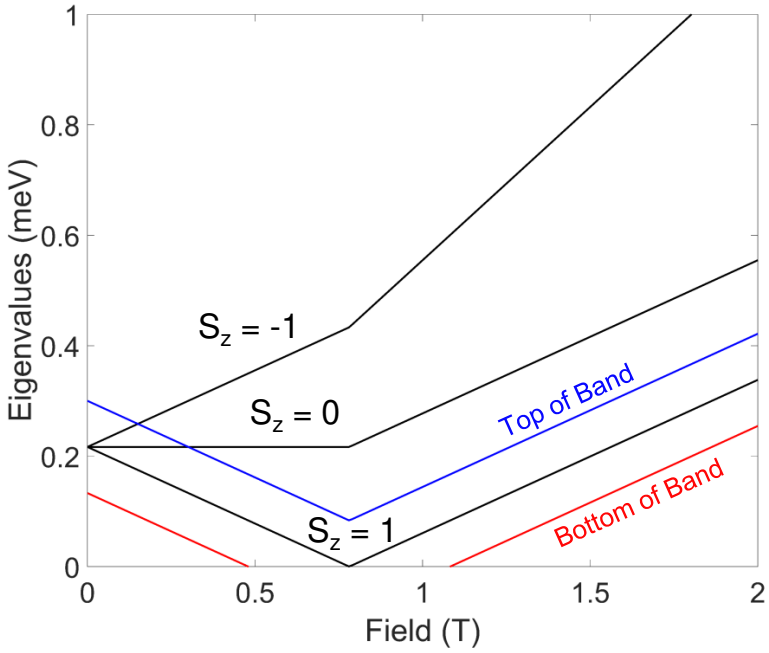

Figure A.10: Calculation of the eigenvalues of the triplet modes with an isolated dimer model using the parameters from the constrained Heisenberg fit (Fig. SA.9). The upper and lower bound of the $S_Z = 1$ mode are shown using the bandwidth determined experimentally, as in this model they determine H_{c1} and H_{c2}.

Table A.2: Structural parameters at 295 K. Space group C2/m, a = 6.7714(9), b = 8.8394(2), c = 4.6896(5), β = 101.984(9).

Atom	Site	x	y	z
Yb	$4g$	0.5	0.8066(8)	0
Si	$4i$	0.7184(4)	0.5	0.4137(6)
O	$2c$	0.5	0.5	0.5
O	$4i$	0.8804(7)	0.5	0.7215(9)
O	$8j$	0.7362(8)	0.6510(8)	0.2160(4)

A.9 Magnetization

Magnetization was measured at 1.8 K using a Quantum Design SQUID magnetometer, shown in Fig. SA.13. Proper orientation of the crystal was confirmed before and after measurements using Laue x-ray diffraction.

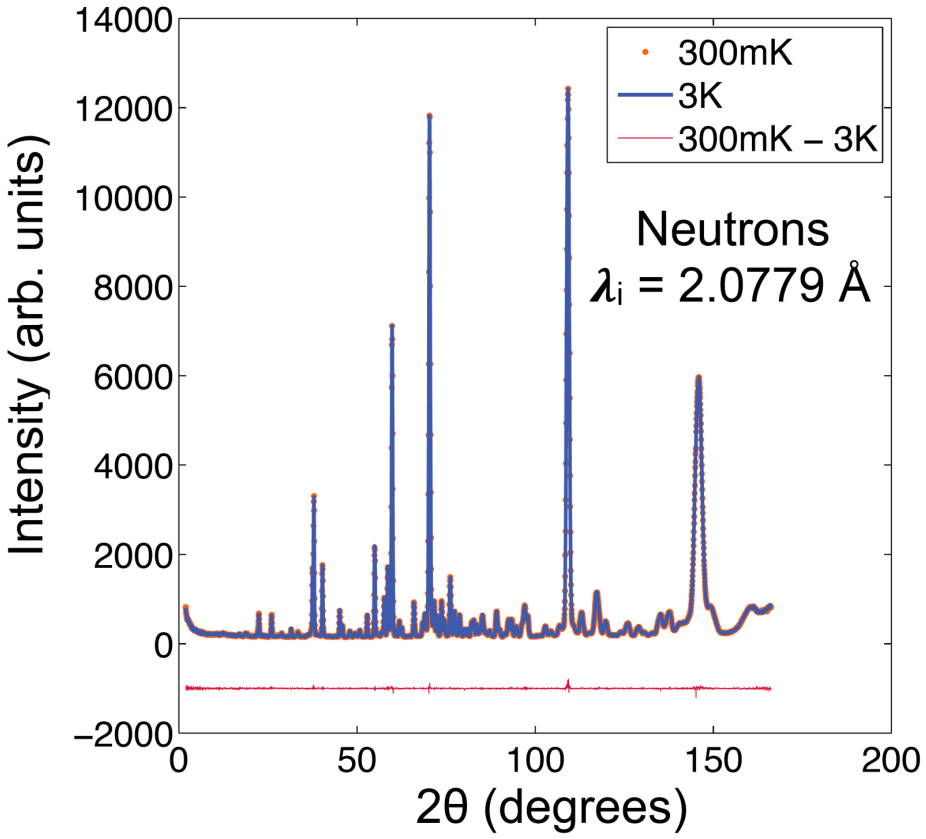

Figure A.11: Powder neutron diffraction data taken at 300 mK and 3 K. No additional Bragg peaks are observed at 300 mK confirming the non-magnetic singlet ground state.

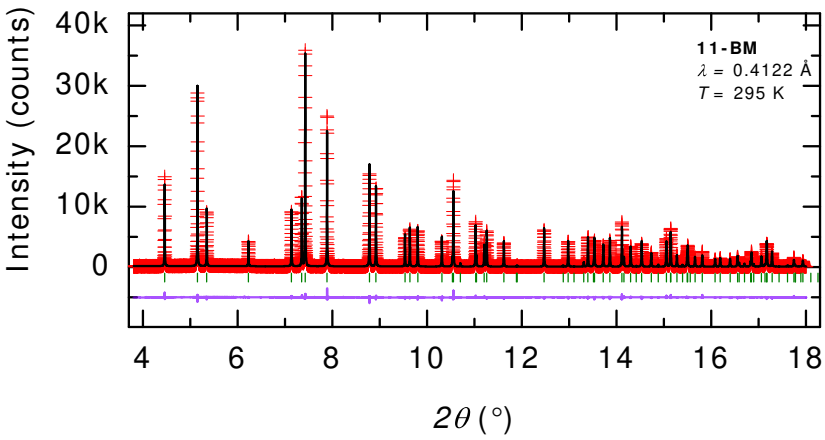

Figure A.12: Synchrotron X-ray diffraction data measured on polycrystalline $Yb_2Si_2O_7$ at 295 K (red data points), with structural refinement (black line) and difference curve (purple line) shown.

A.10 High-Temperature Specific Heat

The magnetic specific heat of a polycrystalline sample of $Yb_2Si_2O_7$ was found by subtracting the specific heat of $Lu_2Si_2O_7$ (the non-magnetic lattice analog), and is shown in Fig. SA.14. The

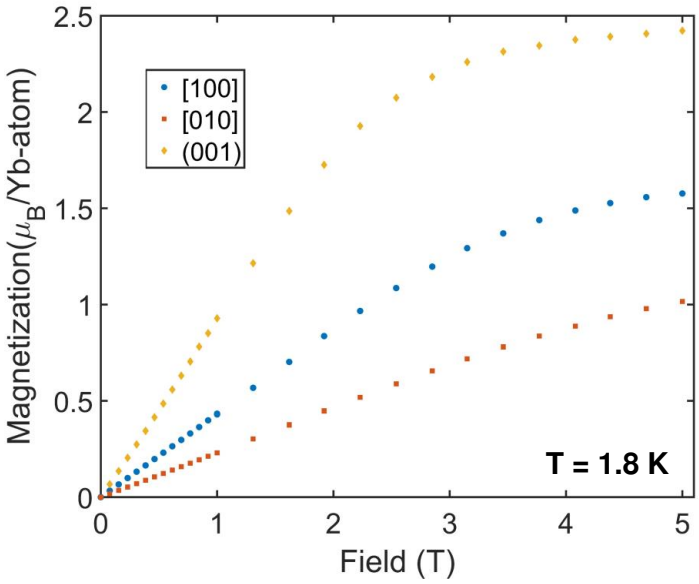

Figure A.13: Magnetization performed at 1.8 K along a^*, b^*, and c yields the g-tensor values shown in the main text, $g_{a*} = 3.2$, $g_{b*} = 2.0$, and $g_c = 4.8$.

data shows the field dependence of the low-temperature Schottky anomaly, and also show the beginnings of a separate Schottky anomaly (upturn after 10 K) signaling the presence of a crystal field level at approximately 120 K. The 0T data was reproduced at both Colorado State University (using a Quantum Design Physical Properties Measurement System) and Université de Sherbrooke.

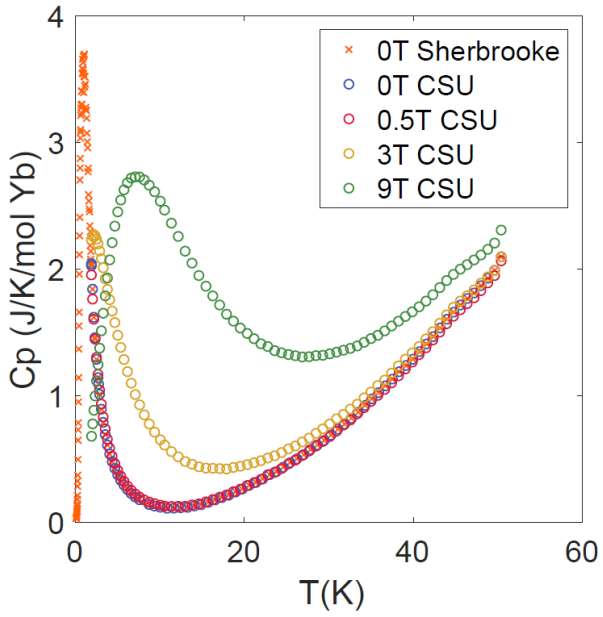

Figure A.14: Field-dependent magnetic specific heat (lattice subtracted) from a polycrystalline sample.

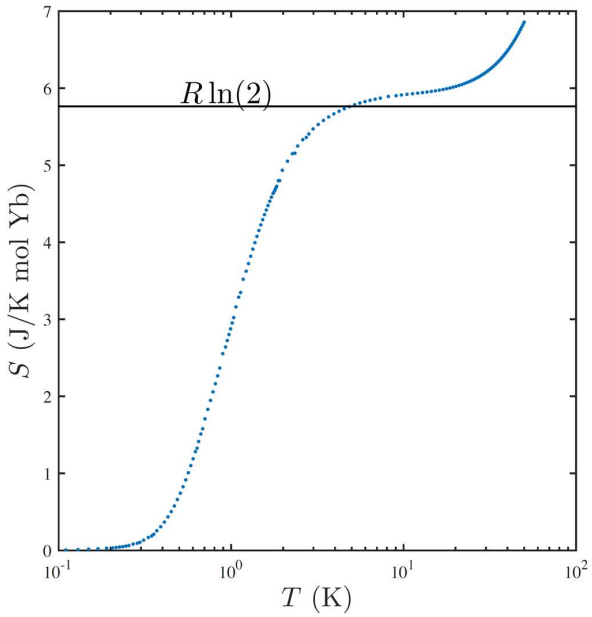

Figure A.15: Magnetic entropy extracted from the 0T specific heat measurement. The entropy reaches Rln2 per Yb between 50 mK and 5 K, indicating a low temperature effective spin-1/2.

A.11 Erratum

In the original version of this paper, we presented heat capacity data for numerous magnetic field strengths (Fig. 3.2), however, inconsistencies encountered with measurements on different compounds warranted checking the data presented for $Yb_2Si_2O_7$. It was found that some of the heat pulse fits for the low temperature measurements at 0.5 T, 0.8 T, and 1.2 T were incorrect, likely due to not enough grease being used when mounting the crystal. A lack of grease can limit the thermal conductivity from the platform to the sample, causing heat pulses that do not represent the heat capacity of the sample. This is corroborated by a comparison of the original 0.5 T data and the 0.5 T data with the pulses checked in Fig. A.16a, as the heat capacity matches well at higher temperatures (above $\sim$0.3 K), but at low temperature - where the heat capacity is naturally lower and the thermal conductivity becomes more important - the heat capacity values are quite different. Subsequently, we have examined every pulse presented in the main text - except at 0 T - to look for bad fits, similar to the one shown in Fig. A.16a. The 0 T data was measured by collaborators at the Université de Sherbrooke on a different system, therefore the raw pulses were not available to analyze. Removing the data with bad fits and adding 0.5 T data that was not included when the paper was published yields an updated version of the figure shown in Fig. A.17 . Experiments to remeasure the rest of the missing data are currently planned, but the measurements are not available at the time of writing. The missing data does not significantly affect our conclusions on the quantum dimer magnet ground state of $Yb_2Si_2O_7$. The value for H_{c1} presented in the paper was obtained from an ultrasound velocity measurement at 0.05 K, so it is unlikely that H_{c1} will change, but it is possible that the shape of the dome in the field-temperature phase diagram will change slightly. The unknown phase in the field-temperature phase diagram should persist, as there are still no sharp peaks in the 1.3 T data, indicating that the field polarized paramagnetic state is still continuously connected to the unknown state in the high field regime of the BEC dome. Overall, this error may change the shape of the dome in the field-temperature phase diagram, but it does not significantly affect our main conclusions that $Yb_2Si_2O_7$ exhibits a ground-state quantum dimer

The pulses for the added 0.5 T data were checked as well.

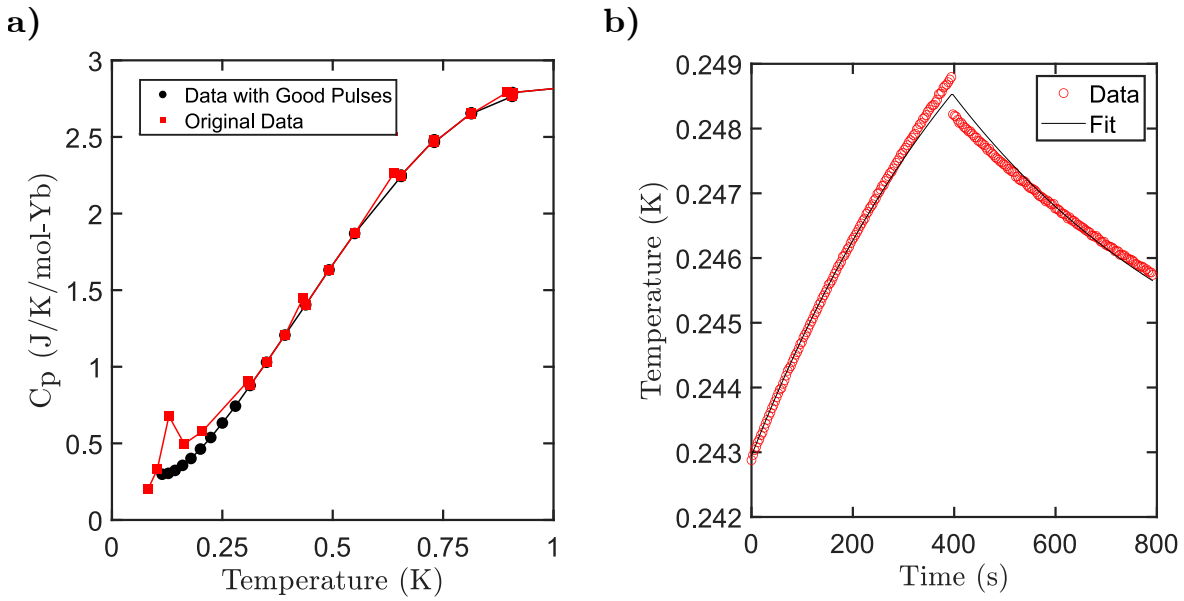

Figure A.16: a) A comparison of the 0.5 T specific heat data with verified good pulses (black) and the original data (red) presented in the manuscript. The specific heat peak at 0.130 K for the 0.5 T data no longer appears when the bad pulses are removed, indicating it was an artifact of the lack of thermal grease. b) An example of a bad fit to the heating-cooling curve measured by the Quantum Design Dilution Insert system. This fit is utilized to extract the specific heat values shown in panel b.

magnet state with field-induced signatures similar to that of traditional $3d$ transition metal BEC compounds.

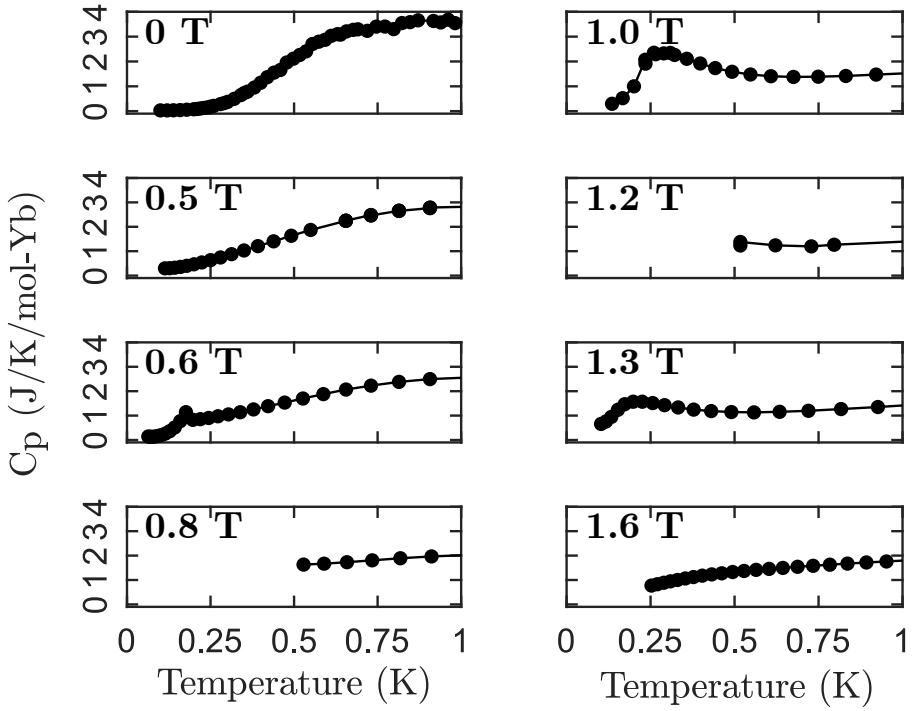

Figure A.17: Reproduction of the specific heat figure shown in Fig. 3.2, but only showing data where the pulses have been verified, aside from the 0 T data which was measured on a different experimental setup.

A.12 Additional Data

A.12.1 $Yb_2Si_2O_7$: Preliminary b-axis Heat Capacity Measurements

Measurements of the field-dependent specific heat for $Yb_2Si_2O_7$ with the magnetic field applied along the crystallographic b-axis were performed using the quasi-adiabatic and the "long pulse" measurement method. The former technique is outlined in Chapter 2.2.2. The latter method - the "long pulse" method - applies a large heat pulse (a temperature rise of 200% is not uncommon) to the sample and the temperature is measured as the sample cools back to the platform temperature (shown in the inset of Fig. A.18a). The derivative of this temperature versus time graph can then be computed to determine the heat capacity [118], resulting in a specific heat curve that looks similar to the one shown in Fig. A.18a. To analyze the long pulse data, short pulse data is also needed, but only a few measurements. This technique greatly improves the efficiency for measuring very sharp transitions, i.e. transitions with significant latent heat - enabling the measurement of more variations of an experimental parameter, such as magnetic field. Using this technique, preliminary specific heat data were obtained with the field along the b-axis of $Yb_2Si_2O_7$ and is shown in Fig. A.18b. The lower critical field, H_{c1}, for a field along the b-axis is approximately 1 T based on this data. This is larger than the first critical field for the field along the c-axis (0.4 T) due to the smaller g-tensor value along the b-axis. This data is not clear as to if the dome is asymmetric, but it may be that the field being applied along the b-axis realizes a dome closer to those of the traditional $3d$ BEC compounds.

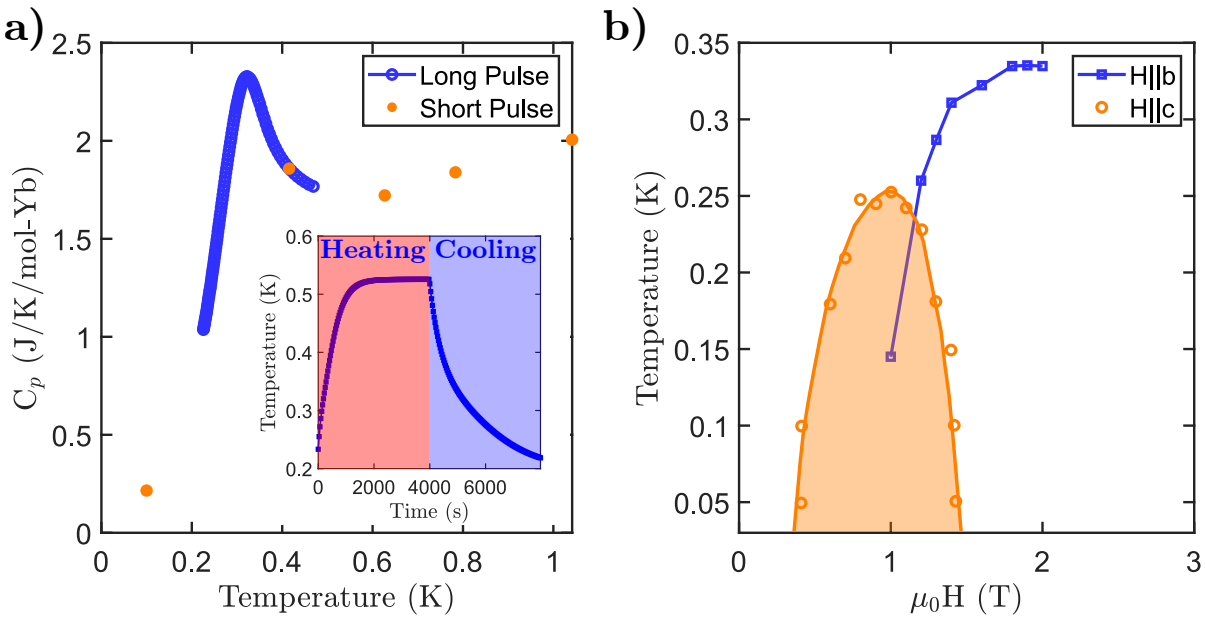

Figure A.18: a) Characteristic long pulse curve (blue) measured on $Yb_2Si_2O_7$ with a 1.6 T field applied along the *b* axis. The short pulse data needed to calibrate the long pulse data is also shown in orange. (inset) A plot of the heat pulse used to extract the spcific heat in panel a. b) Preliminary data (blue) showing the evolution of the specific heat peak in temperature and magnetic field for a magnetic field applied along the *b*-axis of $Yb_2Si_2O_7$. The data for the phase diagram for a field along the *c*-axis is shown in orange.

Appendix B

Supplemental Information on D-$Er_2Si_2O_7$

B.1 Heat Capacity Measurements

The heat capacity for 1.8 K to 100 K is shown in Fig. B.1. A broad feature on top of the phonon contribution is observed. The peak of this feature occurs at $\sim$ 16 K and can be attributed to a crystal field Schottky anomaly around 39 K, consistent with the lowest crystal electric field level measured by Leask *et. al.* at 27 cm^{-1} (39 K) [2].

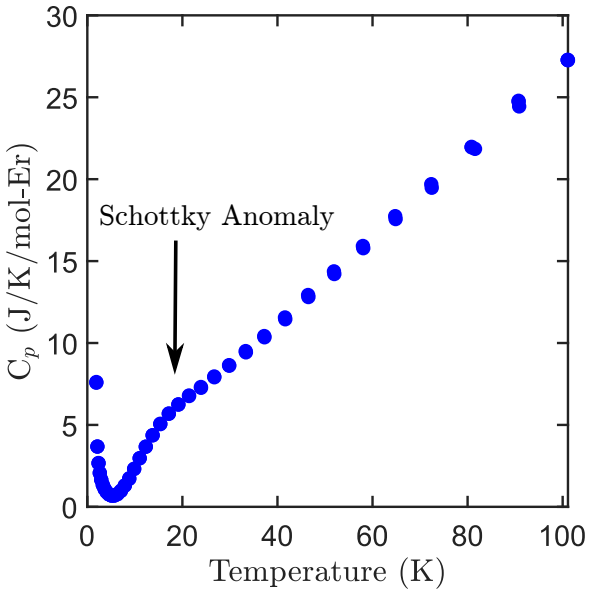

Figure B.1: Specific heat measured on a powder sample of D-$Er_2Si_2O_7$.

B.2 Magnetic Structure Refinement

Additional neutron diffraction data obtained on a powder sample of D-$Er_2Si_2O_7$ is shown in Fig. B.2. The data at 10 K (Fig. B.2a) was used to perform a Rietveld refinement on the nuclear structure of D-$Er_2Si_2O_7$ with the Cu peaks masked. This yielded the following lattice parameters

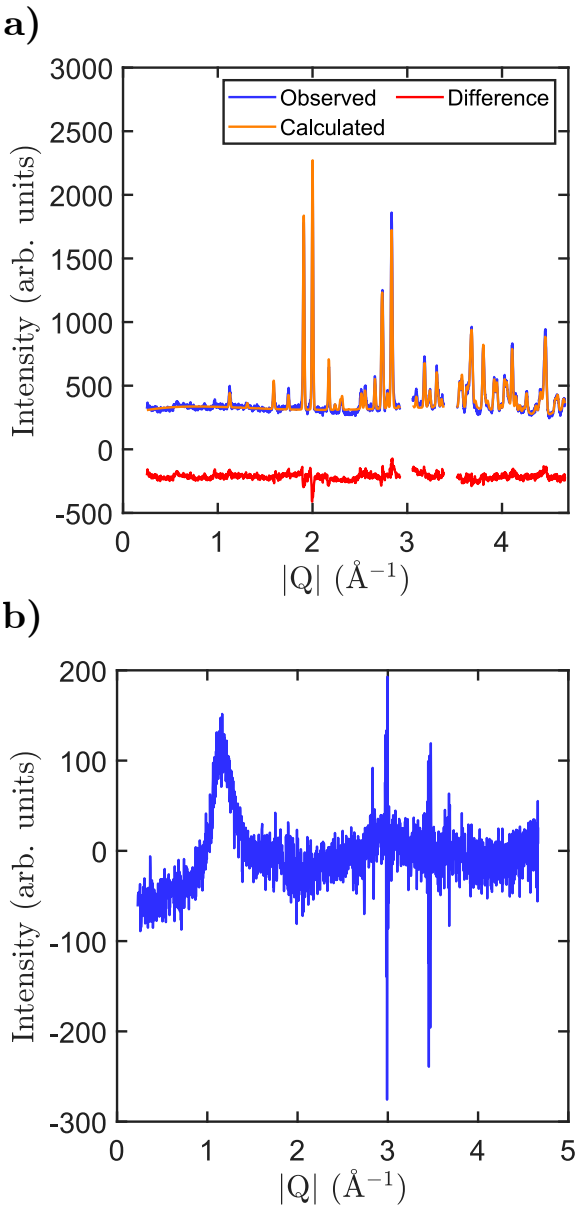

Figure B.2: a) Neutron diffraction data obtained using HB-2A at 10 K. The fit was performed after removing peaks from the Cu canister. b) Neutron diffraction data obtained using HB-2A with the 10 K data subtracted from the 2 K data showing the diffuse scattering expected in the vicinity of a second order phase transition, with a peak centered at 1.2 Å.

at 10K for D-$Er_2Si_2O_7$: a = 4.6808(8) Å, b = 5.5566(2) Å, c = 10.7864(4) Å, α = 90°, β = 90°, γ = 96.064(2)°. These values found for the nuclear structure of D-$Er_2Si_2O_7$ were used in the refinement of the magnetic structure in Fig. 4.3a. The neutron diffraction data shown in Fig. B.2b is a subtraction of the 10 K data from the 2 K data. This shows the development of diffuse scattering expected in the vicinity of a second order phase transition. This is consistent with the magnetic ordering transition observed in D-$Er_2Si_2O_7$ at 1.9 K.

Table B.1: A table showing the positions (x, y, z) of the four Er^{3+} sublattices in the unit cell, the representation for each basis vector in terms of the (non-orthogonal) crystallographic *a*,*b*, *c* axes, the refined contributions (C_{10}, C_{11}, C_{12}) of each basis vector, and the resulting refined moment vectors for each Er^{3+} site.

Atom Info				ψ_{10}			ψ_{11}			ψ_{12}			Moment Direction
Atom	x	y	z	m_a	m_b	m_c	m_a	m_b	m_c	m_a	m_b	m_c	(**a**, **b**, **c** basis)
1	0.88829	0.09318	0.34934	1	0	0	0	1	0	0	0	1	(5.72(3), -2.34(6), -1.45(6))
2	0.11171	0.40682	0.84934	1	0	0	0	1	0	0	0	-1	(5.72(3), -2.34(6), 1.45(6))
3	0.11171	0.90682	0.65066	-1	0	0	0	-1	0	0	0	-1	(-5.72(3), 2.34(6), 1.45(6))
4	0.88829	0.59318	0.15066	-1	0	0	0	-1	0	0	0	1	(-5.72(3), 2.34(6), -1.45(6))
				C_{10} = 5.72(3)			C_{11} = -2.34(6)			C_{12} = -1.45(6)			

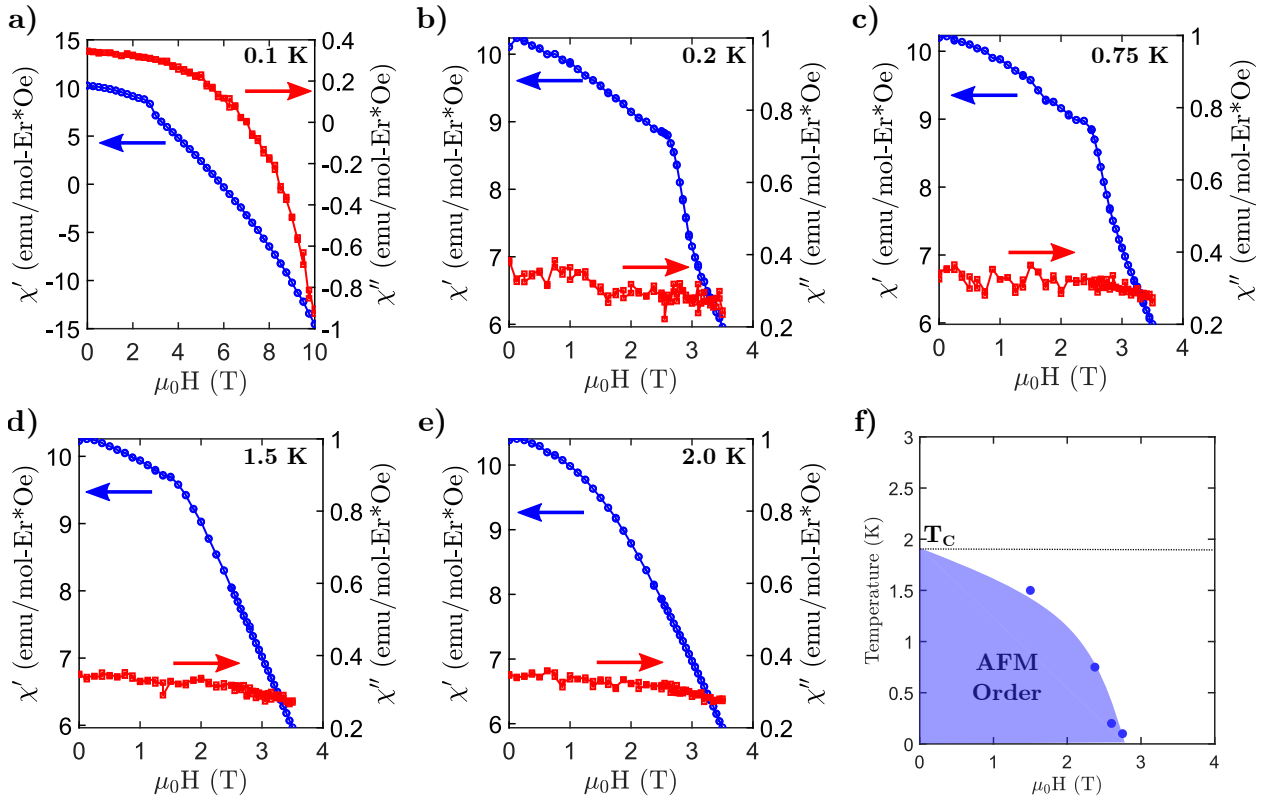

Figure B.3: a)-e) AC susceptibility data measured at several temperatures with $f = 1000$ Hz, H_{AC} = 2 mT up to a DC field of 10 T (panel a) or 3.5 T (panels b through e) with the field applied perpendicular to the Ising direction (i.e. applied along the x direction). The field-induced transitions are observable as a kink in the real component of the susceptibility (χ'). f) Phase diagram for D-$Er_2Si_2O_7$based on the AC susceptibility measurements shown in panels a-e. The transition points represent the points where the real part of the susceptibility (χ') abruptly changes due to the transition. The shaded region indicates AFM order.

The basis vector composition of the three basis vectors (ψ_{10}, ψ_{11}, ψ_{12}) in the Γ_4 irreducible representation are shown in Table B.1. These basis vectors are part of the Γ_4 irreducible representation which relates to the "m" point group symmetry and magnetic space group $P2_1$'/c.

B.3 AC Susceptibility and Magnetometry

B.3.1 Measurements along the transverse direction

Additional AC susceptibility measurements for a field applied perpendicular to the Ising direction are shown in and Fig. B.3. All data in this shown in this section is measured with $f = 1000$ Hz and H_{AC} = 2 mT. The data shown in Fig. B.3a demonstrates the susceptibility up to a DC field of 10 T. The transition observed in Fig. 4.2 at 2.65 T is also observed here. At high fields the signal

becomes diamagnetic, partly from the sample, partly from the mount and glue, and is likely due to the small moment along the transverse field direction which becomes saturated, leading to a small paramagnetic response. The data shown in Fig. B.3b-e consists of four constant-temperature field sweeps (increasing field) and demonstrates how the 2.65 T transverse field transition evolves with temperature. There is little change in the imaginary component of the susceptibility (χ'') as the temperature increases, but the real component of the susceptibility (χ') changes, with the transition moving down in field as the temperature is increased. Measurements with the field decreasing were not performed for these temperatures and therefore no statement regarding the hysteresis observed in Fig. 4.2 can be made.

B.3.2 Measurements along (4$\bar{9}$1)

As mentioned in the main text, a previous version of this manuscript showed AC susceptibility data that was presented as a field applied transverse to the Ising direction, but it was later discovered that the measurements were actually for a field applied 37° from the average Ising direction, approximately along the (4$\bar{9}$1) direction. We have included these data here (Fig. B.4). A comparison of data with $f = 100$ Hz at $T = 0.075$ K (originally shown in the main text) and 0.5 K is shown in Fig. B.4a. The data at 0.075 K shows a sharp peak in both the real (χ') and imaginary (χ'') components at 0.9 T, with a small shoulder near 0.65 T. This shoulder has no significant imaginary component. This changes at 0.5 K, where the shoulder increase significantly in magnitude in the real part of the susceptibility. We also see that the peak in the imaginary component shifts to coincide with the shoulder at 0.65 T. Similar changes are observed for a comparison of data with $f = 1000$ Hz and $T = 0.05$ K and 0.5 K, shown in Fig. B.4b. Overall, there is not a large difference between data measured at $f = 100$ Hz and $f = 1000$ Hz. One notable signature is that the transition at 0.65 T changes in magnitude with higher frequencies, indicating there may be some frequency dependence to this transition. The cause for these changes is not currently known, but may indicate a more complex field-induced phase diagram.

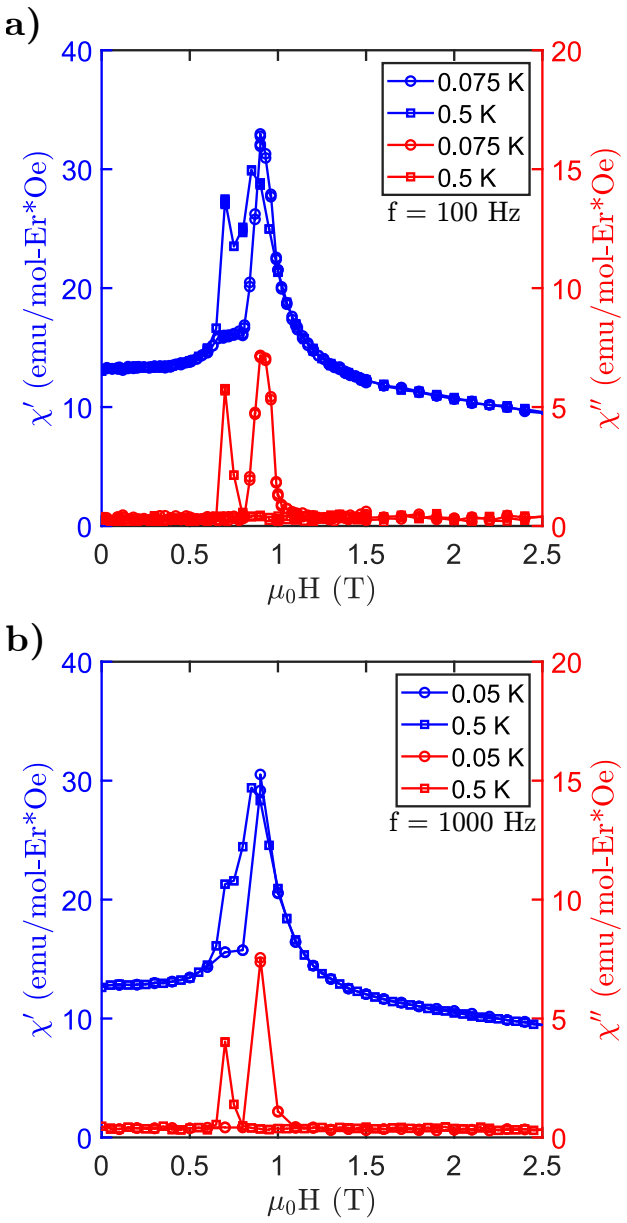

Figure B.4: a) AC susceptibility at 0.075 K and 0.5 K performed with a frequency of 100 Hz in an DC magnetic field applied 37° from the average Ising direction, approximately along the [4$\bar{9}$1] direction. and a 2 Oe AC magnetic field. b) AC susceptibility at 0.05 K and 0.5 K performed with a frequency of 1000 Hz in an DC magnetic field applied 37° from the average Ising direction, approximately along the [4$\bar{9}$1] direction. and a 2 mT AC magnetic field.

The DC magnetometry measurements that enabled us to identify the issue with the alignment are shown in Fig. B.5. These measurements were performed with a ^{3}He insert for the Quantum Design MPMS3. Measurements were performed for a field applied 37° from the average Ising direction, approximately along the [4$\bar{9}$1] direction. The fact that the measured moment is so large

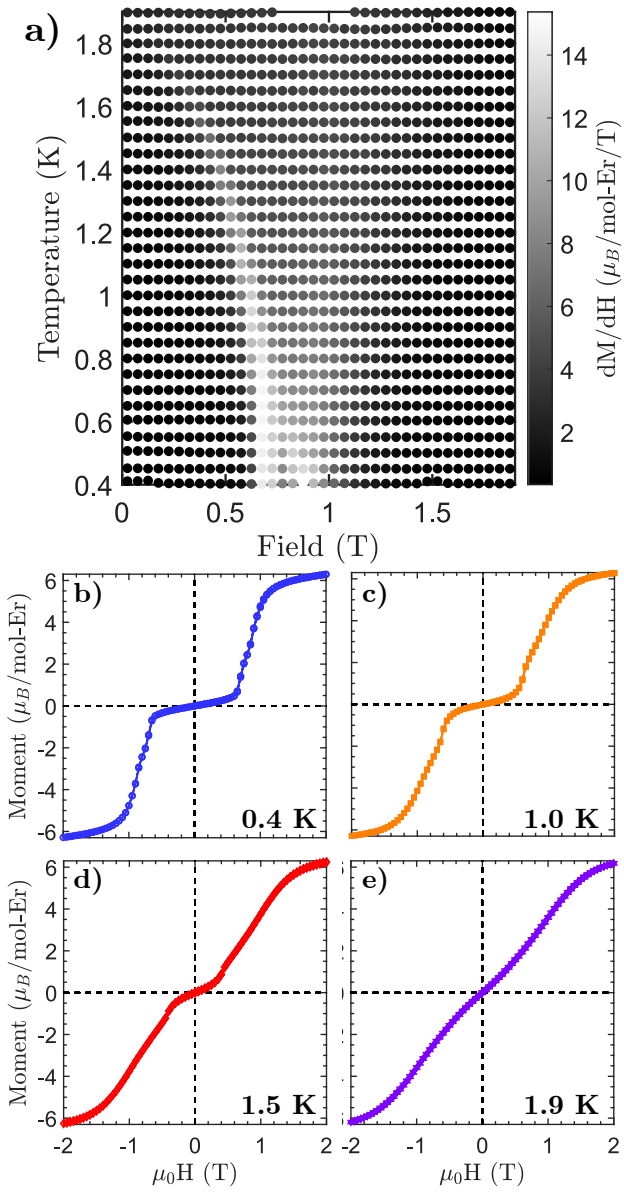

Figure B.5: a) A grayscale view of numerous constant-temperature field sweeps for the field-derivative of the DC magnetic susceptibility, showing a transition at 0.65 T that decreases in field as the temperature is increased. b-e) Characteristic field sweeps from the data shown in panel a).

along this field direction (6 μ_B) led to the discovery that the sample was misaligned, as the transverse field direction would be expected to have a maximum moment of 1.3 μ_B (based off Leask *et. al*'s g-tensor value of 2.6 for the transverse field direction).

B.4 MACS Data

Additional inelastic slices from the MACS data at 5 T (panel a) and 7 T (panel b) are shown in Fig. B.6. Both sets of data show Branch 2 increasing in energy relative to the 3 T data shown in Fig. 4.4e. Note, in Fig. B.6 the energy window was increased from 1 meV to 2 meV to allow all of Branch 2 to be visible.

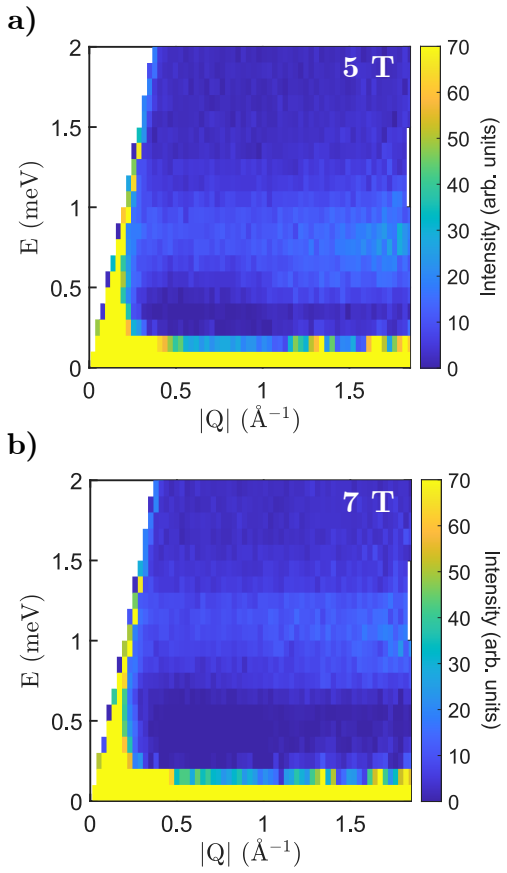

Figure B.6: a) Energy vs. |Q| slices (T_{avg} = 0.16 K) at μ_0H = 5 T. Branch 2 has increased relative to 3 T (Fig. 4.4e) due to Zeeman splitting. b) Energy vs. |Q| slices (T_{avg} = 0.16 K) at μ_0H = 7 T. Branch 2 has increased relative to 5 T, causing the energy window displayed to be increased from 1 meV to 2 meV.